UNIVERSITY OF CALIFORNIA
RIVERSIDE

Optimization Methods on Synthesis of Atomically Thin Layered Materials and Heterostructures

A Dissertation submitted in partial satisfaction
of the requirements for the degree of

Doctor of Philosophy

in

Materials Science and Engineering

by

Selcuk Temiz

September 2017

Dissertation Committee:

Dr. Cengiz S. Ozkan, Co-Chairperson
Dr. Mihrimah Ozkan, Co-Chairperson
Dr. Kambiz Vafai
Dr. Sandeep Kumar

The Dissertation of Selcuk Temiz is approved:

Committee Co-Chairperson

Committee Co-Chairperson

University of California, Riverside

ACKNOWLEDGEMENTS

I would like to express my sincere appreciation and gratitude to the institutions and people who have contributed to me financially, intellectually, and motivationally.

First, I would like to extend my deep gratefulness to my advisors Dr. Cengiz S. Ozkan and Mihrimah Ozkan. During my studies, they have provided to me strong encouragement, support, and perspective.

I would like to thank my committee members Dr. Kambiz Vafai and Dr. Sandeep Kumar for their valuable time and feedback.

I am grateful to have the opportunity to collaborate with Dr. Andre Mkhoyan and Ryan Wu from the University of Minnesota to perform a fundamental investigation on 2D materials systems through nano-scale electron microscopy characterization.

Thanks also goes to current and former members of the Ozkan's research group. Especially to Dr. Zafer Mutlu for his continuous collaboration, help, and scientific discussions during my studies. I would like to thank to Dr. Yu Chai for her kind help and training on the 2D materials dry transfer tool. I would like to thank to Sina Shahrezaei for his training and collaboration. I would also like to thank to my friends; Hasan Kurban, Mohammed Saadah, Ruben Salgado, Chenglong Jiang.

Finally, I thank to my family for their endless support and patience.

ABSTRACT OF THE DISSERTATION

Optimization Methods on Synthesis of Atomically Thin Layered Materials and Heterostructures

by

Selcuk Temiz

Doctor of Philosophy, Graduate Program in Materials Science and Engineering
University of California, Riverside, September 2017
Dr. Cengiz S. Ozkan, Co-Chairperson
Dr. Mihrimah Ozkan, Co-Chairperson

Two dimensional (2D) materials have emerged as a new class of materials that only a few atoms thick. Owing to their low dimensionality, 2D materials bear rather unusual properties that do not exist in traditional three dimensional (3D) materials. Graphene, a single layer of carbon atoms arrange in a 2D hexagonal lattice, has started the revolutionary progress in materials science and condensed matter physics, and motivated intense research in other 2D materials such as h-BN, and layered metal dichalcogenides.

Chemical vapor deposition (CVD) is the most studied bottom-up graphene production method for building the prototypes of next-generation electronic devices due to its scalability; however, there is still not an ultimate consensus of growth mechanisms on

control the size and morphology of synthesized-crystals. In order to have better understanding the growth mechanisms, the role of oxygen exposure in the graphene growth has been comprehensively studied. The oxygen gas is introduced into the CVD reactor before and during the growth, and its effects on the morphology, crystallinity, and nucleation density of graphene are systematically studied. It is found that introducing oxygen during growth significantly improves the graphene crystallinity while pre-dosing oxygen before growth reduces the graphene nucleation density.

The stacking of graphene and other layered materials in the lateral or vertical geometries can offer extended functionality by exploiting interfacial phenomena, quantum confinement and tunneling, which requires the interface between the layered materials be free of contaminates. The vertical heterostructures of CVD-grown graphene and h-BN single crystals are deeply investigated by analytical scanning transmission electron microscopy (STEM) and electron energy loss spectroscopy (EELS). It is shown that graphene contamination, undetectable using optical microscopy, is prevalent at the nanoscale, and the interfacial contamination between the layers reduces the interlayer coupling and ultimately undermines the graphene/h-BN heterostructures.

Raman spectroscopy is a versatile and non-destructive technique for the identification of structural properties and phonon features of atomically thin layered materials. Especially, the second order resonant Raman spectroscopy, which can be applied to the resonance conditions in energy of the incoming photon and interband transitions of an electron in a crystal lattice, reveals additional phonon modes to typical Raman active modes in spectra. Various 2D materials, including $SnSe_2$, WSe_2, SnS_2, and $MoTe_2$, and

their heterostructures are fabricated by dry transfer method as a top-down approach. The vibrational characteristics of these 2D materials systems are unambiguously established by using second order Resonant Raman spectroscopy.

Table of Contents

List of Figures

List of Tables

1. Chapter 1. Introduction

1.1 The Emergence of Atomically Thin Layered Materials

Atomically thin layered materials are the family of materials that includes the inorganic compounds of two-dimensional (2D) layers, which are linked together by van der Waals (vdW) forces while atoms are organized by covalent bonding in the plane, and that excludes atomically thin solid films which do not possess layered structures. Atomically thin layered materials consist of a few layers.

There have been reports about whether 2D crystal order is possible or not since late 1930s. As of leading scientists, Peierls [1] and Landau [2] had argued that low dimensional ordered materials are not possible to exist due to the lack of thermal stability, however Mermin has stated that some quantitative calculations indicates disputation on their results in terms of dimensionality of crystalline orders [3,4]. According to Landau, the thermal fluctuations are too big, and destroy the structure in 2D geometry when the fluctuation displacements are comparable to the size of the height of material [5]. Atomically thin materials, specifically 2D form of graphite, has been theoretically studied for years. Philip R. Wallace had calculated the interlayer spacing is quite larger than the distance between carbon (C) atoms in plane, and concluded that the interaction between the layers of graphite is insignificant, on his paper titled “The Band Theory of Graphite” in 1947 [6]. On his talk at American Physical Society (APS) annual meeting in 1959, famous physicist Richard Feynman has stated, “What could we do with layered structures with just the right layers? What would the properties of materials be if we could really arrange the atoms the way we

want them? They would be very interesting to investigate theoretically. I can't see exactly what would happen, but I can hardly doubt that when we have some control of the arrangement of things on a small scale we will get an enormously greater range of possible properties that substances can have, and of different things that we can do" [7].

The discovery of isolating layers of graphite to individual sheets of hexagonal arrangement of C atoms, called graphene, by Novoselov and Geim in 2004 [8], has started the revolutionary progress in materials science and condensed matter physics which is later called "Two Dimensional Materials" or "Atomically Thin Layered Materials". The realization and physical characterization of graphene has led scientists to a next chapter, which is to develop the complimentary group of atomically thin layered materials, so-called "Transition metal dichalocogenides (TMDs)" with the general formulation of MX_2 (M: transition metal, X: chalcogenide). Molybedenum disulfide (MoS_2), tungsten diselenide (WSe_2), and tin disulfide (SnS_2), tin diselenide ($SnSe_2$), molybdenum ditelluride ($MoTe_2$) are some intriguing examples of the TMDs family. Hexagonal-boron nitride (h-BN), silicine, germanene, phosphore and other similar materials are discovered soon after graphene, as members of atomically thin layered materials family.

Topological insulators (TIs) have emerged as a new class of quantum matter and member of atomically thin layered materials. Fu and Kane have predicted the TIs in their report [9] in 2007. Time reversal symmetry protected topological surface states are experimentally proved by David Hsieh and M. Zahid Hasan in 2009 [10]. Examples of the TIs include, but not limited to, bismuth telluride (Bi_2Te_3), bismuth selenide (Bi_2Se_3),

antimony telluride (Sb_2Te_3), stanene, mercury telluride (HgTe), and cadmium telluride (CdTe).

1.2 Properties of Atomically Thin-Layered Materials and Heterostructures

Atomically thin layered materials are single or few layers of sheets of materials in which atoms form strong chemical bonds in plane and there are weak van der Waals bonds between the layers of sheets. In these materials; electrons are free to move in two dimensions, but its movements are restricted in the third direction. This quantum mechanical confinement effect of electrons give rise to interesting properties such as; exceptional electronic and heat conductivity, dangling bond free and extremely smooth interfaces, energy independent step-like density of states, etc. These materials are expected to form the future electronics applications in transistors, sensors, solar cells, semiconductors, wearable electronics, battery electrodes, and spin devices.

Graphene has the unique electronic structure, at which the energy-momentum dispersion (Dirac-type energy dispersion) relationship is linear except the intersection of occupied and unoccupied energy states at gamma point of the Brillouin zone, leading to zero band gap structure. In graphene, four outer shell electrons make three σ bonds in plane and leaving an out of plane p_z orbital available for electronic conduction. These σ bonds formed by the sp_2 orbitals give graphene excellent mechanical and thermal properties. Graphene is hundreds of times stronger than the strongest steel, and it is quite flexible. The highly mobile p_z orbital electrons are located above and below the graphene sheet, and they give graphene excellent electronic properties such as Dirac type energy dispersion, high

mobility, etc. Dirac type energy dispersion in graphene implies that electrons have zero effective mass. Graphene has an excellent mobility (200,000 $cm^2V^{-1}s^{-1}$ at Room Temperature) [11], and that makes it the target material to work on for various device applications in electronics, spintronics, optoelectronics, etc.

Another important class of atomically thin layered materials is the metal dichalcogenides (MX_2: M: metal, X: chalcogen) that are three atom thick layers of semiconductors such as; MoS_2, $MoSe_2$, $MoTe_2$, WS_2, WSe_2, SnS_2, $SnSe_2$ etc. These materials have a direct electronic band gap when they are in monolayer form, but they have indirect electronic band- gap when they are few layer (2-8 layers), multilayer (9-25 layers), and bulk (>25 layers). They possess strong spin orbit coupling (SOC) in contrary to graphene. Strong spin orbit coupling gives rise to spin splitting, and this drives to control on electrons spin through tuning excitation signal. Their electronic band gap varies from 0.7 eV to 3.0 eV, and that gives the opportunity to use them in various applications. The electronic band gap of MX_2 materials can be tuned by mechanical strain for usually transistor applications.

Topological insulators (TIs) are another layered material family that consists of one atomic thick layer in two-dimensional TIs (e.g. stanene) and 5 atomic thick layers (quintuple layers) in three-dimensional Tis (e.g. $B_{i2}Se_3$), where layers are bonded to each other via van der Waals interactions. These materials are insulator in bulk, but they have conducting metallic surface or edge states on their boundaries. Bi_2Se_3, Bi_2Te_3, Sb_2Te_3 are among the three-dimensional topological insulators, mercury telluride (HgTe), cadmium telluride (CdTe), stanene, silicine are among the two dimensional topological insulators.

Topological insulators consist of heavy atoms; hence spin orbit coupling is so strong in these materials. Strong spin orbit coupling enables them to be used in spintronics. Two-dimensional topological insulators, such as stanene, present strong quantum spin hall behavior and they are called quantum spin hall insulators (QSHI). The electronic conduction is confined through the boundaries, and it is spin-polarized. QSHI type materials are the perfect candidates for their use of spintronics by their room temperature metallic states at boundaries. Topological insulators are also used in heterostructures of atomically thin materials to mostly exploit their induced spin orbit coupling at interface with other layered materials such as graphene. In graphene-bismuth telluride heterojunction, the epitaxial graphene turns into a quantum spin hall phase due to proximity to topological insulators by developing a spin orbit gap around 20 meV [12], which is three orders of magnitude larger than the one of on pristine graphene.

1.3 Synthesis of Atomically Thin Layered Materials and Heterostructures

Atomically thin layered materials can be synthesized by various techniques from bottom-up to top-down approaches. Micromechanical exfoliation (as of top-down approach) is one of the mostly used synthesis methods for production of these materials. Micromechanical exfoliation is operated by picking up layered crystal form the source material by mechanically-breaking the bonds between layers and transferring to arbitrary-substrate through an adherent tape or polymer. The structural formation of atomically thin layered materials provides the perfect compatibility with this synthesis method thanks to weak interlayer van der Waals type bonding. Micromechanical exfoliation is the technique

that is relatively easy to apply, reliable, and results high crystalline quality [13]. The downsides of micromechanical exfoliation are lack of scalability, repeatability, and contamination caused by adhesives. Graphene has been discovered by isolating layers of graphite to single layer form with scotch tape. This method is mostly preferred for academic research purposes due to its high quality yield.

The source materials used for micromechanical exfoliation are usually grown by so-called Bridgman method [14]. In the Bridgman method, a polycrystalline precursor, usually in the powder form, is heated up to melting point, and then it is gradually cooled down to the point where it starts forming seed. The Bridgman method yield high crystalline quality product on their bulk, but the process takes long time from 48 to 72 hours.

Chemical exfoliation is another technique used to separate layers of atomically thin layered materials [15]. The source material is immersed in a liquid solution and vibration is applied through sonication, and that results the separation of layers. The important point with chemical exfoliation is to manage to determine the right solution in terms of the interaction energy. This method yields defective product, hence it is favorable for energy storage applications, which require defective and porous surfaces.

Chemical Vapor Deposition (CVD) is a bottom-up approach to synthesize atomically thin layered materials [16]. CVD process occurs when the introduced-precursor gases decomposed and condensed onto surface of hot substrate because of temperature gradient in the reaction chamber. Precursor and noble gases in CVD chamber is evacuated through an exhaust system to avoid contamination or side effects on the product. CVD

method provides relatively high quality, uniform, scalable atomically thin layer materials as a final product.

1.4 Characterization of Atomically Thin Layered Materials and Heterostructures

Understanding and utilizing the scattering phenomena require number of scientific tools to research highly-ordered crystalline structures by the interaction of photon, ion and electron with matter. Raman spectroscopy is a micro-scale analytical tool that provides information about molecular vibrations and crystal structures [17, 18]. Raman spectroscopy employs the analysis of inelastic scattering of electromagnetic radiation with the matter of interest.

The scattering events can be observed when a pocket of energy in the form of light interacts with the non-uniform media through molecular vibrations, resulting the change in the direction and energy of the incoming light. Scattering of light can be categorized as elastic and inelastic scattering based on the conservation of energy. Raman spectroscopy utilizes the inelastic (Raman) scattering of incoming light, while detectors filter out the elastic part (Rayleigh scattering). Raman scattering can be visualized with the Stokes and anti-Stokes lines depending on the incoming photon gaining or losing energy to the molecules interact with (**Figure 1.1**). Stokes scattering represent the conditions that the scattered light has lower energy than incoming light by transferring some of its energy to the molecules during interaction. When the scattered light is promoted to the higher energy levels than incoming light by gaining energy from the molecules interact with, it is called anti-Stokes scattering.

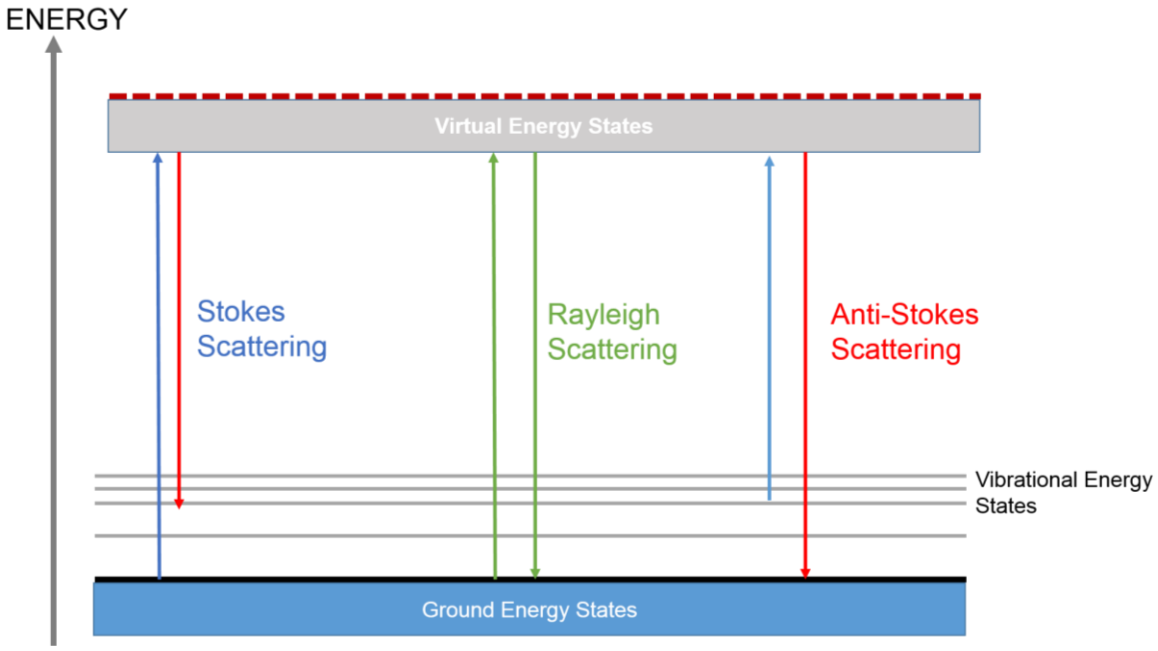

Figure 1.1. The schematic illustration of Stokes, anti-Stokes, and Rayleigh scattering.

The Raman shift in wavenumbers ($\mathcal{V}^*$) is calculated by the **Eq. 1.1**, and it depends on the vibrational, rotational or electronic transitions inside the molecule.

$$\mathcal{V}^* = \left(\frac{1}{\lambda_{incident}} - \frac{1}{\lambda_{scattered}}\right) (\text{cm}^{-1}) \qquad \textbf{(Equation. 1.1)}$$

Where, $\lambda_{incident}$ is the wavelength of the incoming light and is a known parameter.

A molecule can be excited to higher vibrational energy states from the ground state by interacting a shining light on it. These excited energy levels are quantized and designated as normal modes of vibration of molecules. These modes can be visualized as the vibrations of bonds between two or three atoms or bonds direct to out of plane. The Raman spectroscopy relies on the polarizability of molecules since incoming light interacts with molecular bonds. The spectral analysis of the scattered light provides useful

information about the composition and structure of the molecules. We employ the Raman spectroscopy characterization to identify the thickness, crystal quality, and composition of graphene, h-BN, and graphene/h-BN structures, TMDs crystals and its heterostructures.

The systematic analysis of the interactions of electron with matter provides a broad range of information about structural and chemical properties of the material of interest (**Figure 1.2**). Electron's interaction with a specimen can be categorized as elastic and inelastic forms. In the elastic interactions, there is no energy exchange between electron and specimen as the beam of electrons pass through or scattered by specimen with the same energy as incident beam energy. Inelastic interaction is the more beneficial part of the electron-matter interactions since it provides a lot of physical and chemical characteristic of a specimen. Energy exchange occurs during the course of inelastic interactions that can be read as the scattered primary electrons with changing the momentum and direction, or the excited secondary electrons, photons, X-rays, Auger electrons. The outcomes of inelastic interactions of electrons with matter can be utilized to determine various characteristics of samples by evaluating these change in energy spectrum.

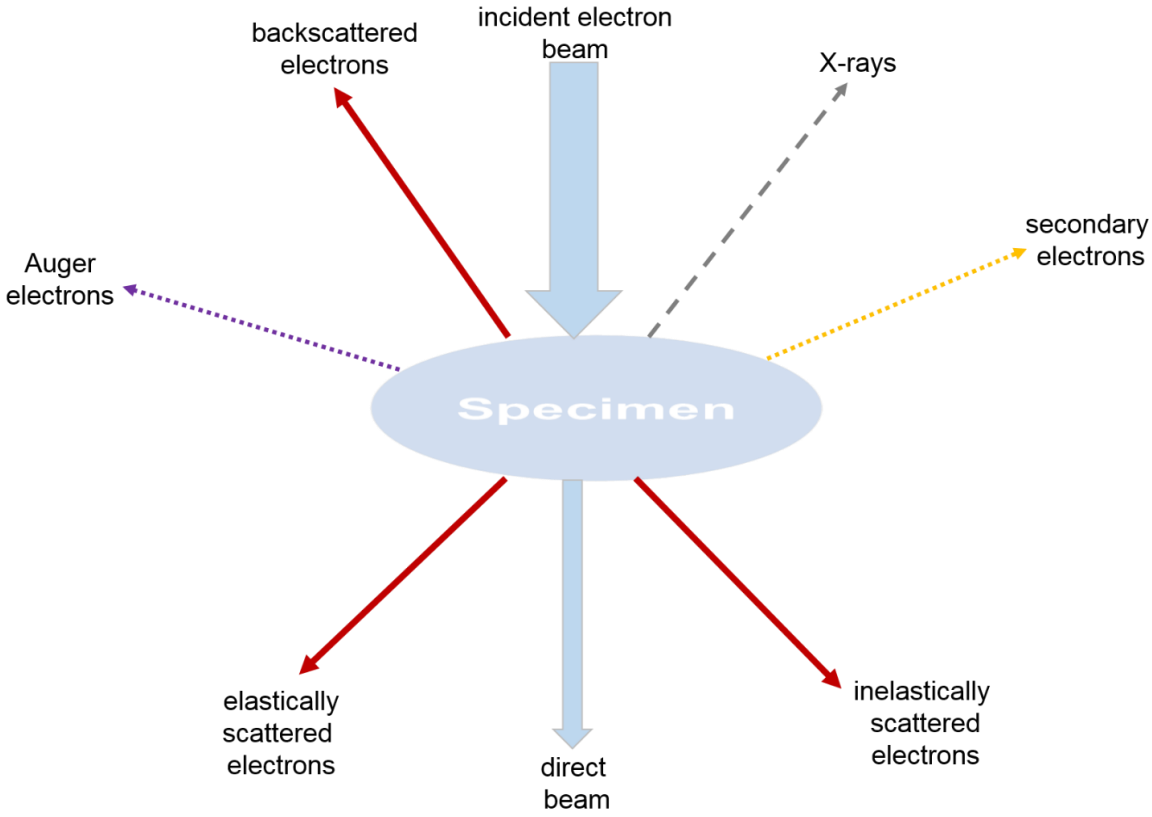

Figure 1.2. The schematic illustration of electron-matter interaction.

1.5. Applications of Atomically Thin Layered Materials and Heterostructures

Atomically thin layered materials promise the leading advancement in future technology thanks to its extraordinary properties. These technological applications include transistor devices, sensors, spintronics, photovoltaic, flexible electronics, energy storage, composites, and information processing [19]. The most prominent applications of these materials is the transistor devices due to their semiconductor nature and unique electronic properties stem from quantum confinement of electrons.

It has been more than six decades since the first silicon transistor introduced as a revolutionary technology to human lives, and it is improved over these years parallel to the Moore's Law. New technological applications, such as nanotechnology, develops gadgets to have more transistors in smaller sizes, hence it results to shrink the channel length of devices. The performance problem, which is designated as the deteriorated mobility, appears when the reduced channel length becomes comparable to the thickness of the materials used in nano-scale devices. The response or adaptation of the scientific community to this size related problem is to redesign transistors made of atomically thin layered materials to overcome these mobility-based obstacles stem from the channel length-thickness ratio to as-defined problem. Atomically thin layered materials have emerged as the need for future generation electronics since the conventional silicon chip based applications came to its limit. Atomically thin layered materials are not only offer solution to mobility problem, but also, they are the unique platform to serve as almost scattering-free ballistic conduction in room temperatures and ideal materials for wearable electronics devices. These materials promise the ideal materials base for nano-scale device applications such as; transistors, sensors, solar cells, optoelectronic devices, etc. The heterostructures of atomically thin layered materials are the excellent candidates for new generation technology with their distinct properties which is not possible with homogenous or homo-junction structures. Heterostructures present a platform that the interface can be tuned by mechanical strain, thickness, and electric field. These heterostructures can optimize the charge transfer by applied electric field and materials thickness at interface for device applications such as, the tunnel field effect transistors (TFETs).

1.5.1. Heterostructures of Atomically Thin Layered Materials

Heterojunctions of materials with different characteristic properties present a useful foundation to understand, discover, and optimize complex condensed matter systems that are shaped by new physical states. Tunnel field effect transistors (TFETs), one of the most promising applications, are quite efficiently enabled by heterostructures of atomically thin layered materials. Near broken or broken band gap heterostructures of these materials allow the phenomena so-called band-to-band tunneling (BTBT) of electrons to operate the transistors based on electrical band alignment by applied electric field instead of thermionic excitation of electrons.

Future generation electronics, including low power electronics by tunneling field effect transistors (TFETs), field effect transistors (FETs), spintronics, p-n junctions, and photodetectors, employs heterostructures as the base-platform for their operations [20]. Heterostructures of materials with different physical properties have served as a basis for finding new physical states and understanding complex phenomena in condensed matter systems. The electronic, optical, and magnetic properties in heterostructures differ from those individual crystals itself. Junctions between heterogeneous materials present interesting properties that are not likely to be observed between homogenous junctions. The diffusion of the order parameters by proximity induces a weak order in the nano-ordered materials, generating quantum interference effects. Heterojunctions of materials with different topological orders can thus provide an interesting platform to explore emerging quantum phenomena of Dirac fermions at the interface. As an interesting

example of the use of heterostructures in spintronics, “the Graphene-Bismuth Telluride junction” is used as the spin device, in which the built-in spin orbit coupling in graphene is regulated by the Bismuth Telluride’s proximity effect at the junction, hence graphene is being spin polarized at the junction [21, 22]. This device design enables one to use spin device with no need of spin valve to turn on/off. Another use of heterostructures in electronics is the platform for tunnel field effect transistors by using specific atomically thin-layered materials with near broken band gap alignment such as molybdenum disulfide-tungsten disulfide [23]. Graphene-hexagonal boron nitride is another widely studied interesting class of heterostructures because of structural similarities, and electronically different properties, hence the synergy between these two materials. In graphene channel devices, the h-BN is mostly used as a substrate due its stable and uniformly smooth surface results to enhance the performance of devices [24].

1.5.2. Band Bending at Semiconductor Heterojunctions

The new generation electronics demands to interpret and utilize how the band structure lineup in energy of two or more different semiconductors at interface in terms of materials engineering because of its fundamental and technological implications. The energy band diagram is a representation of the carrier energy levels determined in quantum mechanical calculations by tracing the probability of the allowed wave functions in certain states.

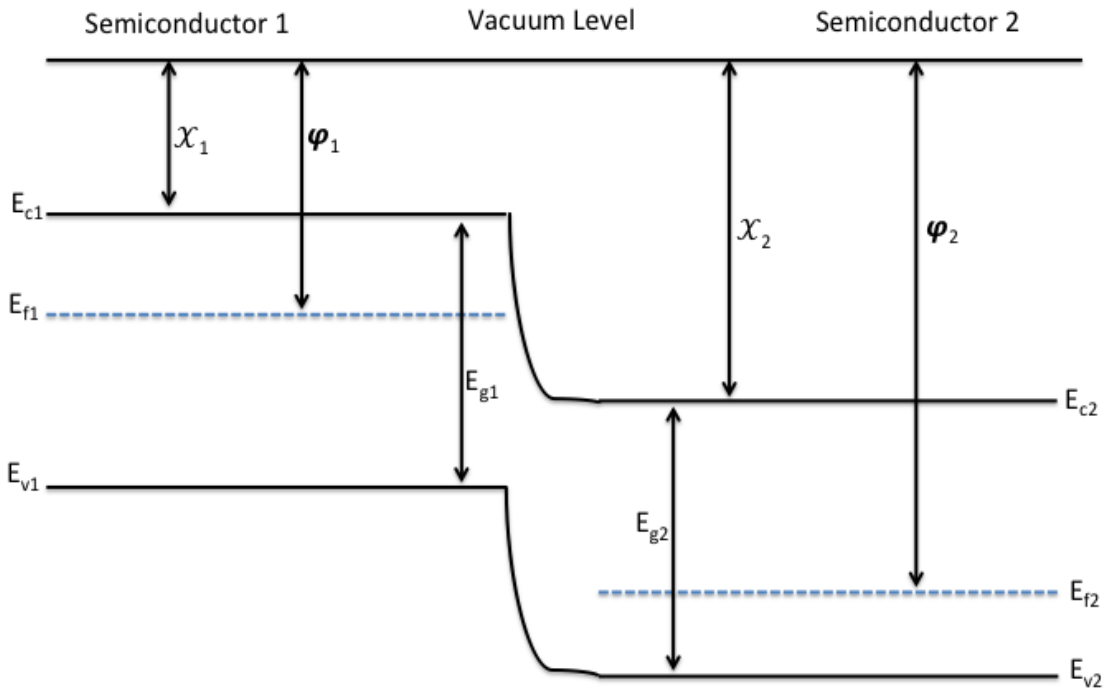

Figure 1.3. The illustration of energy band diagram of semiconductor heterostructures.

The **Figure 1.3** shows an energy band diagram of a p-n type heterostructures consist of two different type of semiconductors; semiconductor-1 is being n-type, energy band gap E_{g1}, and semiconductor-2 is being p-type, energy band gap E_{g2}. Vacuum level is the energy of a free electron that is at rest with respect to the semiconductors. At absolute zero temperature, E_v is the valence band that is the highest fully occupied band, E_c is the conduction band that is the lowest empty band. The positions of E_c and E_v are determined by the chemical bonding of the atoms. Where χ is the electron affinity that defines the change in energy of a neutral atom (in the gaseous phase) when an electron is added to the atom to form a negative ion. E_f is the Fermi level that is the highest occupied electron energy level at absolute zero temperature.

The band bending is the way to draw a picture about how the charge exchange at interface reorder energy offset of a semiconductor's band structure near a junction. When two different semiconductors meet at interface, at first, the edges of the valence and conduction bands line up while the Fermi level reveal discontinuities. Then, the carriers diffuse across the junction that leads to accumulation of space charges until the built-in potential balances carrier diffusion and Fermi levels of both materials get aligned to each other in equilibrium. According to the Fermi-Dirac statistics, there must be only one Fermi level at interface; this is why the band edges bend spatially as in illustrated in the energy band diagram of heterostructures.

1.5.3. Band Alignment in Semiconductor Heterojunctions

The characteristics of heterostructures depend on the energy band alignment of heterogeneous semiconductor combinations [25]. The energy band line has step-like discontinuities in semiconductor heterojunctions. It is crucial to predict the band alignment of energy bands in heterostructure in terms of device applications. There are several methods to predict the band alignment of heterostructures of semiconductors.

Anderson's rule or affinity rule is a method to build energy band diagram of the heterojunction between two semiconductors. It basically aligns the vacuum levels of two semiconductors on each side as the same energy. Anderson's rule does not practically predict the band alignment of actual heterostructures on lack of consideration of strain effects, defects, and lattice mismatch by fundamentally avoiding the influence of chemical bonding.

Another model is a common anion rule that predicts the band alignment of the heterostructures of semiconductors by generalizing the energy band behavior of valence band of semiconductors because valence band characteristics of semiconductors are linked to anionic states, and same anionic states should result quite small valence band offsets. Even though, the common anion model is useful to generalize the chemical behavior, it is not useful for use of wide range of solids with structural variation.

Gap state model is a method to predict band alignment similar to the case when the schottky type contact formed. The metal electron states penetrate into the semiconductor's band gap, and this penetration length can be calculated. Gap state model take consideration of the dipole layer, stem from electron tunneling from conduction band of a material to the energy gap of the other same as Schottky type contact) at the interface between two semiconductors. This model is successful with the heterostructures on which the semiconductor components with negligible lattice mismatch.

There are three types of band alignments of heterostructures of semiconductors at the junctions. To understand the band alignments at the junctions of heterostructures are very important to design and build nanoscale devices in various fields.

1.5.3.1 Type I (Straddling Gap) Band Alignment

The type I band alignment happens when the band gap of one material completely overlap the band gap of the other material, and it is called straddling gap. **Figure 1.4** shows type I band alignment when semiconductor materials form heterostructures.

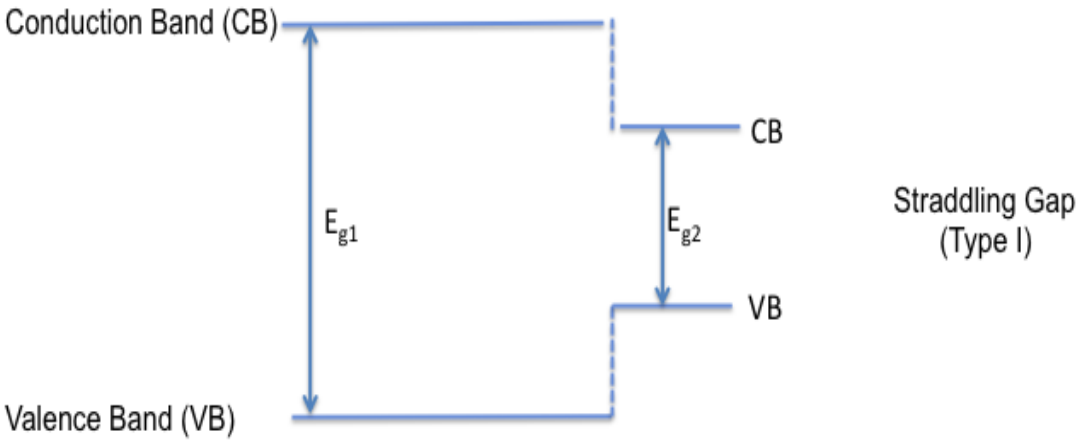

Figure 1.4. The illustration of the type I band alignment of semiconductor heterostructures.

1.5.3.2 Type II (Staggered Gap) Band Alignment

Type II band gap alignments occur when the band gaps of the two materials overlap but one does not completely enclose the other, and it is called staggered gap. **Figure 1.5** shows type II band alignment when two semiconductor materials form heterostructures.

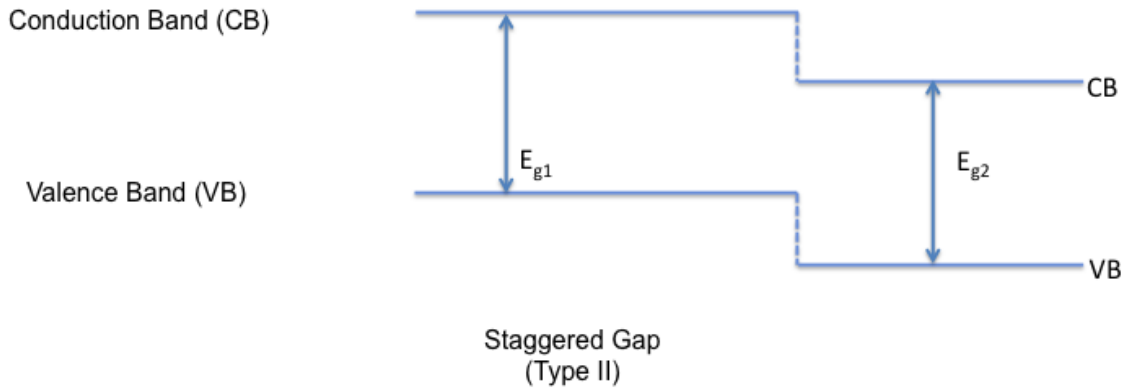

Figure 1.5. The illustration of the type II band alignment.

1.5.3.3. Type II (Broken Bandgap) Band Alignment

Type III bandgap alignments occur when the bandgap of two materials do not overlap at all in energy, and it is called the broken bandgap. **Figure 1.6** shows type III band alignment when two semiconductor materials form heterostructures.

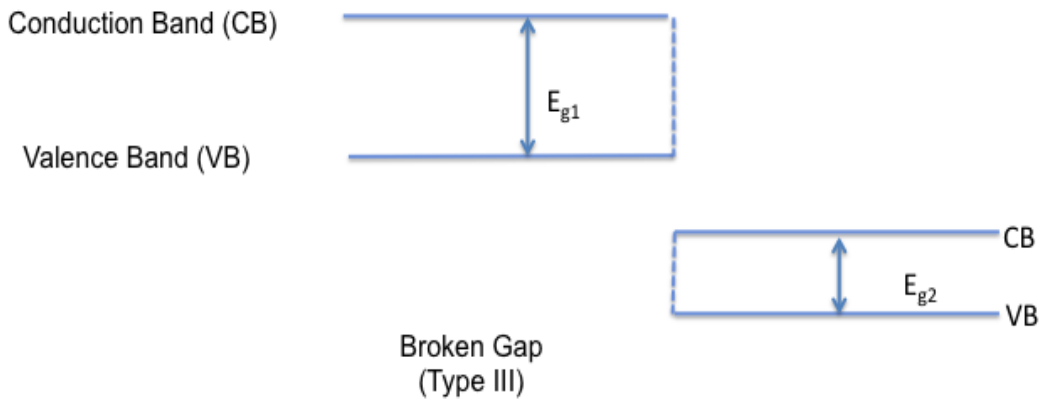

Figure 1.6. The illustration of the type III band alignment.

1.5.4. Tunneling Field Effect Transistors (TFETs)

Field Effect transistor is a device composes of semiconductor p-n junction, and its channel structure and behavior is controlled by applied electric field. The conductivity of FETs depends on the diameter of the channel. Tunneling field effect transistor (TFET) is one of the futuristic device design placed in low power electronics as an advancement of FET transistors[6]. The structure of TFET is similar to MOSFET, but it differs from the traditional transistors with its switching mechanism that is to regulate the quantum mechanical tunneling instead of regulating the thermionic diffusion of carriers. Vertically stacked heterostructures of atomically thin-layered materials present promising candidacy

for TFET device applications with their dangling bond free smooth interfaces and energy independent step-like density of states.

Power consumption is the one of the biggest challenges to accomplish in new generation electronics. In today's electronics, scaling down (nano-scale) on widely used transistors allows one to put more transistors into the circuit, hence more nano-devices drain more power that cause shorter battery life and heating on the gadgets we use our daily life. In the existing transistor designs, such as MOSFET, the low power switching is not possible because the thermal emission of carriers has its limitation (substhreshold switch (SS) is limited to 60mV/dec.) according to the Boltzmann statistics. Subthreshold is the gate voltage needed to change the transistor current by one order of magnitude. In the light of this power consumption issue, the revolutionary advance, based on quantum mechanical effects, is the so-called "the Steep Slope Devices" that includes "Impact Ionization Field Effect Transistors", "Electro-Mechanical Field Effect Transistors", "Ferroelectric Field Effect Transistors", "Feedback Field Effect Transistors", and "Tunnel Field Effect Transistors".

Tunneling field effect transistors exploits quantum mechanical tunneling phenomena between energy bands, so-called band-to-band tunneling (BTBT). Tunneling is the probability of the wave function of transmission that calculated from the Schrödinger's equation by the law of quantum mechanics. Tunneling is always possible, but the probability function varies with the barrier height, internal energy, perturbation, etc. Band to band tunneling implies the tunneling of carriers form the valence band of one material to the conduction band of the other material or vice versa by the operation of gate

voltage. Band to band tunneling mechanism needs low voltage regulation to be functioned, and it is fast because of the quantum nature of tunneling. Tunnel field effect transistors are requires low power to fast operations thanks to the band-to-band interband tunneling. There are possible fundamental enhancements of the performance of tunnel field effect transistors such as channel structure engineering, doping engineering, and materials selection engineering. We work on the materials engineering by using the best-suited materials in nanoscale to obtain best results.

Schrodinger's Equation and tunneling probability (Eq. 1.2):

$$\frac{\partial^2\psi(z)}{\partial z^2} = \frac{2m}{\hbar^2}\{E - U(z)\}\psi(z) \qquad \textbf{(Equation. 1.2)}$$

And solution of the Schrodinger's Equation (Eq. 1.3) gives us:

$$\psi(z) = \psi(0)e^{\pm ikz} \qquad \textbf{(Equation. 1.3)}$$

Where, ψ is the wave function of the carrier, z is the spatial distribution, W is the barrier width, E is the kinetic energy of the carrier, U is the potential energy of the carrier which is related to band structure.

The starting point to the material engineering for tunnel field effect transistors is materials selection that is to study, simulate, prepare, and optimize the suitable materials for the purpose. According to tunneling probability calculations, the materials effective masses, and their energy band structures play a crucial role on quantum tunneling, so does the device performance. To point of view of quantum mechanics, small band gap

semiconductors are more preferable for tunneling based application. Another issue is the keep the barrier as low as possible to ease the tunneling. With conventional materials, the Fermi level pinning is the issue that puts extra energy barrier on the surface, but fortunately, in atomically thin materials the Fermi level pinning is not occurs thank to dangling bond free smooth surface. When the heterostructure is built with atomically thin materials, there it forms a van der Waals gap between the materials, and it prevents the Fermi level pinning. Atomically thin materials also easy to build because of their layered nature. As a result, to choose proper the proper materials is the key issue for technological advance.

Figure 1.7 illustrates the structure of a field effect transistor built on a lateral heterostructure. Lateral heterostructures can be built in different ways, among them CVD based synthesis is preferred by most of the engineers because of its large scale, uniform product.

Figure 1.8. Illustrates the structure of field effect transistor built on vertical heterostructure. Vertical heterostructures are preferably synthesized by micromechanical exfoliation and dry transfer method, and CVD is not desired for vertical heterostructures because atoms from different origin diffuse into each other and creates alloys instead of protected van der Waals gap between the layers.

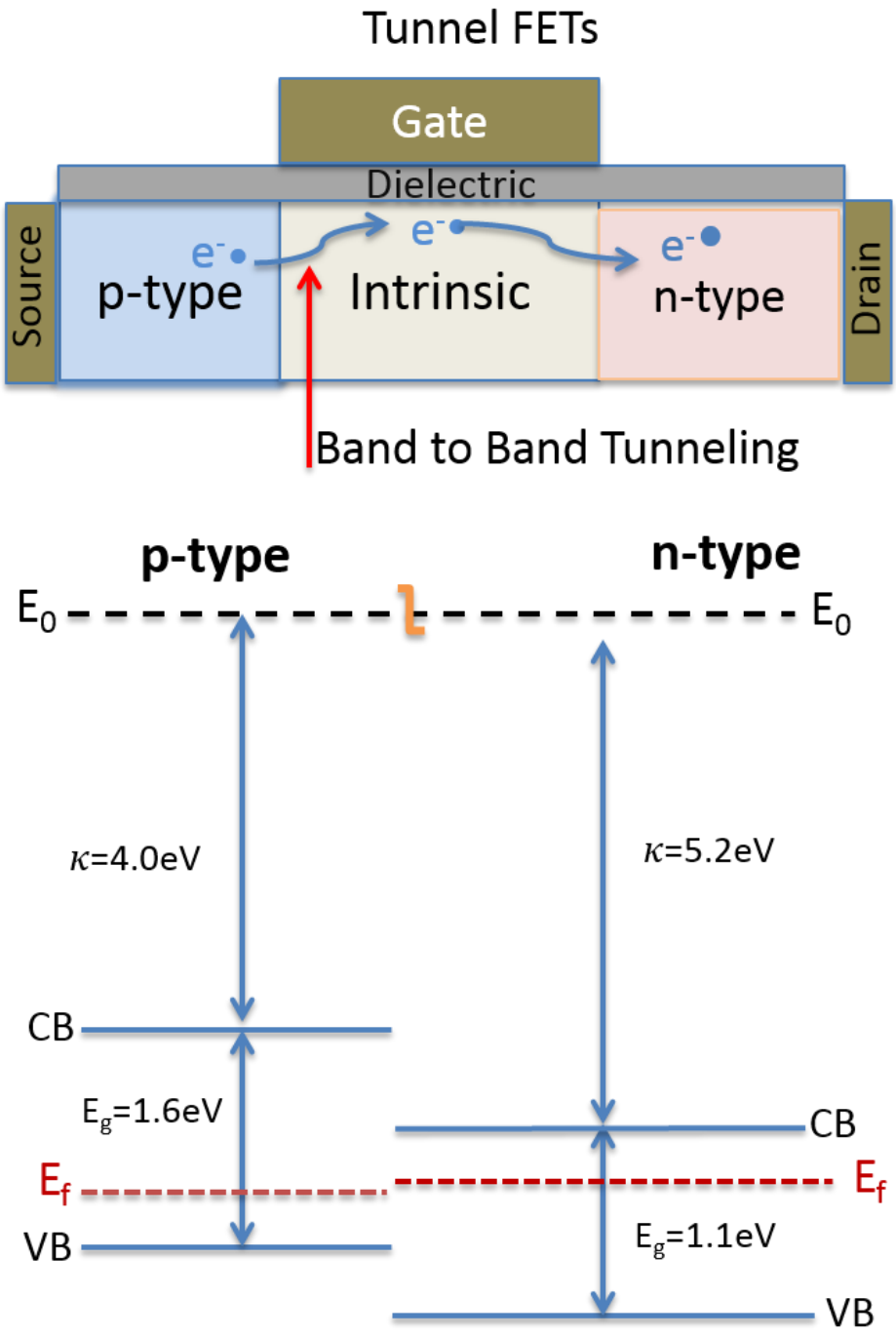

Figure 1.7. The schematic illustration of tunnel field effect transistor form on a lateral heterostructures.

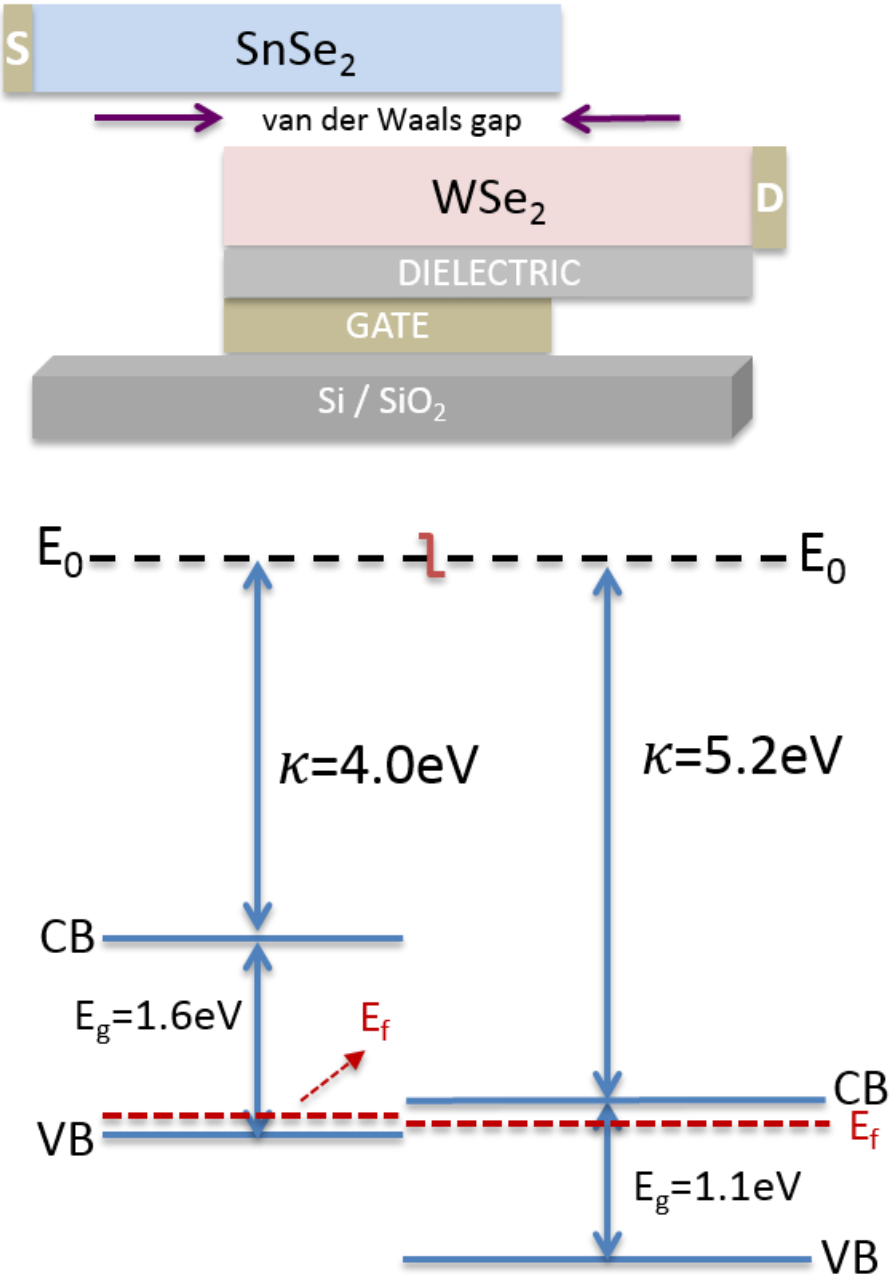

Figure 1.8. The schematic illustration of tunnel field effect transistor form on a vertical heterostructures.

1.6. Challenges of the Production and Integration of Atomically Thin Layered Materials to the Nanotechnology Applications

Atomically thin layered materials are used to be synthesized either isolating individual layers from their bulk form as a top-down approach namely exfoliation, or building the structure from the scratch as a bottom up approach namely growth. For each synthesis technique; there are wide range of parameters to consider such as operational difficulties, selection of sources, and the enhancement of quality of the product. Therefore, it is crucially important that how one synthesizes these materials and utilizes its properties to obtain the maximum efficiency in terms of materials design, device performance, compatibility with various applications, etc.

Even though, the better device performance has been obtained by micromechanically exfoliated samples for research point of view, chemical vapor deposition (CVD) is still more preferred materials synthesis method on graphene production for applications point of view including electronics, spintronics, and photonics thanks to its wafer scale, uniform, and controllable features [25]. However, there are certain complications for CVD growth of graphene. One major issue is that the deposition is limited to occur on a catalyst metallic substrate surface such as copper and nickel, and these substrates cannot be employed as a base platform for device applications, hence; the graphene needs to be transferred onto mostly SiO_2/Si substrates after CVD process. There are different types of techniques for transferring graphene from copper substrate to SiO_2 or other final substrates [26]. It is important that to employ the best technique to preserve graphene's unique properties, which are high mobility, mechanical strength, etc., after

transfer process. CVD grown graphene needs to deal with some other issues such as choice of substrate, orientation of substrate, contamination from the reaction chamber, etc. The controlling the order and quantity of exposure of gaseous species in CVD system plays a crucial role on graphene production.

Even though, micromechanical exfoliation is limited by materials library and lack of control on product, it is a mostly preferred synthesis method with its simple, reliable, high crystalline quality yield features to study elementary properties of materials for research purposes. The key parameters that have an effect on the quality of the product with micromechanical exfoliation are to handle the transfer process properly, the choice of adhesive tools, cleanness of the substrate, quality of the bulk materials, aftermath treatment, etc. Building heterostructures of atomically thin layered materials with the dry transfer tool is basically the post micromechanical exfoliation process. Dry transfer method is to attach two different layered materials mostly in vertical orientation to form a heterostructure. The quality of heterostructures by dry transfer method depends on the compatibility of equipment used in process, operational skills, aftermath treatment, etc. The structural identification via characterization tool is an important step for micromechanical exfoliation. The non-destructive, easy to apply, and versatile micro-characterization tool, namely Raman spectroscopy, is employed to identify the properties of atomically thin layered crystals. However, there is still not a standard and peak assignment for identifying structural properties and analyzing phonon behaviors of some transition metal dichalcogenides such as, WSe_2 and $MoTe_2$.

1.7. Outline

The sequent chapters of this dissertation is organized as follows. In chapter 2, the effect of intermittent oxygen exposure on chemical vapor depostion of graphene is systematically investigated. In chapter 3, the interface of graphene / h-BN is investigated in terms of interlayer coupling between the constituents of the van der Waals heterostructures. In chapter 4, the second order resonant Raman spectroscopy characterization of the metal dichalcogenides and heterostructures are studied. Conclusively in chapter 5, we are going to summarize the key findings of this thesis.

1.8. References for chapter 1

[1] R.E. Peierls: *Quelques proprietes typiques des corpses solides*. Ann. IH Poincare **5** (1935) 177-222.

[2] L.D. Landau: *Zur Theorie der phasenumwandlungen II. Phys. Z. Sowjetunion* **11**, no. 545 (1937) 26-35.

[3] N.D. Mermin: *Crystalline order in two dimensions*. Physical Review **176**, no. 1 (1968) 250.

[4] B.J. Alder and T. E. Wainwright*: Phase transition in elastic disks*. Physical Review **127**, no. 2 (1962) 359.

[5] A.K. Geim, and K.S. Novoselov: *The rise of graphene*. Nature materials **6**, no. 3 (2007) 183-191.

[6] P.R. Wallace: *The band theory of graphite*. Physical Review **71**, no. 9 (1947) 622.

[7] R.P. Feynman: *There's plenty of room at the bottom*. Engineering and science **23**, no. 5 (1960) 22-36.

[8] K.S. Novoselov, A.K. Geim, S.V. Morozov, D. Jiang, Y. Zhang, S.V. Dubonos, I.V. Grigorieva, and A.A. Firsov: *Electric field effect in atomically thin carbon films*. Science **306**, no. 5696 (2004): 666-669.

[9] L. Fu, and C.L. Kane: *Topological insulators with inversion symmetry*. Physical Review B **76**, no. 4 (2007) 045302.

[10] D. Hsieh, Y. Xia, D. Qian, L. Wray, F. Meier, J.H. Dil, J. Osterwalder, L. Patthey, A.V. Federov, H. Lin, A. Bansil, D. Grauer, Y.S. Hor, R.J. Cava, and M.Z. Hasan: *Observation of time-reversal-protected single-Dirac-cone topological-insulator states in Bi2Te3 and Sb2Te3*. Physical review letters **103**, no. 14 (2009) 146401.

[11] K.I. Bolotin, Kirill, K. J. Sikes, Z. Jiang, M. Klima, G. Fudenberg, J. Hone, P. Kim, and H.L. Stormer: *Ultrahigh electron mobility in suspended graphene. Solid State Communications* **146**, no. 9 (2008) 351-355.

[12] K.-h. Jin, and S.-H. Jhi: *Proximity-induced giant spin-orbit interaction in epitaxial graphene on a topological insulator*. Physical Review B **87**, no. 7 (2013) 075442.

[13] Y. Huang, E. Sutter, N.N. Shi, J. Zheng, T. Yang, D. Englund, H.-J. Gao, and P. Sutter: *Reliable exfoliation of large-area high-quality flakes of graphene and other two-dimensional materials*. ACS nano **9**, no. 11 (2015) 10612-10620.

[14] P.W. Bridgman, Percy Williams: *The resistance of 72 elements, alloys and compounds to 100,000 Kg/Cm²*. In Proceedings of the American Academy of Arts and Sciences **81**, no. 4 (1952), pp. 165-251.

[15] J.N. Coleman, M. Lotya, A. O'Neill, S.D. Bergin, P.J. King, U. Khan, K. Young, A. Gaucher, S. De, R.J. Smith, I.V. Shvets, S.K. Arora, G. Stanton, H.-Y. Kim, G.T. Kim, G.S. Duesberg, T. Hallam, J.J. Boland, J.J. Wang, J.F. Donegan, J.C. Grunlan, G. Moriarty, A. Shmeliov, R.J. Nicholls, J.M. Perkins, E.M. Grieveson, K. Theuwissen, D.W. McComb, P.D. Nellist,and V. Nicolosi: *Two-dimensional nanosheets produced by liquid exfoliation of layered materials*. Science **331**, no. 6017 (2011) 568-571.

[16] J. Yu, J. Li, W. Zhang, and H. Chang: *Synthesis of high quality two-dimensional materials via chemical vapor deposition*. Chemical Science **6**, no. 12 (2015) 6705-6716.

[17] D. Graf, F. Molitor, K. Ensslin, C. Stampfer, A. Jungen, C. Hierold, and L. Wirtz: *Spatially resolved Raman spectroscopy of single-and few-layer graphene*. Nano letters **7**, no. 2 (2007) 238-242.

[18] L. Britnell, R.M. Ribeiro, A. Eckmann, R. Jalil, B.D. Belle, A. Mishchenko, Y.-J. Kim, R.V. Gorbachev, T. Georgiou, S.V. Morozov, A.N. Grigorenko, A.K. Geim, C. Casiraghi, A.H.C. Neto, and K.S. Novoselov: *Strong light-matter interactions in heterostructures of atomically thin films*. Science **340**, no. 6138 (2013) 1311-1314.

[19] A.C. Ferrari, F. Bonaccorso, V. Fal'Ko, K.S. Novoselov, S. Roche, P. Bøggild, S. Borini et al: *Science and technology roadmap for graphene, related two-dimensional crystals, and hybrid systems*. Nanoscale **7**, no. 11 (2015) 4598-4810

[20] M.O. Li, D. Esseni, J.J. Nahas, D. Jena and H.G. Xing: Two-dimensional heterojunction interlayer tunneling field effect transistors (thin-tfets). IEEE Journal of the Electron Devices Society **3**, 3 (2015), pp.200-207

[21] J. Tian, T.-F. Chung, I. Miotkowski, and Y.P. Chen: *Electrical spin injection into graphene from a topological insulator in a van der Waals heterostructure*. arXiv preprint arXiv:*1607.02651* (2016).

[22] K. Vaklinova, A. Hoyer, M. Burghard, and K. Kern. *Current-induced spin polarization in topological insulator–graphene heterostructures*. Nano letters **16**, no. 4 (2016) 2595-2602.

[23] K.T. Lam, X. Cao, and J. Guo: *Device performance of heterojunction tunneling field-effect transistors based on transition metal dichalcogenide monolayer*. IEEE Electron Device Letters **34**, no. 10 (2013) 1331-1333.

[24] Z.J. Qi, S.J. Hong, J.A. Rodríguez-Manzo, N.J. Kybert, R. Gudibande, M. Drndic, Y.W. Park, and A. T. Johnson. *Electronic transport in heterostructures of chemical vapor deposited graphene and hexagonal boron nitride*. small **11**, no. 12 (2015) 1402-1408.

[25] R. Schlaf, C. Pettenkofer and W. Jaegermann: *Band lineup of a SnS_2/$SnSe_2$/SnS_2 semiconductor quantum well structure prepared by van der Waals epitaxy*. Journal of applied physics **85,** no. 9 (1999) 6550-6556.

[25] K.S. Novoselov, V. I. Fal, L. Colombo, P. R. Gellert, M. G. Schwab, and K. Kim: *A roadmap for graphene*. nature **490**, no. 7419 (2012) 192-200.

[26] C.H. Wong, H. An, and M. Pumera: *Electrochemical delamination and chemical etching of chemical vapor deposition graphene: contrasting properties*. The Journal of Physical Chemistry C **120**, no. 8 (2016) 4682-4690.

Chapter 2. The effect of Intermittent Oxygen Exposure on Chemical Vapor Deposition of Graphene

Abstract:

Chemical vapor deposition is the most proficient method for growing graphene on copper foils due to its scalability, repeatability, and uniformity, etc. Herein, we systematically study the effect of oxygen exposure on graphene growth. We introduced oxygen before and during the growth, and then studied its effects on the morphology, crystallinity, and nucleation density of graphene. We observe that introducing oxygen during growth significantly improves the graphene crystallinity while pre-dosing oxygen before growth reduces the graphene nucleation density. These studies suggest that intermittent oxygen exposure play a significant role in graphene growth, enabling scalable production of high quality graphene.

2.1. Introduction

Graphene, as one of many stable carbon (C) allotropes, is the two-dimensional (2D) arrangement of C atoms on a hexagonal lattice structure. Even though, theoretical studies of graphene went back to 1940s [1], the experimental work on graphene has started in 2004, by Geim and Novoselov and their discovery of isolation of single layer graphene by using so-called scotch tape method [2], and number of publications both experimental and theory are getting exponentially increased since then. Graphene is an exceptional material with its unique properties such as high electrical and thermal conductivity [3, 4], excellent

electronic mobility [5, 6], and mechanical strength [7] by far than any other materials. In graphene, four outer shell electrons make three σ bonds in plane and leaving one out of plane p_z orbital available for electronic conduction. These σ bonds formed by the sp^2 orbitals give graphene excellent mechanical and thermal properties. Graphene is around hundred times stronger than the strongest steel, and it is quite flexible. The highly mobile p_z orbital electrons are located above and below the graphene sheet, and they give graphene excellent electronic properties such as Dirac type energy dispersion, high mobility, etc. Dirac type energy dispersion in graphene implies that electrons have zero effective mass, and lack of electronic bandgap enables ballistic carrier transport around symmetry points.

Graphene can be synthesized by using different methods such as chemical vapor deposition (CVD) [8], epitaxial graphene growth on silicon carbide (SiC) [9], electrochemical exfoliation [10, 11], and micromechanical exfoliation [2] from bottom-up to top-down approaches, that vary the product in quality, size and quantity according to the purpose of applications. The optimization of synthesis of graphene is going to promote and shape technological advancements in materials science integrated application platform which demand large scale, high quality, and uniform graphene in order to utilize devices in cutting-edge nanoscale electronics, optics, spintronics, etc. CVD grown graphene on copper (Cu) substrate is the most promising, prevalent materials source for device fabrication process by its compatibility with academic and industrial demand.

CVD is the most studied graphene production method for building the prototypes of next-generation electronic devices thanks to its scalability; however, there is still not an ultimate consensus of growth mechanisms on control the size and morphology of

synthesized-crystals. The varying results in different laboratories imply the necessity to reach better optimization to enhance materials processing. Graphene synthesis by CVD employs the formation process through primarily the nucleation and growth of C atoms on the surface of Cu right after the thermal decomposition of hydrocarbon precursors. The details of nucleation of C atoms on Cu surface and kinetics of gaseous species determine the quality of graphene. Significant improvement has been achieved in graphene growth by investigating fundamental variables. Han et al. have found that graphene growth is affected by Cu surface morphology as smooth surface lowers nucleation density and yields larger graphene domains [12]. The effect of base pressure of CVD growth of graphene regulates the coverage as the higher sublimation rate of Cu leads to desorption of C adatoms, hence reduces the graphene nucleation density in low pressure CVD, while the Cu desorption in atmospheric pressure CVD is negligible due to higher activation energy [13]. The effect of hydrogen (H_2) exposure on graphene growth forms the morphology and thickness as the lower dosage of H_2 would manage the multiple layer graphene formation quickly, then succeeding high dosage of H_2 for etching to single layer graphene [14]. The surface oxygen and oxygen (O_2) exposure before the growth of graphene reduce the graphene nucleation density by passivating Cu surface [15].

In this work, we systematically investigate the effect of O_2 on the CVD growth of graphene in a single zone split horizontal quartz tube furnace. The O_2 gas with varying concentrations is introduced into the quartz reaction chamber during the different steps of the thermal process. The detailed characterization of the morphological, structural and

chemical properties has been performed by various microscopic and spectroscopic techniques.

2.2. Methods

2.2.1. Materials synthesis

Electropolishing of Cu foils: It is well-understood procedure that the smoothing of Cu foils prior to growth helps to improve the quality of graphene [16]. We cut (wrinkle-freely) Cu foils 2 cm x 1.5 cm x 20 μm in dimensions and set as an anode, then immersed the Cu foil in a solution with the larger and thicker Cu foil set as a cathode in a homemade electrochemistry cell. The electrochemical solution consists of 500 mL deionized (DI) water, 250 mL phosphoric acid (H_3PO_4), 250 mL ethanol (C_2H_6O), 50 mL isopropyl alcohol (IPA: C_3H_80), and 10 g urea (CH_4N_2O). A direct current (DC) power supply was used to apply 0.7 A of current at 2.7 V of potential for 100 sec. After electro-polishing, the Cu foil was rinsed with DI water, further washed with IPA, and then blow- dried with nitrogen.

CVD of Graphene on Cu foils: The graphene samples were grown by CVD method using three different recipes, referred as recipe I, recipe II, and recipe III. Briefly, the furnace was heated up to 1000 °C with the heating ramp of 25 °C min^{-1} under a gas mixture of H_2 (100 sccm) and Ar (400 sccm), and the growth pressure of 15 Torr was maintained during the entire process in all recipes. While the graphene samples were grown without introducing O_2 in recipe I, O_2 was introduced into the system before and during the growth of the graphene, respectively, for recipe II, and recipe III.

The thermal steps for chemical vapor deposition (CVD) growth of graphene on copper (Cu) foils are schematically illustrated in **Fig. 2.1**, and the corresponding growth parameters for each step are summarized in **Table 2.1**, **2.2**, and **2.3** as the thermal recipes I, II, and III, respectively**.** Briefly, recipe I excludes the oxygen (O_2) exposure either before or during the growth step. Only recipe II includes the O_2 exposure between the annealing step and growth step, referred as O_2 annealing in Table S2. Recipe III employs the O_2 exposure during the growth. The different O_2 exposures (0, 1, 3, 5, 7, 9, 10, and 20 sccm) in the main manuscript are grown based on recipe III.

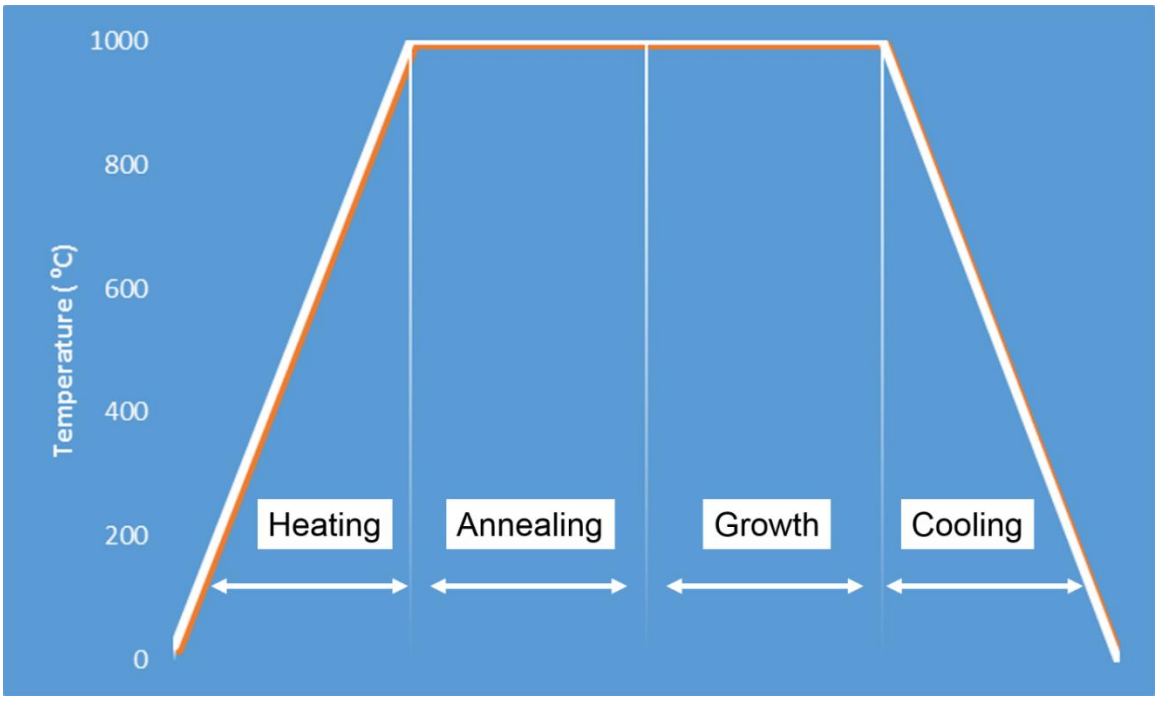

Figure 2.1. Schematic of thermal steps of CVD growth of graphene on Cu.

Table 2.1. Parameters of recipe I for CVD growth of graphene on Cu.

Thermal Recipe I					
CVD Step		**Heating**	**Annealing**	**Growth**	**Cooling**
Temperature (°C)		24 to 1000	1000	1000	1000 to 24
Time (min)		40	10	0.5	45
Pressure (Torr)		15	15	15	15
Gas Flow (sccm)	**Ar**	400	400	0	400
	H_2	100	100	100	100
	O_2	0	0	0	0
	CH_4	0	0	10	0

Table 2.2. Parameters of recipe II for CVD growth of graphene on Cu.

Thermal Recipe II						
CVD Step		**Heating**	**Annealing**	**O_2 Annealing**	**Growth**	**Cooling**
Temperature (°C)		24 to 1000	1000	1000	1000	1000 to 24
Time (min)		40	10	2	0.5	45
Pressure (Torr)		15	15	15	15	15
Gas Flow (sccm)	**Ar**	400	400	0	0	400
	H_2	100	100	100	100	100
	O_2	0	0	5	0	0
	CH_4	0	0	0	10	0

Table 2.3. Parameters of recipe III for CVD growth of graphene on Cu.

Thermal Recipe III					
CVD Step		**Heating**	**Annealing**	**Growth**	**Cooling**
Temperature (℃)		24 to 1000	1000	1000	1000 to 24
Time (min)		40	10	2	45
Pressure (Torr)		15	15	15	15
Gas Flow (sccm)	**Ar**	400	400	0	400
	H_2	100	100	100	100
	O_2	0	0	5	0
	CH_4	0	0	10	0

Transfer of Graphene from Cu foils to SiO_2/Si substrates: The grown graphene was transferred from Cu foil to the final substrate by electrochemical delamination method[17]. The transfer experiment was started with spin coating of Poly (methyl methacrylate) (PMMA: $(C_5O_2H_8)_n$) on graphene/Cu sample as a supporting layer. Next, we let the PMMA to dry 30 minutes under white light or bake it on a hot plate at 180 °C for 90 seconds. Electrolysis process took place in a homemade electrolytic cell by setting the trio of PMMA/graphene/Cu as a cathode while thick graphitic rod as an anode, and applying 1.7-2.1 V electrode potential in a solution 1M of sodium hydroxide (NaOH). After separation from Cu, the PMMA/graphene was fished out of solution to deionized water bath to cleanse the residual solution. PMMA/graphene were later transported to SiO_2/Si (300 nm thick oxide), and dried up at 65 °C before acetone (C_3H_6O) cleaning. After removing the PMM layer by acetone washing, we completed transfer process with IPA rinsing and dry nitrogen blowing.

2.2.2. Materials characterization

X-ray photoelectron spectroscopy (XPS) characterization of graphene on Cu substrate was carried out using a Kratos AXIS ULTRADLD XPS system equipped with an Al Kα monochromated X-ray source, and a 165- mm mean radius electron energy hemispherical analyzer. The size of slot for XPS is 300 μm x 700 μm. The vacuum pressure was kept below $3x10^{-9}$ Torr, and the neutralizer was applied during the data acquisition. Microstructural analyses of graphene on Cu substrates were done by the FEI NNS450 scanning electron microscopy (SEM). Raman spectra of graphene on SiO_2 / Si substrate were collected using a Horiba system with a 532 nm excitation laser (<2 mW excitation power, 100X objective lens).

2.3. Results and discussion

As described in methods, graphene islands were grown on the Cu foils by CVD using three different recipes, recipe I, II, and III, to establish a conclusive comparison of the effects of the O_2 that is introduced in the different stages of the thermal process with varying flow rates on the CVD growth of graphene. It should be noted that the graphene was intentionally grown in the form of islands, allowing us to understand how the O_2 affects the shape, density and thickness of the individual islands of graphene.

As a starting point, we characterized the graphene islands on the Cu foils by SEM. **Fig. 2.2 a** and **2.2 b** show the SEM images of the graphene islands grown by recipe I and recipe II, respectively. The graphene islands can be easily distinguished from the Cu foils thanks to their sharp contrast to the Cu foils. Recipe I provides higher surface coverage of the graphene islands than that of the islands obtained by recipe II. Specifically, the density

of the graphene islands is calculated to be ~ 0.164 and 0.054 μm^{-2} for recipe I, and recipe II, respectively. The decrease in the density of the graphene islands with the O_2 exposure can be attributed to the passivation of the Cu surface, and thus reducing the nucleation sites[15].

We further investigated the role of O_2 introduced during the growth step in the growth of the graphene islands, which has not been studied to date. **Fig. 2.2 c** and **2.2 d** show the SEM images of the graphene islands grown by recipe II using 3 sccm and 5 sccm of O_2 flow, respectively. The O_2 is introduced to the reaction chamber in cooperation with CH_4 and H_2 during the growth. The presence of O_2 during the growth yields more uniform coverage for O_2 flow of 3 sccm and 5 sccm (0.062 and 0.067 flake / $(\mu m)^2$) in **Fig. 2.2 c**, and **2.2 d,** respectively. The comparison of **Fig. 2.2 c** and **2.2 d** points out that the O_2 exposure during growth is optimized at the flow rate of 5 sccm, since **Fig. 2.2 d** represents the most uniform coverage and thickness distribution of graphene islands.

We conclude that O_2 exposure on the Cu foil before the growth substantially reduce the density of the graphene islands, while the O_2 during growth does this. This results will pave the way. As the amount and step of exposure of O_2 differs, the coverage and uniformity of graphene islands significantly changes.

Raman spectroscopy is a non-destructive tool commonly used for the characterization of graphene as well as other 2D materials [17-24]. Raman spectroscopy is further performed to obtain information about the thickness and crystallinity of the graphene islands that are transferred onto SiO2/Si substrates. Typical Raman modes as namely D (disorder band or defect band), G (in-plane vibrational mode), and 2D (second

order overtone of the D band) of the graphene islands grown with different O2 flow rates are shown in **Fig. 2.3 a**. Particularly, the Raman mode frequencies are located at 1340, 1587, and 2678 cm-1 for D, G, and 2D bands, respectively, for the top panel. The weaker Raman D band is an indication of lesser defective graphene structure. The graphene islands, which are grown in the presence of O_2 exposure during the growth step, exhibit negligible Raman D band, and this exemplifies highly crystalline structure.

The intensity ratio of Raman 2D and G band is utilized to evaluate the thickness and quality information of graphene. The 2D / G band intensity ratio of the graphene islands grown with O_2 flow rate of 5 sccm is significantly higher than the samples grown with O_2 flow rate of 3 sccm, and much higher than the growth held in the absence of O_2 flow. The 2D / G band ratio with various O_2 exposure rates are plotted in **Fig. 2.3 b**. The highest 2D/G intensity ratio value is measured for graphene islands grown with O_2 flow of 5 sccm. The high Raman 2D/G band intensity ratio of the samples, which are grown with O_2 flow during growth step, is the clear confirmation of single layer, and high quality (close to the value of micromechanically exfoliated) graphene [25]. The sharpness of 2D Raman band is an indicator of crystallinity; peaks are getting sharper as the crystal quality of the graphene island increases. The Raman 2D band full width half maximum (FWHM) with the different O_2 exposures is plotted in **Fig. 2.3 c**. The lowest (28.4 cm^{-1}) value of 2D Raman band FWHM is measured for the graphene islands grown by O_2 flow rate of 5sccm. The sharp Raman 2D band signifies that high quality graphene islands are synthesized with the O_2 exposure during the growth step. We observe that the excessive O_2 flow (20 sccm) during the growth damages the quality of graphene by yielding defective and thicker

crystals, **Fig. 2.4**. The Raman 2D / G band ratio and FWHM values are summarized in **Table 2.4**. The Raman spectroscopy analysis on graphene designates the favorable growth with the O_2 flow of 5 sccm by recipe III. The extensive Raman spectroscopy of graphene grown with more or lesser O_2 flow rates are plotted in **Fig 2.5-2.8.**

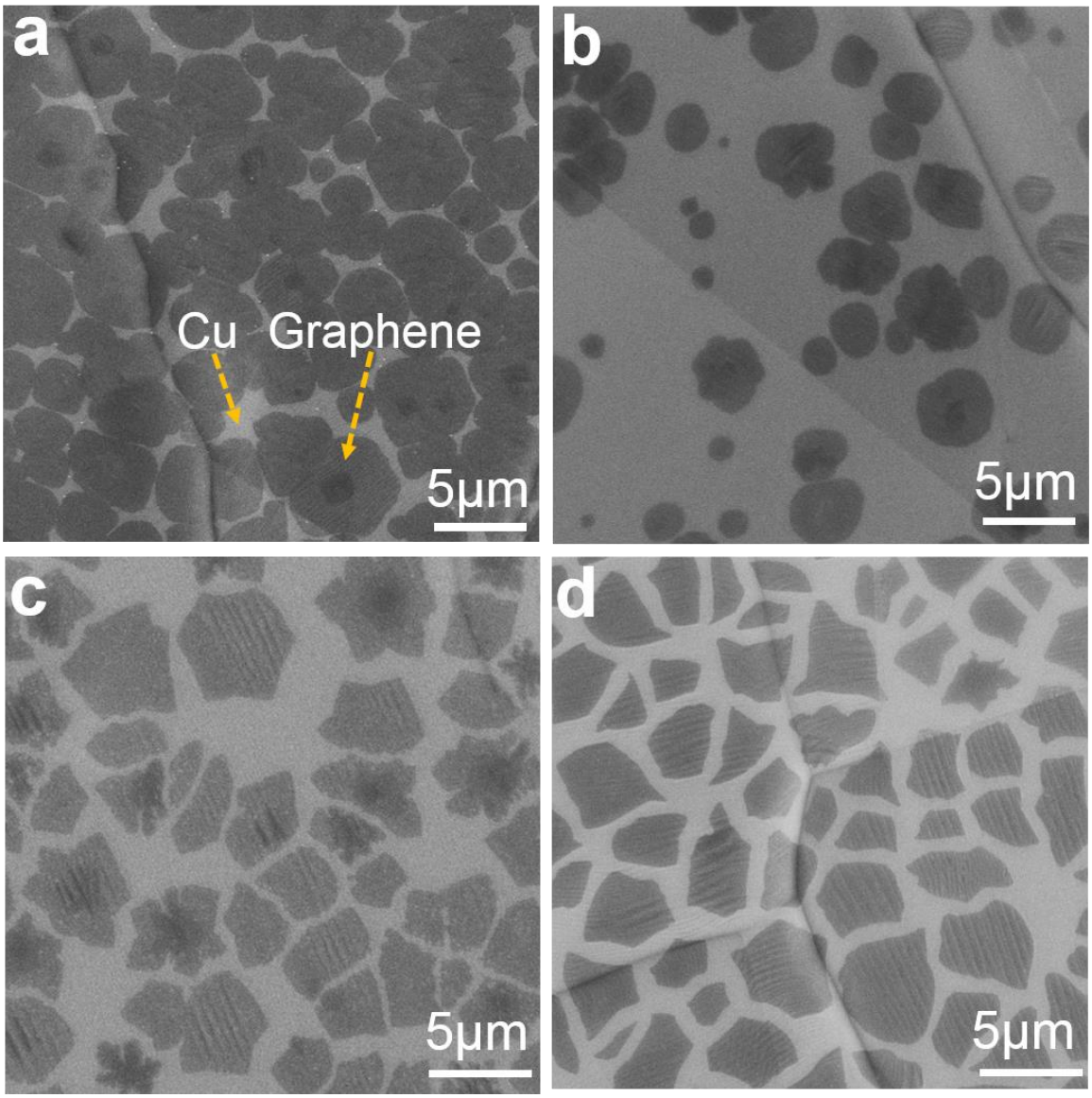

Figure 2.2. Surface morphology of graphene islands. SEM images of the graphene islands grown on the Cu foils by recipe I (a) and recipe II (b). SEM images of the graphene islands grown by recipe III using the O_2 flow of 3 sccm (c) and 5 sccm (d).

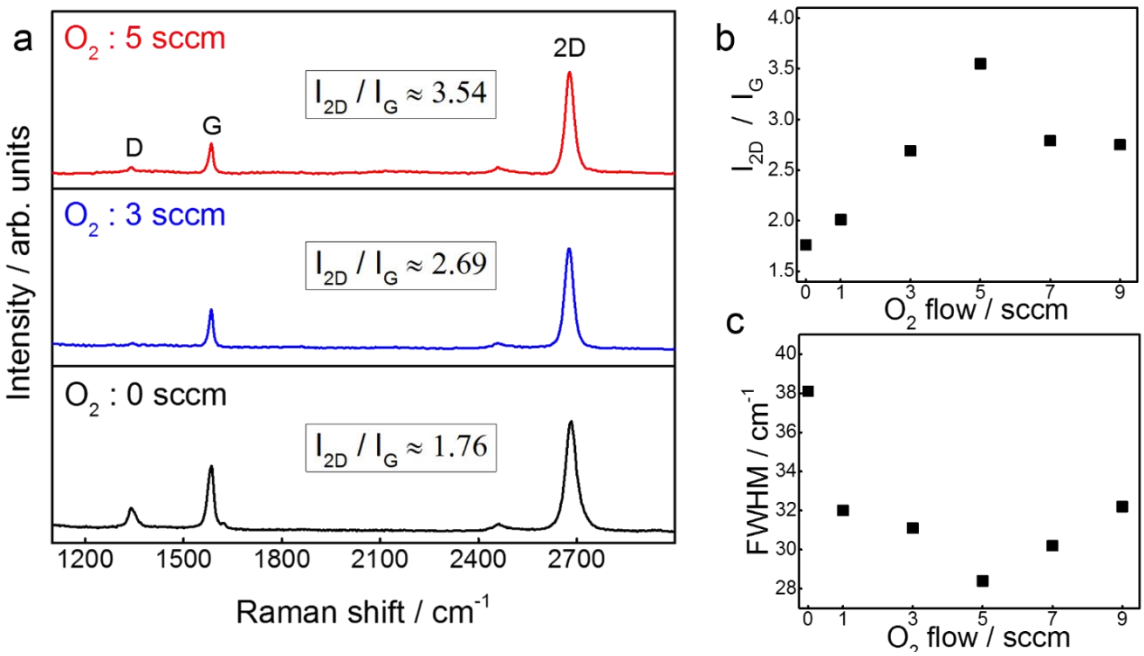

Figure 2.3 Raman spectroscopy characterization of graphene islands. Raman spectra comparison (a), intensity ratio of the 2D and G Raman peaks (b), and FWHM of the 2D peak (c) for the graphene islands grown under varying concentrations of O_2.

In **Table 2.4**, we have recapitulated the results of Raman spectra of graphene grown with different parameters. The intensity ratio of Raman 2D and G bands gives information about the thickness of graphene, as the ratio is higher, thinner the graphene. The sharpness of 2D band also signify the quality and thickness, as sharper the 2D band, better the quality of graphene. Based on the results on Table S4, O_2 exposure of 5sccm during the growth gives the best results in terms of quality and single layer graphene production.

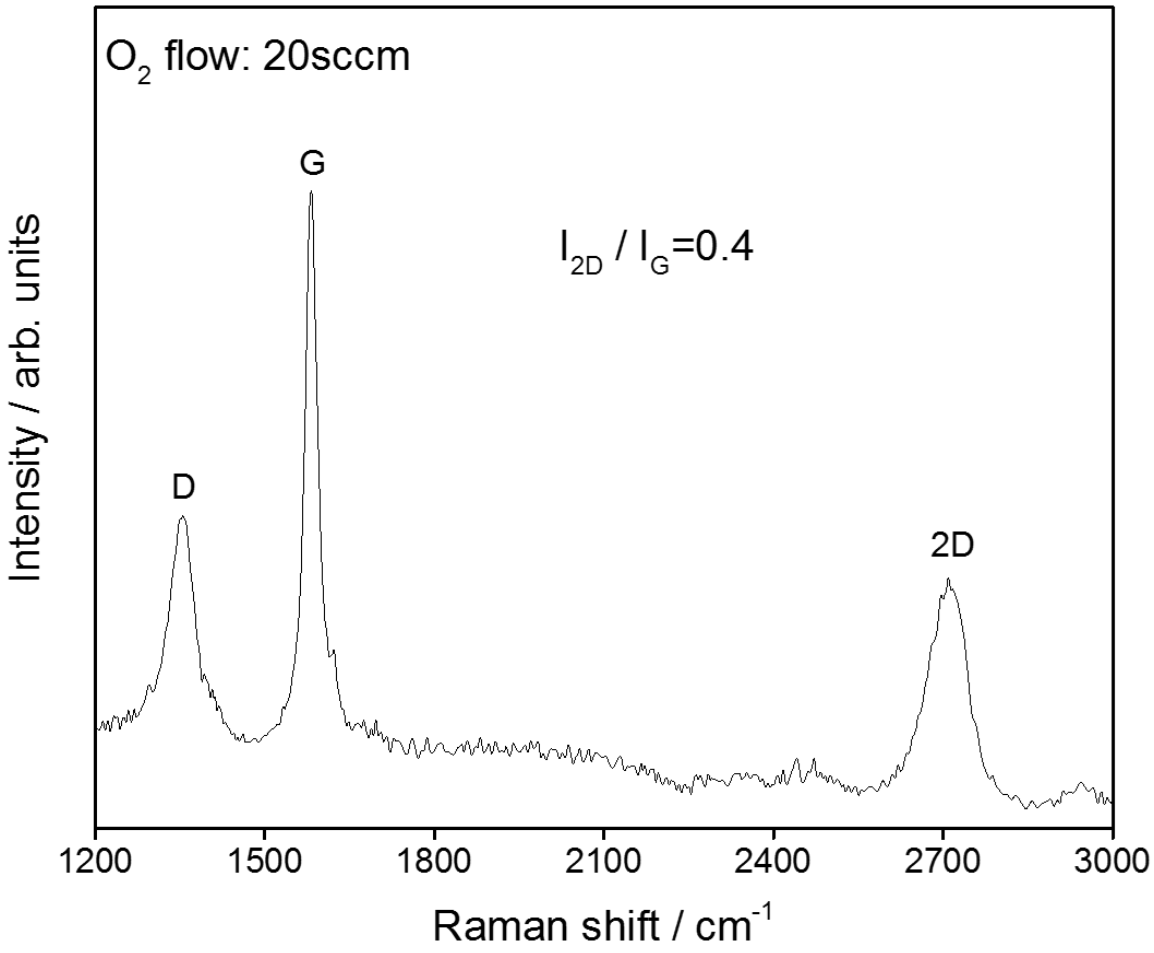

Figure 2.4. Raman Spectra of graphene grown under 20 sccm O_2 exposure.

Table 2.4. Summary of the results of Raman spectra of CVD grown graphene islands.

O_2 Exposure	Raman G Band (cm^{-1})	Raman 2D Band (cm^{-1})	I_{2D} / I_G	FWHM
Zero O_2 flow	1584	2681	1.76	38.1
Before growth (5sccm)	1585	2677	2.85	30.6
During growth (1sccm)	1583	2683	2.01	32.0
During growth (3sccm)	1584	2677	2.69	31.1
During growth (5sccm)	1587	2678	3.54	28.4
During growth (7sccm)	1588	2680	2.79	30.2
During growth (9sccm)	1588	2681	2.75	32.2
During growth (10sccm)	1584	2678	2.87	32.7
During growth (20sccm)	1582	2707	0.40	77.6

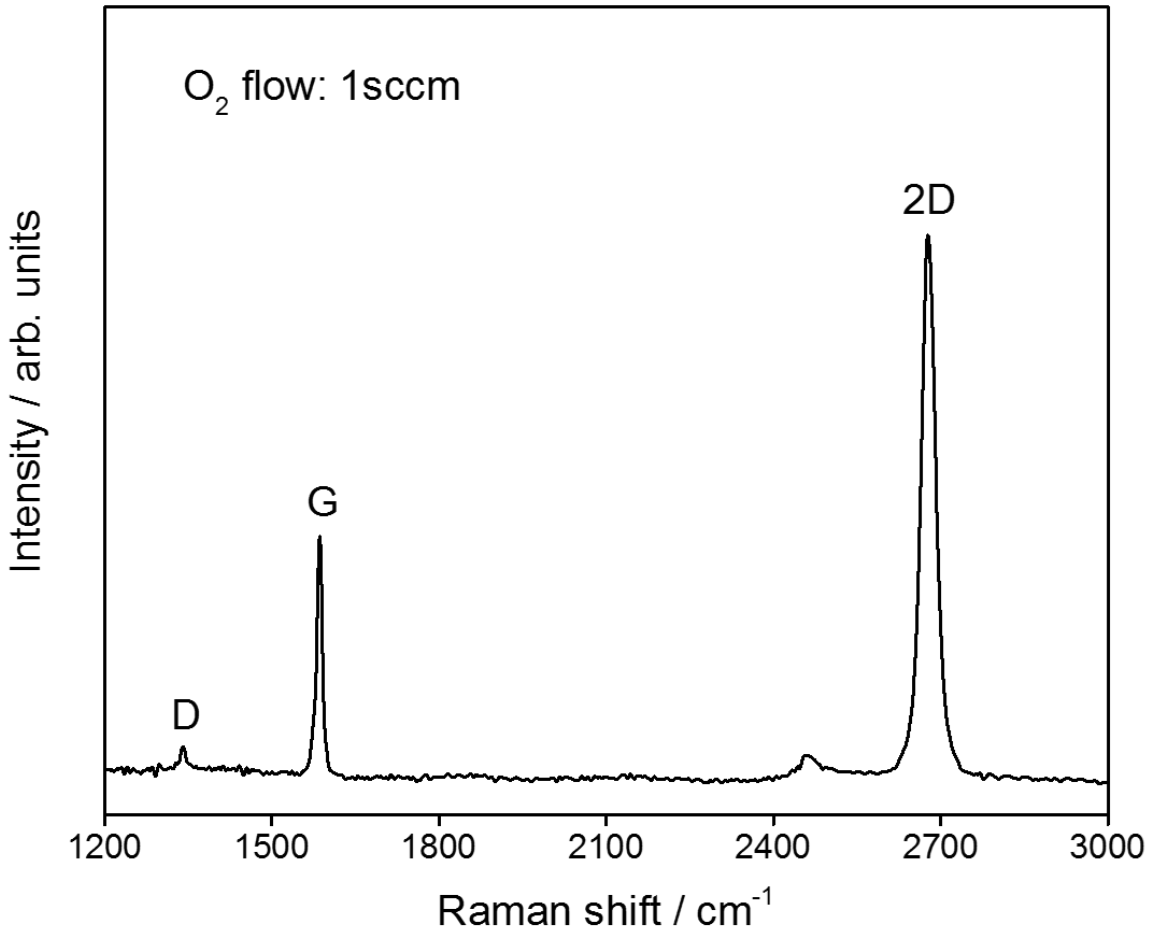

Figure 2.5. Raman spectra of graphene grown by recipe III, O_2 flow of 1sccm.

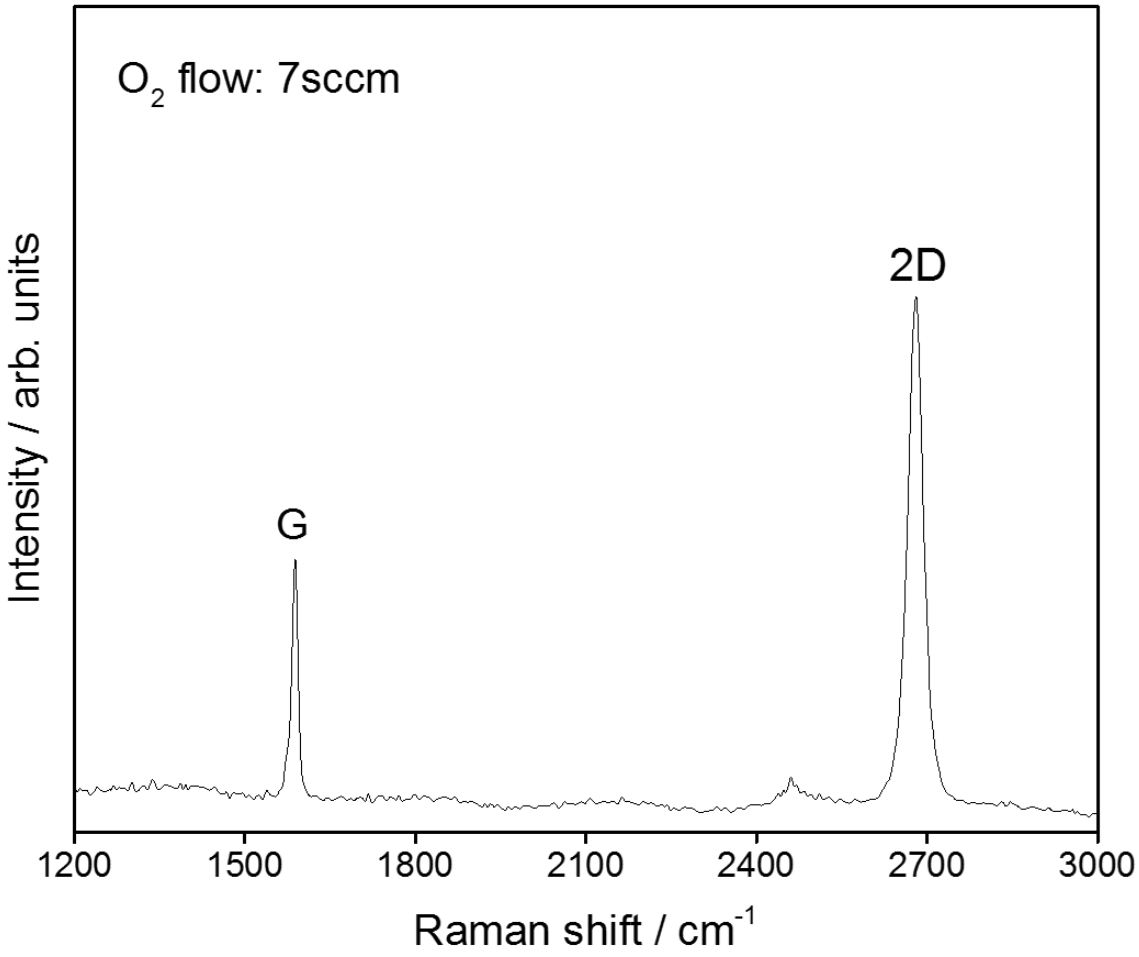

Figure 2.6. Raman spectra of graphene grown by recipe III, O_2 flow of 7sccm.

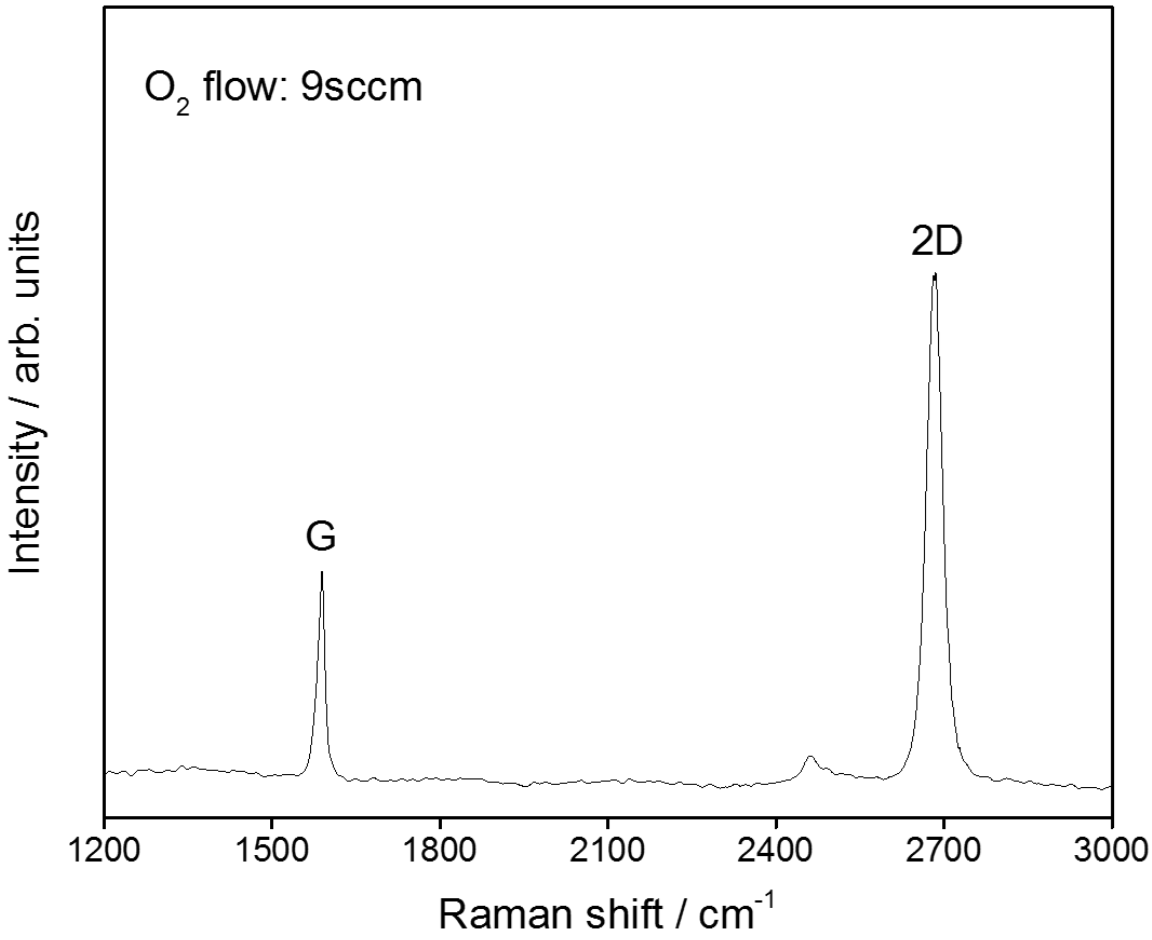

Figure 2.7. Raman spectra of graphene grown by recipe III, O_2 flow of 9 sccm.

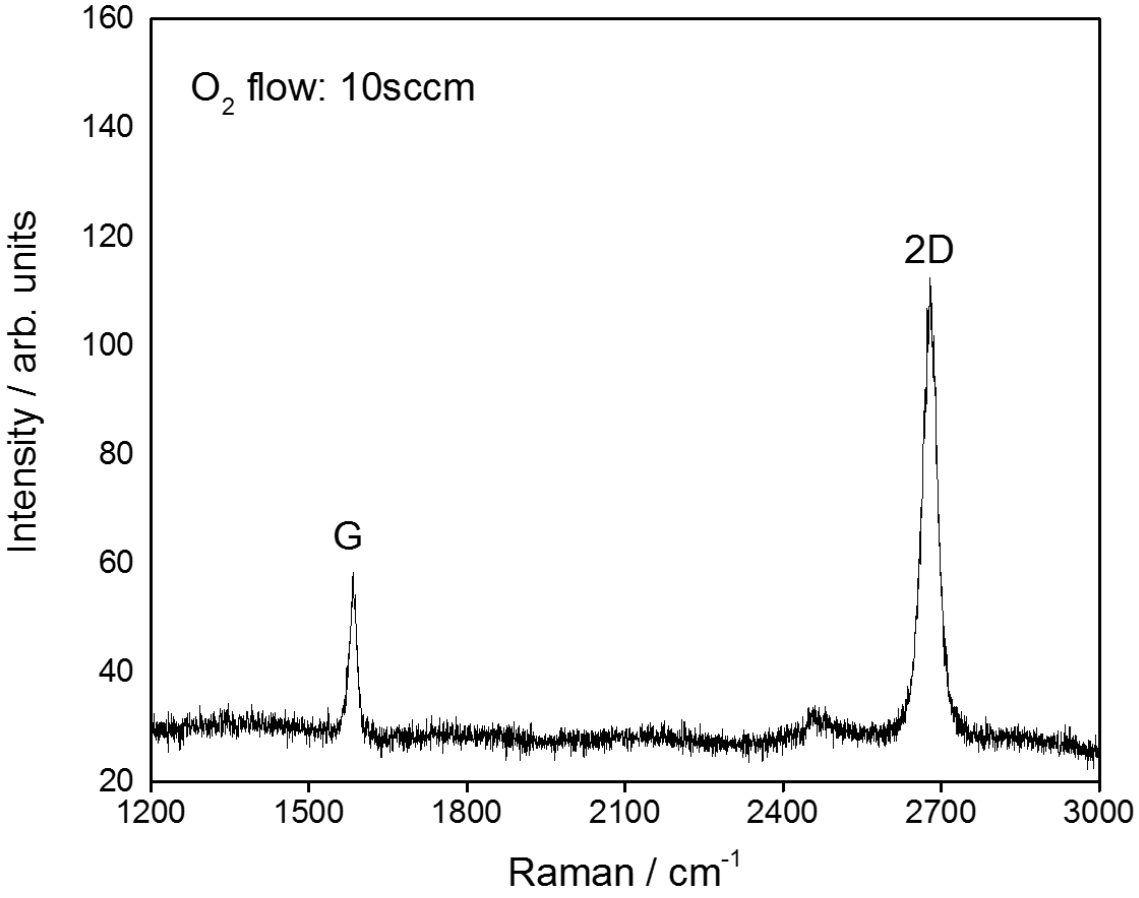

Figure 2.8. Raman spectra of graphene grown by recipe III, O_2 flow of 10sccm.

Raman mapping of the 2D band intensity has been proven to be useful for thickness identification of graphene [26]. The optical microscopy images and corresponding Raman mappings of the graphene islands grown by three different recipes, which are transferred on the SiO_2/Si substrates, are displayed in **Fig. 2.9**. We observe that recipe I provides the graphene islands with a thickness ranging from single to a few layers as seen in **Fig 2.9a**, and **2.9d**. The graphene islands consisting single to bilayers are obtained by recipe II, as shown in **Fig. 2.9b**, and **2.9e**. Introducing O_2 just before the growth relatively improves the thickness uniformity of the graphene islands. On the other hand, the graphene islands

grown by recipe III, in which O_2 is introduced during the growth, have a uniform monolayer thickness in **Fig 2.9c** and **2.9f**. We find that O_2 exposure during the growth plays a key role to achieve complement uniformity of the graphene islands synthesized by CVD. The Raman mapping confirms that the recipe III with 5sccm O_2 flow yields uniform single layer thickness distribution through Cu surface for graphene production. The Raman spectroscopies taken from different regions of the graphene islands as center, edge, and between edge and center verify the thickness classification made based on Raman mappings of different samples, in **Fig 2.10-2.12**.

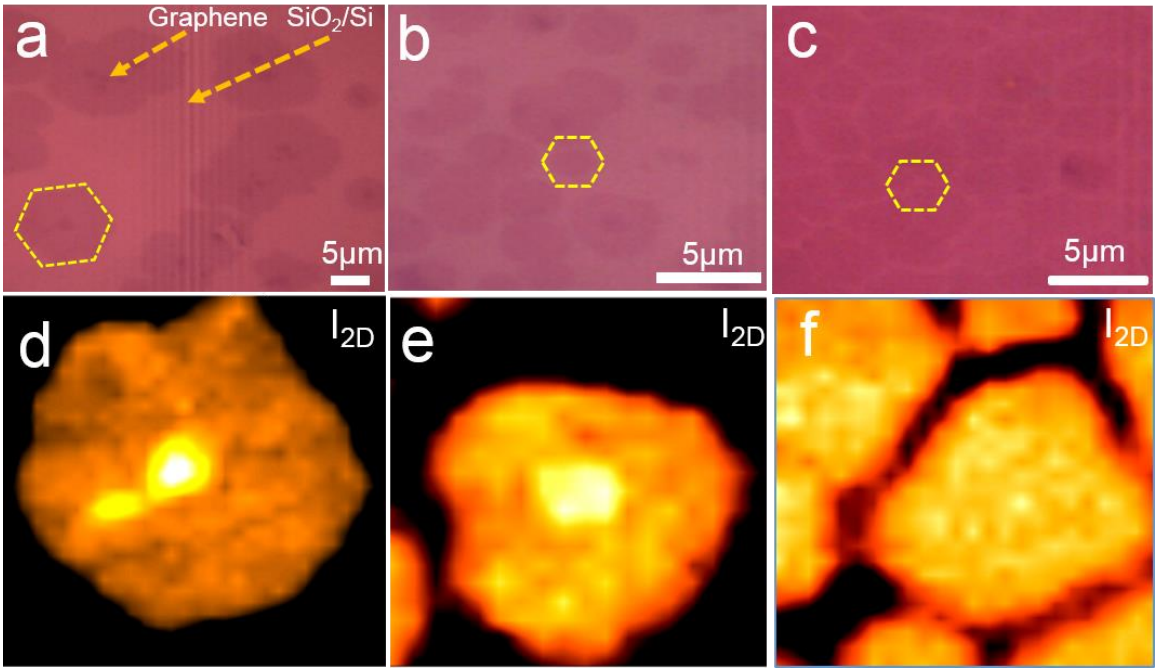

Figure 2.9. Raman imaging of graphene islands. Optical images and corresponding Raman mappings of the graphene islands grown by recipe I (a, d), recipe II (b, e), and recipe III (c, f), respectively.

Fig. 2.10 represents the optical image (**Fig. 2.10a**), Raman mapping (**Fig. 2.10b**), and Raman spectra (**Fig. 2.10.c**) taken from three different regions as green curve for

center, blue curve for edge, and red curve between center and edge of graphene island grown by recipe I (No O_2 exposure involved), and also illustrated at Fig. 2.9a, d. The **Fig. 2.10c** shows that the center region consists of few layers, the edge region is single layer, and between center and edge region is single or two layers of graphene.

Fig. 2.11 represents the optical image (**Fig. 2.10a**), Raman mapping (**Fig. 2.10b**), and Raman spectra (**Fig. 2.10c**) taken from three different regions as green curve for center, blue curve for edge, and red curve between center and edge of graphene island grown by recipe II (O_2 exposure after annealing and before growth as 5sccm), and also illustrated at Fig. 2.9b, e. The **Fig. 2.9c** shows that the center region consists of two or three layers, the edge region is single layer, and between center and edge region is one or two layers.

Fig. 2.12 represents the optical image (**Fig. 2.12a**), Raman mapping (**Fig. 2.12b**), and Raman spectra (**Fig. 2.12c**) taken from three different regions as green curve for center, blue curve for edge, and red curve between center and edge of graphene island grown by recipe III (O_2 exposure during growth as 5sccm), and also illustrated at Fig. 2.9c, f. The **Fig. 2.12c** shows that the center region, the edge region, and between center and edge region is single layer uniformly.

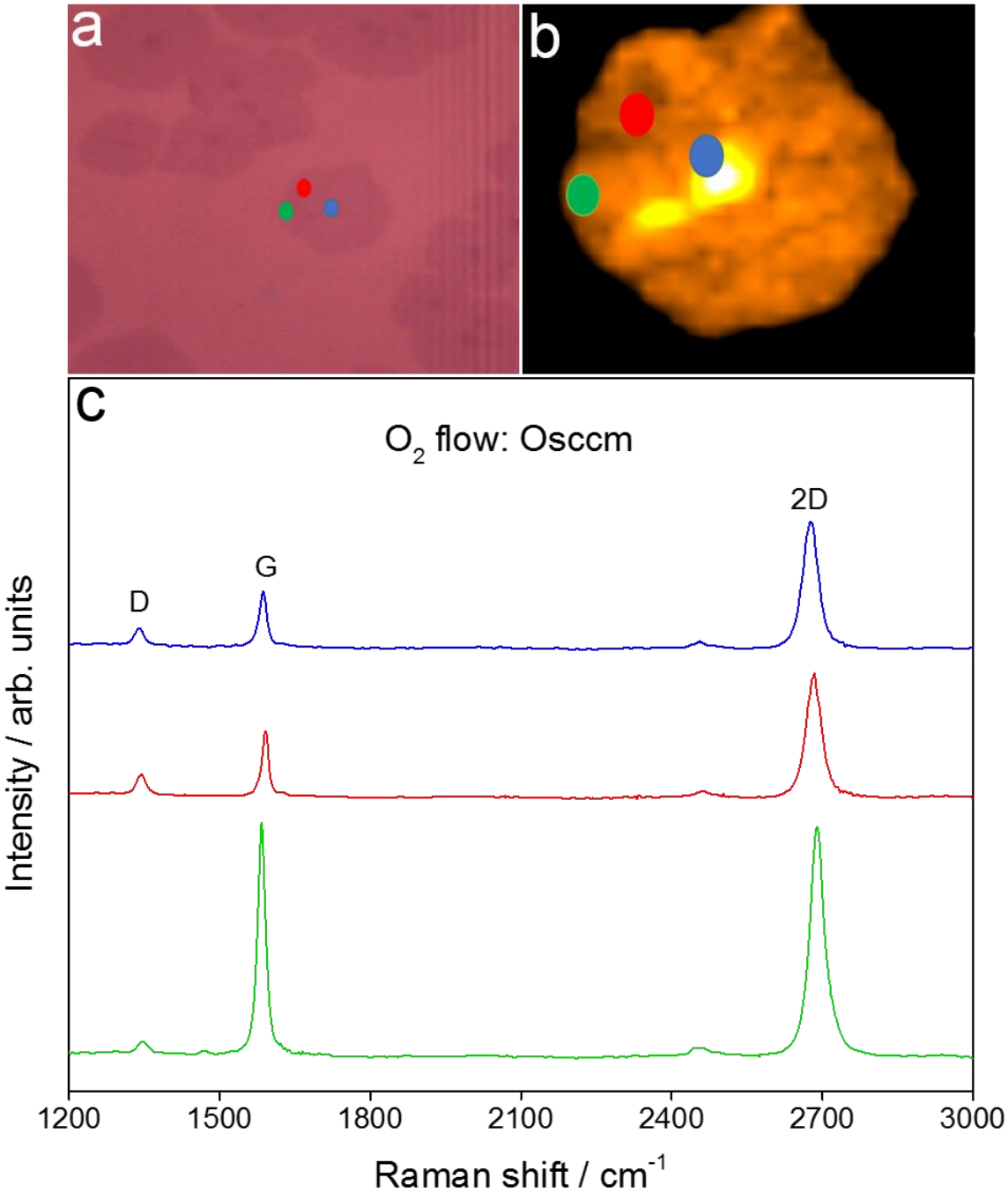

Figure 2.10. Optical image (a), Raman mapping (b), and Raman spectra (c) taken form the different areas of graphene islands grown with recipe I.

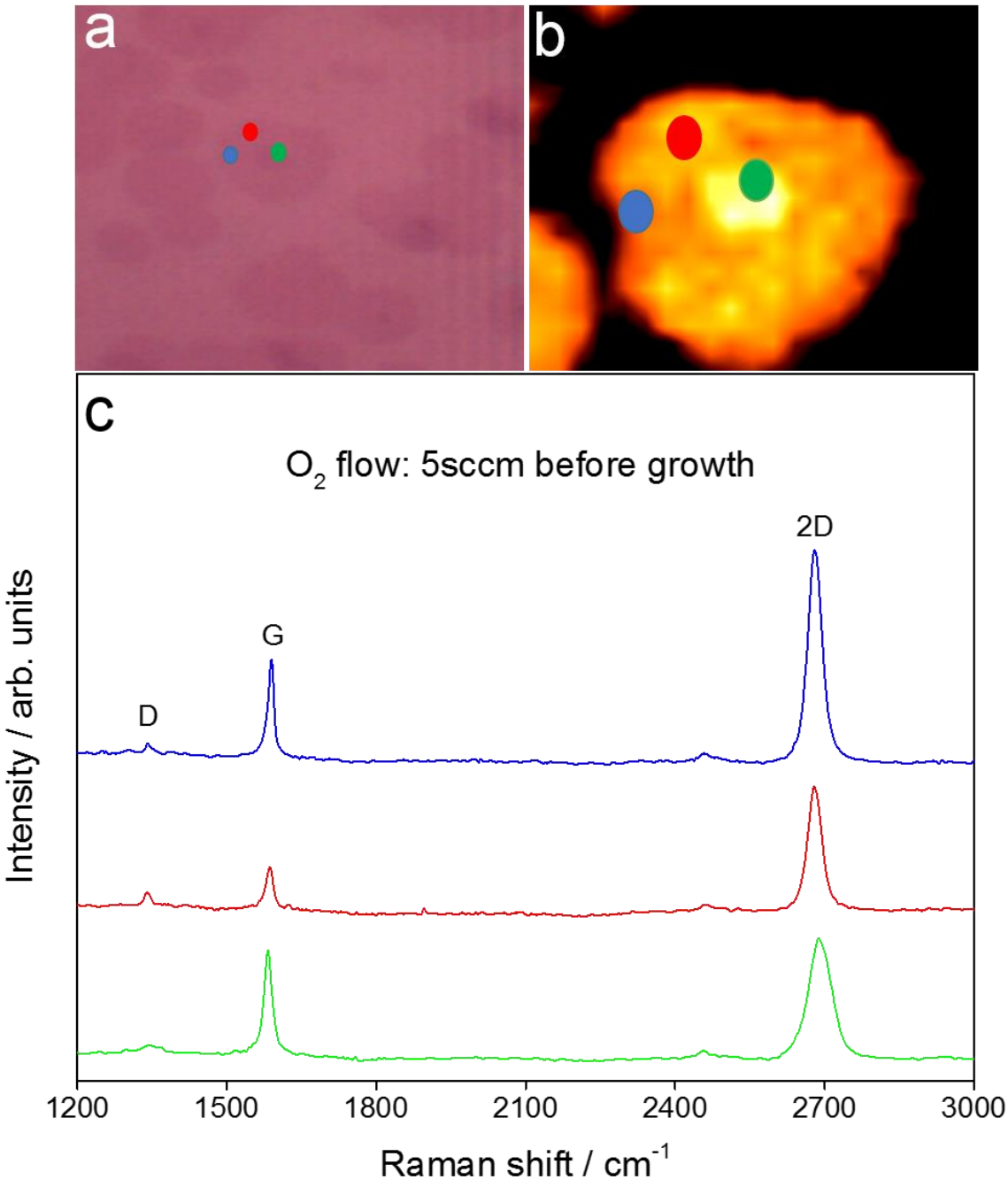

Figure 2.11. Optical image (a), Raman mapping (b), and Raman spectra (c), taken form the different areas of graphene islands grown with recipe II.

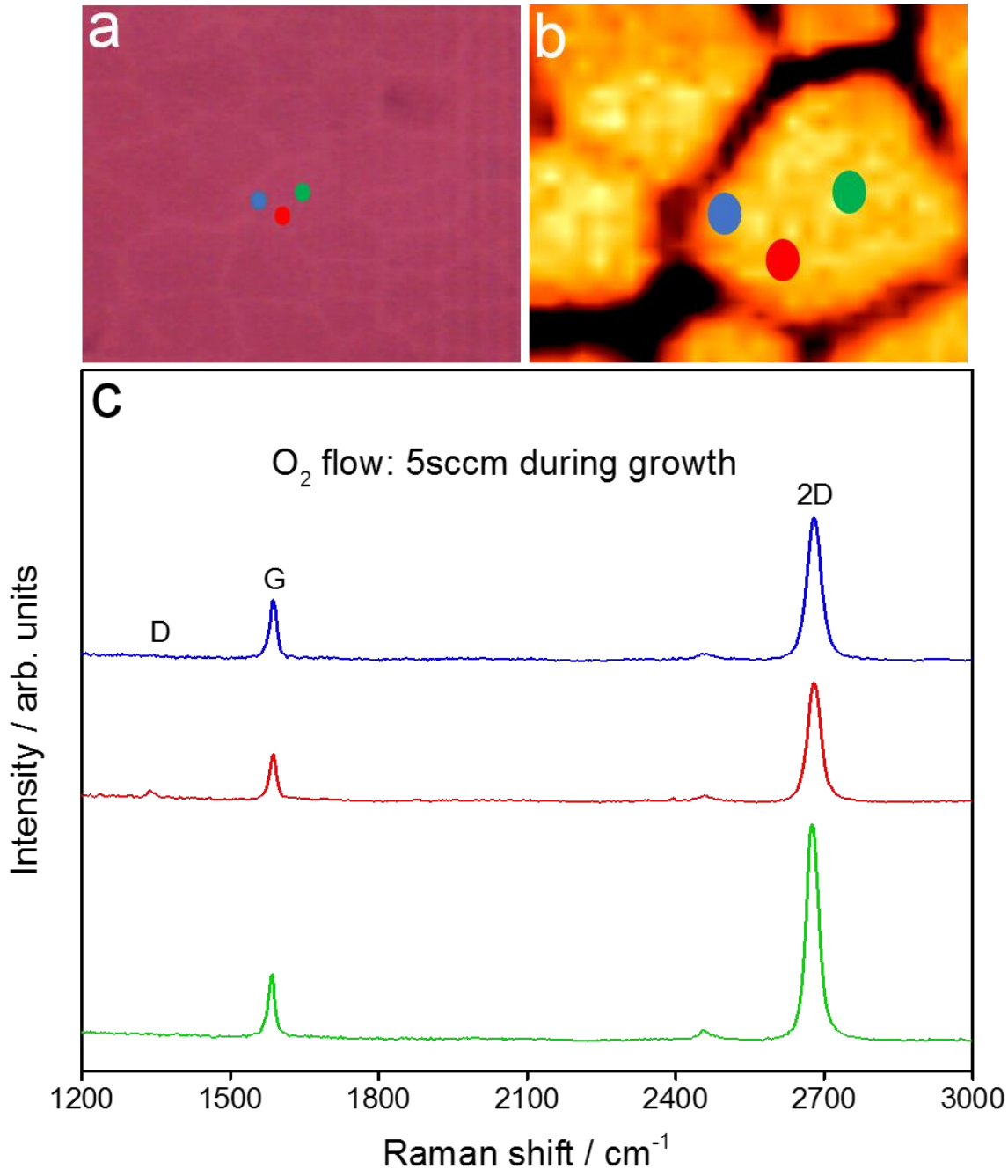

Figure 2.12. Optical image (a), Raman mapping (b), and Raman spectra taken form the different areas of graphene islands grown with recipe III.

The surface chemistry of the graphene islands and Cu foils are investigated by XPS analysis [27]. The XPS survey spectra of the graphene islands grown by recipe III and O_2 flow of 5 sccm reveals only C, Cu, and O elements are present on the surface, **Fig. 2.13**. X-Ray Photoemission spectroscopy (XPS) of graphene provides information about surface chemistry of product. The XPS survey spectra of the graphene islands grown by O_2 exposure of 5sccm during the growth is added to show the surface chemistry behavior of graphene samples grown with the ideal recipe. The C 1s core level peak of graphene shows no sign of sp^3 binding, which implies defect free, high quality production, **Fig. 2.14**. The higher C 1s peak on the graphene islands grown with O_2 flow of 0 sccm than O_2 flow of 5 sccm indicates higher graphene coverage with the absence of O_2 exposure as a comparison between recipes I with recipe III. The C 1s peak is located at the binding energy (B.E.) of 284.6, while it is shifted to higher B.E. by 0.3 eV after graphene deposition. The XPS spectrum also tells us none or negligible amount of O_2 bonded to graphene with changing exposure rates, which is an indication that changing O_2 exposure does not change the surface chemistry of graphene but affects the growth conditions. The XPS spectra presents C 1s peaks of the graphene samples grown by recipe III under O_2 flow of 5sccm and 20 sccm, fig 2.14. It is clearly seen that excessive O_2 exposure (20 sccm) leads the syntehsis of the thicker graphene islands compare with monolayer graphene islands grown with O_2 flow of 5 sccm during the growth step, **Fig. 2.15**. It is clearly seen that O_2 exposure of 20 sccm gives much higher (approximately four fold) C 1s peak than O_2 exposure of 5 sccm, and it indicates that 20 sccm growth yields multiple layers of graphene in contrary to uniform single layer graphene by O_2 flow of 5sccm.

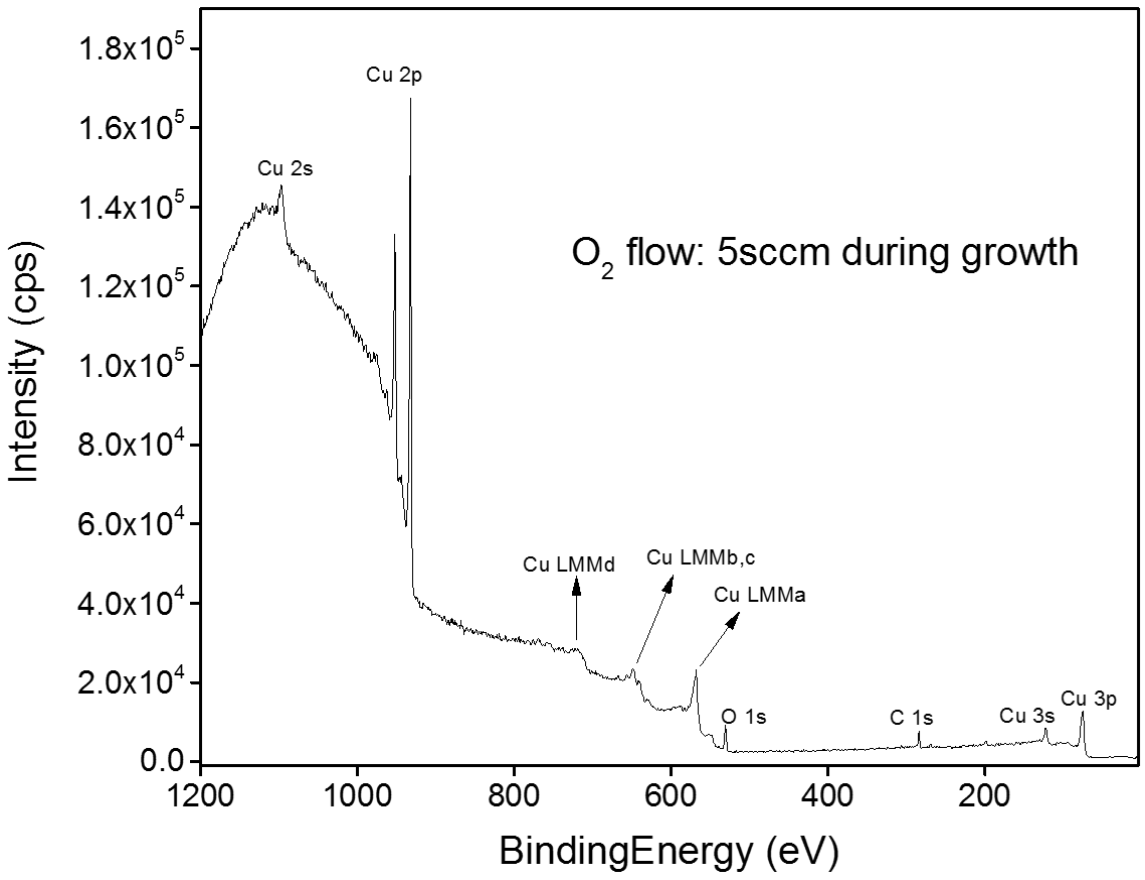

Figure 2.13. XPS survey spectra of graphene grown with O_2 flow of 5sccm on Cu.

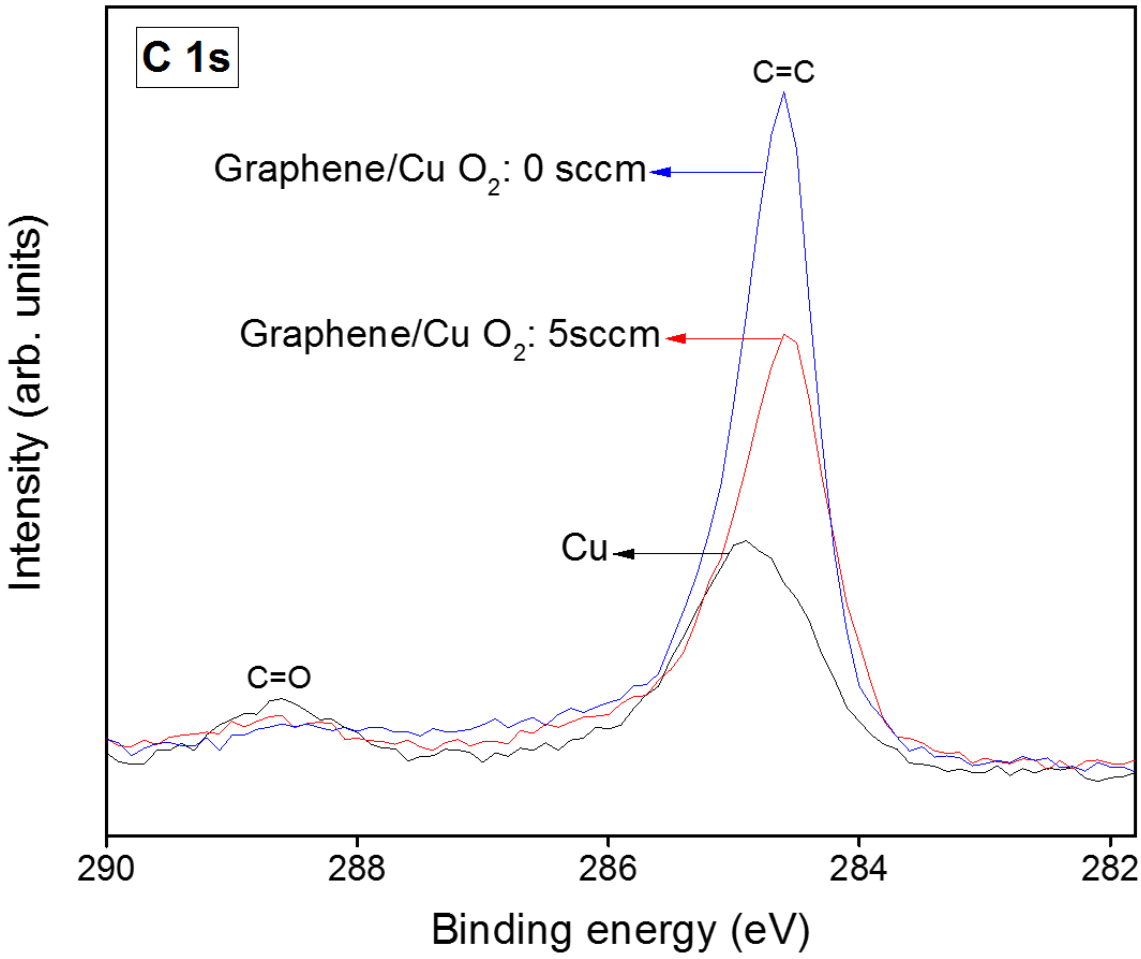

Figure 2.14. Surface chemistry of graphene islands. The XPS C 1s core levels of the Cu foil, and the graphene islands grown by recipe I, and recipe III.

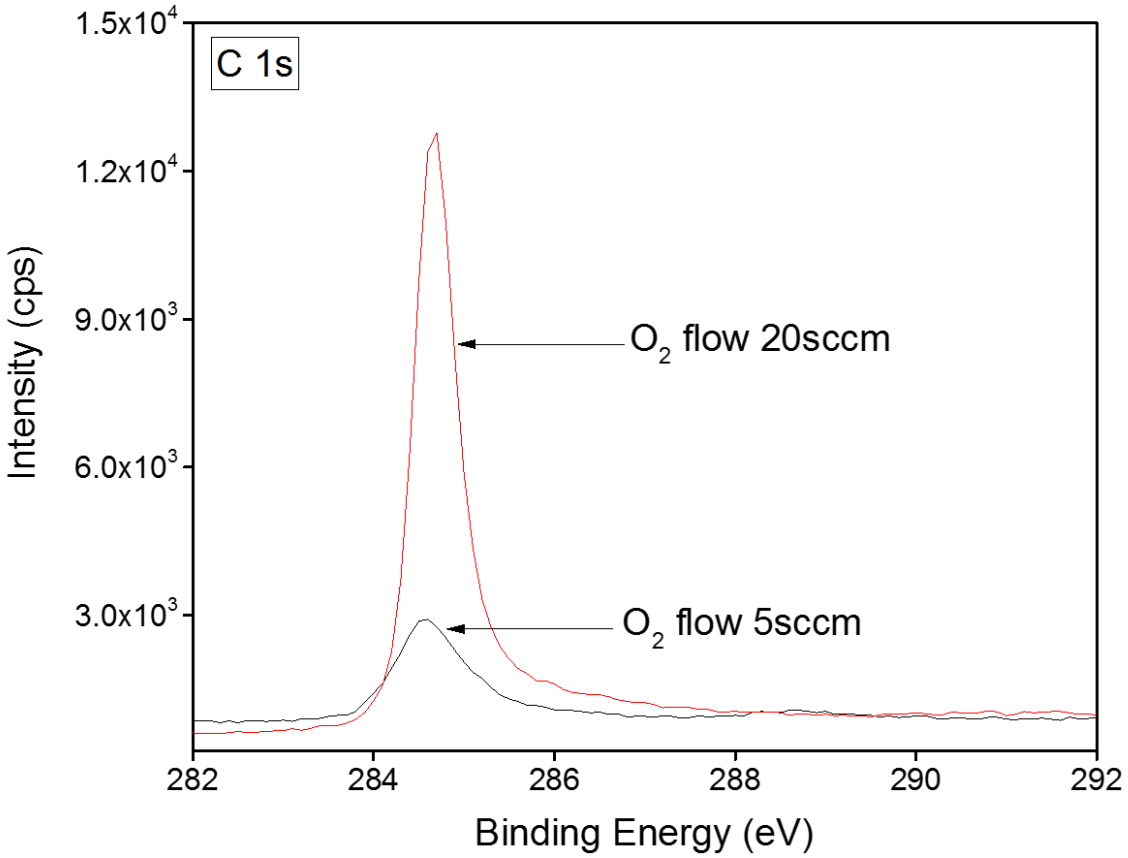

Figure 2.15. XPS spectra of graphene samples grown with recipe III and different O_2 exposures.

2.4. Conclusion

In conclusion, we have systematically investigated the effect of O_2 exposure during the growth in CVD system for high quality graphene synthesis. We suggest that O_2 exposure during the growth plays two important roles on graphene synthesis in CVD. The first effect is the suppression of nucleation density by passivating the Cu surface, and the second effect is the etching of graphene islands. The reduced nucleation density enables more uniform distribution of graphene islands through Cu surface. The etching of graphene islands provides more uniform thickness by yielding single layer graphene island formation

on Cu surface. The synthesis of high quality and uniform graphene islands confirms that the optimization conditions are attained by the O_2 exposure of 5 sccm during the growth.

2.5. References for chapter 2

[1] P.R. Wallace: *The band theory of graphite*. Physical review **71**, no. 9 (1947), 622.

[2] K.S. Novoselov, A.K. Geim, S.V. Morozov, D. Jiang, Y-Zhang, S.V. Dubonos, I.V. Grigorieva, and A.A. Firsov: *Electric field effect in atomically thin carbon films*. Science **306**, no. 5696 (2004), 666-669.

[3] K. Ziegler: *Robust transport properties in graphene*. Physical review letters **97**, no. 26 (2006), 266802.

[4] S.D. Sarma, S. Adam, E. H. Hwang, and E. Rossi: *Electronic transport in two-dimensional graphene*. Reviews of modern physics **83**, no. 2 (2011), 407.

[5] R.S. Shishir and D. K. Ferry: *Intrinsic mobility in graphene*: Journal of Physics: Condensed matter **21**, no. 23 (2009), 232204.

[6] L.Banszerus, M. Schmitz, S. Engels, J. Dauber, M. Oellers, F. Haupt, K. Watanabe, T. Taniguchi, B. Beschoten, and C. Stampfer: *Ultrahigh-mobility graphene devices from chemical vapor deposition on reusable copper*. Science advances **1**, no. 6 (2015), e1500222.

[7] A. Zandiatashbar, G.-H. Lee, S. J. An, S. Lee, N. Mathew, M. Terrones, T. Hayashi, C.R. Picu, J. Hone, and N. Koratkar: *Effect of defects on the intrinsic strength and stiffness of graphene*. Nature communications **5** (2014).

[8] X. Li, L. Colombo, and R.S. Ruoff: *Synthesis of graphene films on copper foils by chemical vapor deposition*. Advanced materials **28**, no. 29 (2016), 6247-6252.

[9] K.V. Emtsev, A. Bostwick, K. Horn, J. Jobst, G.L. Kellogg, L. Ley, J.L. McChesney, T. Ohta, S.A. Reshanov, J. Röhrl, E. Rotenberg, A.K. Schmid, D. Waldmann, H.B. Weber, T. Seyller: *Towards wafer-size graphene layers by atmospheric pressure graphitization of silicon carbide*. Nature materials **8**, no. 3 (2009), 203-207.

[10] D. Li, M.B. Müller, S. Gilje, R.B. Kaner, and G.G. Wallace: *Processable aqueous dispersions of graphene nanosheets*. Nature nanotechnology **3**, no. 2 (2008), 101-105.

[11] C.Y. Su, A.Y. Lu, Y. Xu, F.R. Chen, A.N. Khlobystov, and L.J. Li: *High-quality thin graphene films from fast electrochemical exfoliation*: ACS nano **5**, no. 3 (2011), 2332-2339.

[12] G.H. Han, F. Gunes, J.J. Bae, E.S. Kim, S.J. Chae, H.J. Shin, J.Y. Choi, D. Pribat, and Y.H. Lee: *Influence of copper morphology in forming nucleation seeds for graphene growth*: Nano letters **11**, no. 10 (2011), 4144-4148.

[13] I. Vlassiouk, S. Smirnov, M. Regmi, S.P. Surwade, N. Srivastava, R. Feenstra, G. Eres, C. Parish, N. Lavrik, P. Datskos, S. Dai, and P. Fulvio: *Graphene nucleation density on copper: fundamental role of background pressure*. The journal of physical chemistry C **117**, no. 37 (2013), 18919-18926.

[14] P. Zhao, Y. Cheng, D. Zhao, K. Yin, X. Zhang, M. Song, S. Yin,Y. Song, P. Wang, M.Wang, Y. Xia, and H. Wang: *The role of hydrogen in oxygen-assisted chemical vapor deposition growth of millimeter-sized graphene single crystals*. Nanoscale **8**, no. 14 (2016), 7646-7653.

[15] Y. Hao, M. S. Bharathi, L. Wang, Y. Liu, H. Chen, S. Nie, X. Wang, H Chou,C. Tan, B. Fallahazad, H. Ramanarayan, C.W. Magnuson, E. Tutuc, B. I. Yakobson, K.F. McCarty, Y.W. Zhang, P. Kim, J. Hone, L. Colombo, and R.S. Ruoff: *The role of surface oxygen in the growth of large single-crystal graphene on copper*. Science **342**, no. 6159 (2013), 720-723.

[16] S.M. Kim, A. Hsu, Y.H. Lee, M. Dresselhaus, T. Palacios, K.K. Kim, and J. Kong: *The effect of copper pre-cleaning on graphene synthesis*. Nanotechnology **24**, no. 36 (2013), 365602.

[17] Y. Wang, Y. Zheng, X. Xu, E. Dubuisson, Q. Bao, J. Lu, and K.P. Loh: *Electrochemical delamination of CVD-grown graphene film: toward the recyclable use of copper catalyst*. ACS nano **5**, no. 12 (2011), 9927-9933.

[18] A.C. Ferrari: *Raman spectroscopy of graphene and graphite: disorder, electron–phonon coupling, doping and nonadiabatic effects*. Solid state communications **143**, no. 1 (2007, 47-57.

[19] Y.Y. Wang, Z.H. Ni, T. Yu, Z.X. Shen, H.M. Wang, Y.H. Wu, W. Chen, and A.T.S. Wee*: Raman studies of monolayer graphene: the substrate effect*. The Journal of Physical Chemistry C **112**, no. 29 (2008), 10637-10640.

[20] L.M. Malard, M. A. A. Pimenta, G. Dresselhaus, and M. S. Dresselhaus: *Raman spectroscopy in graphene*: Physics Reports 473, no. 5 (2009), 51-87.

[21] Z. Mutlu, S. Shahrezaei, S. Temiz, M. Ozkan, and C.S. Ozkan: *Facile Synthesis and Characterization of Two Dimensional Layered Tin Disulfide Nanowalls*. Journal of electronic materials **45**, no. 4 (2016), 2115-2120.

[22] K. Kim, S. Coh, L.Z. Tan, W. Regan, J.M. Yuk, E. Chatterjee, M.F. Crommie, M.L. Cohen, S.G. Louie, and A. Zettl*: Raman spectroscopy study of rotated double-layer graphene: misorientation-angle dependence of electronic structure*. Physical review letters **108**, no. 24 (2012), 246103.

[23] Z. Mutlu, R.J. Wu, D. Wickramaratne, S. Shahrezaei, C. Liu, S. Temiz, A. Patalano, M. Ozkan, R.K. Lake, K.A. Mkhoyan, C.S. Ozkan: *Phase Engineering of 2D Tin Sulfides*. *Small* **12**, no. 22 (2016): 2998-3004.

[24] Z. Mutlu, I. Ruiz, R. Wu, R. Ionescu, S. Shahrezaei, S. Temiz, M. Ozkan, A.K. Mkhoyan, and C. S. Ozkan*, Chemical vapor deposition of partially oxidized graphene*. RSC Advances **7**, no. 51 (2017): 32209-32215

[25] I. Childres, L.A. Jauregui, W. Park, H. Cao, and Y.P. Chen: *Raman spectroscopy of graphene and related materials*. New developments in photon and materials research **1** (2013).

[26] Z. Ni, Y. Wang, T. Yu, and Z. Shen: *Raman spectroscopy and imaging of graphene*. Nano research **1**, no. 4 (2008), 273-291.

[27] D. Ferrah, O. Renault, C. Petit-Etienne, H. Okuno, C. Berne, V. Bouchiat, and G. Cunge: *XPS investigations of graphene surface cleaning using H2-and Cl2-based inductively coupled plasma*. Surface and interface analysis **48**, no. 7 (2016), 451-455.

Chapter 3. Interface Investigation in Graphene/hBN Heterostructures

Abstract:

In this chapter, we study surface contamination of CVD grown graphene through its two-dimensional heterostructures with hexagonal Boron Nitride (h-BN). The stacking of graphene and other layered materials in the lateral or vertical geometries can offer extended functionality by exploiting interfacial phenomena, quantum confinement and tunneling, which requires the interface between the layered materials be free of contaminates. The vertical heterostructures of CVD-grown graphene and h-BN single crystals are deeply investigated by analytical scanning transmission electron microscopy (STEM) and electron energy loss spectroscopy (EELS). It is shown that graphene contamination, undetectable using micro-scale characterization tools, is prevalent at the nano-scale, and the interfacial contamination between the layers reduces the interlayer coupling and ultimately undermines the graphene/h-BN heterostructures.

3.1. Introduction

As the foremost and thinnest member of two-dimensional (2D) materials, graphene is one atom thick sheet of carbon (C) atoms, which are densely packed in a honeycomb lattice structure [1, 2]. Carbon atoms connect to each other via hybridized-sp^2 orbitals to form σ-bonds by three electrons in plane, while the remaining fourth electron involves in p_z orbitals to form delocalized-π-bonds perpendicular to the plane. Graphene possess extreme mechanical strength thanks to C-C bonds, and gapless semimetallic behavior due

to p_z orbitals. C atoms are located 1.42 Å apart from each other in plane, while sheets are spaced by the distance of 3.35 Å [3].

Hexagonal boron nitride (h-BN) has emerged as another branch of study of 2D materials [4-6], which was initiated by the discovery of graphene. h-BN is a chemically [7] and thermally [8] stable, wide-direct electronic band gap [9] 2D material. The h-BN has an equivalent crystal structure with graphene [10], except polarized covalent bonds formed between boron and nitrogen atoms unlikely non polar C-C bonds that of graphene. h-BN is a member of two-dimensional layered materials family that has atomically smooth surface, dangling bond free interface, and close lattice structure with graphene.

Graphene is one of the remarkable outcomes of innovative efforts to productize next-generation electronics by materials point of view [11-17]. Graphene possesses superior properties such as high carrier mobility, high thermal conductivity, optical transparency, and tunable electronic band gap [18-20]. The characteristics of this recently discovered two-dimensional carbon (C) allotropes are ideal to be utilized as channel material for high performance device applications, namely transistors, biological and chemical sensors [21-23], etc. The effectiveness of graphene-based nanoscale devices is easily altered by various factors. The numerous studies indicate that the performance of devices built on a channel material of graphene sitting on hexagonal h-BN is quite higher than graphene is on SiO_2/Si substrates [24-27].

The very similar crystal structure and completely different electronic characteristics of h-BN offer ideal platform to tune graphene's electronic properties by building graphene/h-BN heterostructures [28-30]. Building vertical heterostructures of two

dimensional (2D) materials promises great opportunities to devise electronic properties in certain aspects. Graphene / h-BN heterostructures have been emerged as a popular topic to investigate and enhance the properties of utilitarian combination of these two materials as being channel and substrate components in devices [31-34]. Accordingly, it is important to synthesize clean interface of graphene/h-BN for sensitive electronic device applications [35]. Herein, we investigate the interface of graphene/h-BN by surveying interlayer coupling, which gets significantly affected through surface contamination on graphene. The heterostructures of vertically stacked graphene/h-BN are achieved by the procedure of integration of micromechanically produced h-BN crystals onto CVD-grown graphene crystals on Copper (Cu) foils. We perform Raman spectroscopy to characterize the graphene and h-BN crystals, and further to verify the formation of graphene/h-BN heterostructures. We used scanning electron microscopy (SEM) to study the surface morphology of graphene We employ the high resolution scanning transmission electron microscopy (STEM) to visualize the graphene, h-BN, and their heterostructures, and complementary electron energy loss spectroscopy (EELS) to investigate interlayer coupling, and energy dispersive X-ray (EDX) spectroscopy to analyze the contamination of graphene surface.

3.2. Methods:

3.2.1. Materials synthesis:

Electropolishing of Cu foils: It is a very important procedure that the smoothing of Cu foils prior to growth helps to improve the quality of graphene. We cut (wrinkle-freely) Cu foils 2 cm x 1.5 cm x 20 μm in dimensions and set as an anode, then immersed the Cu foil in a solution with the larger and thicker Cu foil set as a cathode in a homemade electrochemistry cell. The electrochemical solution consists of 500 mL deionized (DI) water, 250 mL phosphoric acid (H_3PO_4), 250 mL ethanol (C_2H_6O), 50 mL isopropyl alcohol (IPA: C_3H_80), and 10 g urea (CH_4N_2O). A direct current (DC) power supply was used to apply 0.7 A of current at 2.7 V of potential for 100 sec. After electro-polishing, the Cu foil was rinsed with DI water, further washed with IPA, and then blow- dried with nitrogen.

CVD of Graphene on Cu foils: The graphene samples were grown by CVD method in a single zone split horizontal quartz tube furnace. The furnace was heated up to 1000 °C with the heating ramp of 25 °C min^{-1} under a gas mixture of H_2 (100 sccm) and Ar (400 sccm), and the growth pressure of 15 Torr was maintained during the entire process. The annealing for 20 minutes with O_2 (10 sccm) and H_2 (100) flow is followed by the growth for 25 seconds for island type graphene deposition under a gas mixture of CH_4 (10 sccm), and H_2 (100 sccm). The furnace then cooled down to room temperature with Ar and H_2 flow.

Micromechanical exfoliation of h-BN onto Graphene / Cu foils: The h-BN crystals are prepared by micromechanical exfoliation technique by isolating from the bulk crystal. The h-BN crystals are later transferred onto the graphene / Cu foil from a mediate carrier substrate such as PDMS or scotch tape. It is quite challenging to be able to convey h-BN onto graphene / Cu foil since the foil gets even thinner than the initial thickness of 20 μm due to the high temperature during the CVD graphene synthesis process.

Transfer of Graphene/h-BN from Cu foils to TEM grids: To transfer the as built-heterostructures from a Cu foil to a TEM grid, wet transfer method, which employs the electrochemical delamination, was used. Briefly, The transfer experiment was started with a spin coating of Poly (methyl methacrylate) (PMMA: $(C_5O_2H_8)_n$) on graphene/h-BN/Cu sample as a supporting layer. Next, we let the PMMA to dry 30 minutes under white light or bake it on a hot plate at 180 °C for 90 seconds. Electrolysis process took place in a homemade electrolytic cell by setting the composite of PMMA/graphene/h-BN/Cu as a cathode while thick graphitic rod as an anode, and applying 1.9-2.2 V electrode potential in a solution 1M of sodium hydroxide (NaOH). After separation from Cu, the PMMA/graphene/h-BN were fished out of solution to deionized water bath to cleanse the residual solution. The PMMA/graphene/h-BN were later transferred to quantifoil holey carbon TEM grids. The PMMA layer was successively dissolved in acetone, followed by the IPA rinse and nitrogen blow.

Optical microscopy images in **Figure 3.1** displays the steps of graphene/h-BN fabrication process on TEM grid. The fabrication process is summarized as the CVD

growth of graphene crystals on Cu foil (**a**), micromechanical exfoliation of h-BN crystals on PDMS (**b**), h-BN crystals integrated onto graphene on Cu foil surface to achieve the graphene/h-BN heterostructure (**c**), and as a final step; the graphene/h-BN heterostructure was transferred on TEM grid by using electrochemical delamination process (**d**).

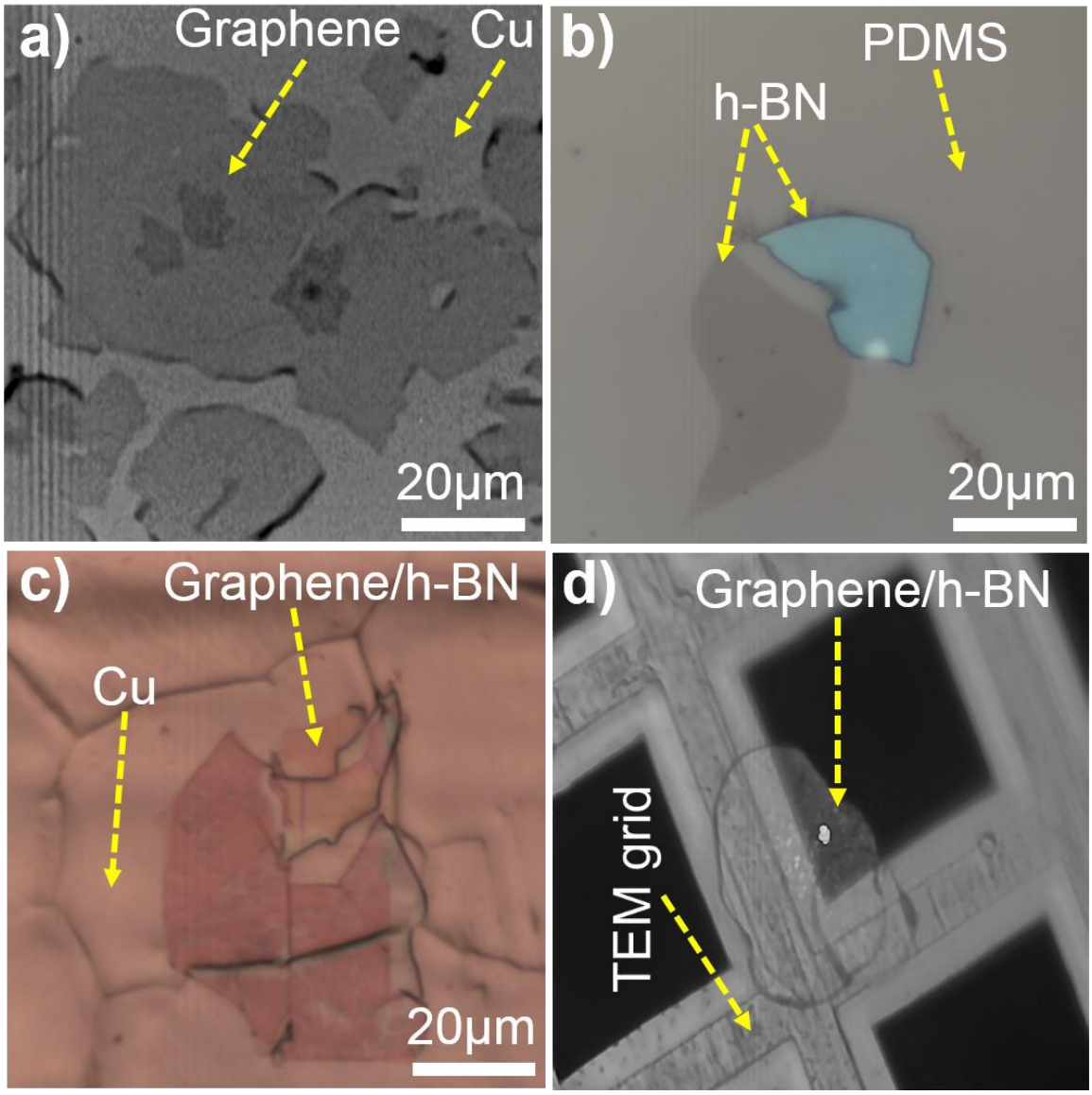

Figure 3.1. Optical microscopy images of step by step graphene/h-BN heterostructure fabrication process. Graphene synthesis (**a**), h-BN synthesis (**b**), the integration of h-BN onto graphene on Cu foil (**c**), the transferred graphene/h-BN from Cu foil to TEM grids (**d**).

3.2.2. Materials characterization:

Microstructural analyses of graphene on Cu substrates were done by the FEI NNS450 scanning electron microscopy (SEM). Raman spectra of graphene on SiO_2/Si substrate were collected using a Horiba system with a 532 nm excitation laser (<1 mW excitation power, 100X objective lens).

FEI Titan G2 60–300 aberration-corrected STEM equipped with a CEOS DCOR probe corrector was used in this study. ADF–STEM images (2048 × 2048 pixel2) were acquired with the STEM operated at 200 keV using a dwell time of 6 μs per image pixel at a camera length of 130 mm. The beam convergence angle, αobj, was measured to be 26 mrad. The ADF detector inner and outer angles of collection were measured to be 54 and 317 mrad, respectively. The measured probe size was ≈0.8 Å.

3.3. Results:

3.3.1. Raman Spectroscopy Characterization

Raman spectroscopy is a non-destructive tool to obtain information about molecular vibrations and crystal structure [36, 37]. Raman spectroscopy is widely used in physical characterization of 2D materials field to probe the surface structure and thickness analysis [38,39]. In Raman spectroscopy, the monochromatic beam of light interacts with the 2D materials through the scattering events by various molecular bonding and phonons in-plane or out of plane, and reveals the spectra with possibly active Raman modes vs. the intensity of corresponding peaks. The Raman spectra of graphene, h-BN, and graphene/h-BN heterostructures provide information about the thickness, crystalline quality, and

substrate effect. We categorize the Raman characterization into three sets, which are the Raman characterization of graphene and h-BN on SiO_2/Si and PDMS, and the Raman characterization of graphene/h-BN heterostructures on SiO_2/Si and TEM grids. We separately characterize the graphene and h-BN crystals to track the thickness and crystallinity information of samples, and compare the substrate effects. We finally conduct the Raman spectroscopy investigation of graphene/h-BN heterostructures to determine the thickness and crystallinity of structures without changing or damaging their properties.

3.3.1.1. Raman Spectroscopy Characterization of Graphene

Raman spectroscopy characterization of graphene is a functional tool that can provide the broad range of information such as; thickness, disorder, doping, strain, thermal conductivity [40, 41]. The Raman spectroscopy of graphene differs in characteristic values depending on the substrate, at which graphene crystals synthesized on it [42]. There are three major Raman modes of graphene crystals. The Raman D band is associated with A_{1g} breathing mode, and it indicates the defects or disorder in graphene crystals. The intensity of Raman D band corresponds to the degree of defects or disorders. The Raman D band is significant for defective graphene samples, and it is negligible in pristine graphene, therefore the Raman D band can be used itself as a parameter to assign the quality of graphene. It is also noteworthy that Raman D band is dispersive and sensitive to the laser properties. The Raman G band is associated with in-plane E_{2g} stretching mode. The Raman frequency of G band is sensitive to the thickness of graphene crystals, as the decreasing thickness causes Raman G band shift to the higher frequencies. Moreover, the position and

intensity of Raman G band can be changed by temperature, doping, and strain, etc. The Raman 2D band is a second order overtone of the D Raman band, and it is dispersive as well. The Raman 2D band is a decisive factor to assign the thickness information of graphene crystals, as the intensity of the peak is higher with decreasing thickness of layers. The sharpness of 2D Raman band is also an indication of high quality graphene samples, as the sharper peaks , narrow full width half maximum (FWHM), implies higher crystalline quality. The intensity ratio of Raman 2D band and G band (I_{2D}/I_G) determines the thickness of graphene, as I_{2D}/I_G>2 indicates single layer graphene. The intensity ratio of Raman D band and G band (I_D/I_G) reveals information about the level of defect or disorder in graphene crystals. Raman spectroscopy characteristics of graphene vary with respect to origin of the type of synthesis and substrate.

Raman Spectroscopy of CVD Grown Graphene:

The CVD-synthesized graphene crystals on Cu foils are transferred onto SiO_2/Si substrates for the detailed Raman spectroscopy characterization. The Raman spectra of the graphene crystals reveal distinguishably varying 2D and G band peak intensity ratios depending on the thickness of samples. The Raman D peak also appears in different intensity values depending on the degree of defects and disorders. The typical Raman spectra of CVD grown graphene with the typical D, G, and 2D peaks is shown in **Figure 3.2**. The ratio of Raman 2D and G peaks (I_{2D} / I_G = 2.63) indicates that the graphene crystal is single layer [43]. The D peak shows some degree of disorder or defect that might originate from CVD process itself or from the transfer process from Cu to SiO_2 [44,45].

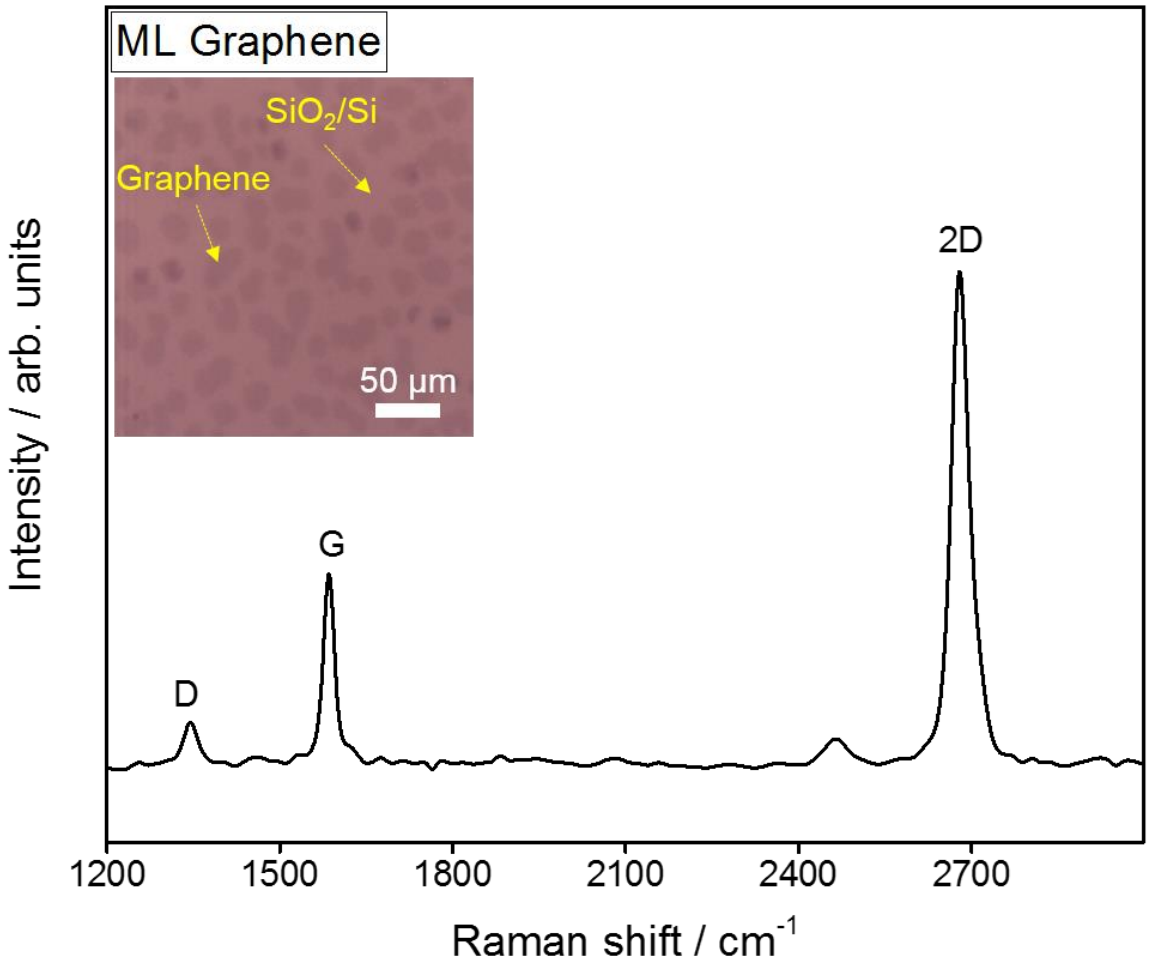

Figure 3.2. The Raman spectra of CVD grown graphene. The inlet presents the optical microscopy image of CVD-grown graphene on SiO_2/Si.

The Raman spectra of graphene crystals with different thickness reveals the varying Raman 2D/G band ratio and shifting Raman G band frequency, **Figure 3.3**. The Raman 2D/G band intensity ratios of graphene crystals are calculated as 2, 0.91, and 0.61 for single layer (SL), few layer (FL), and for multilayer (ML), respectively. The increasing graphene thickness leads the Raman G band shifts to the higher Raman frequencies. We reference

the Raman G band location of SL graphene as reference, and calculated the change of the Raman G band from the reference point with changing thickness.

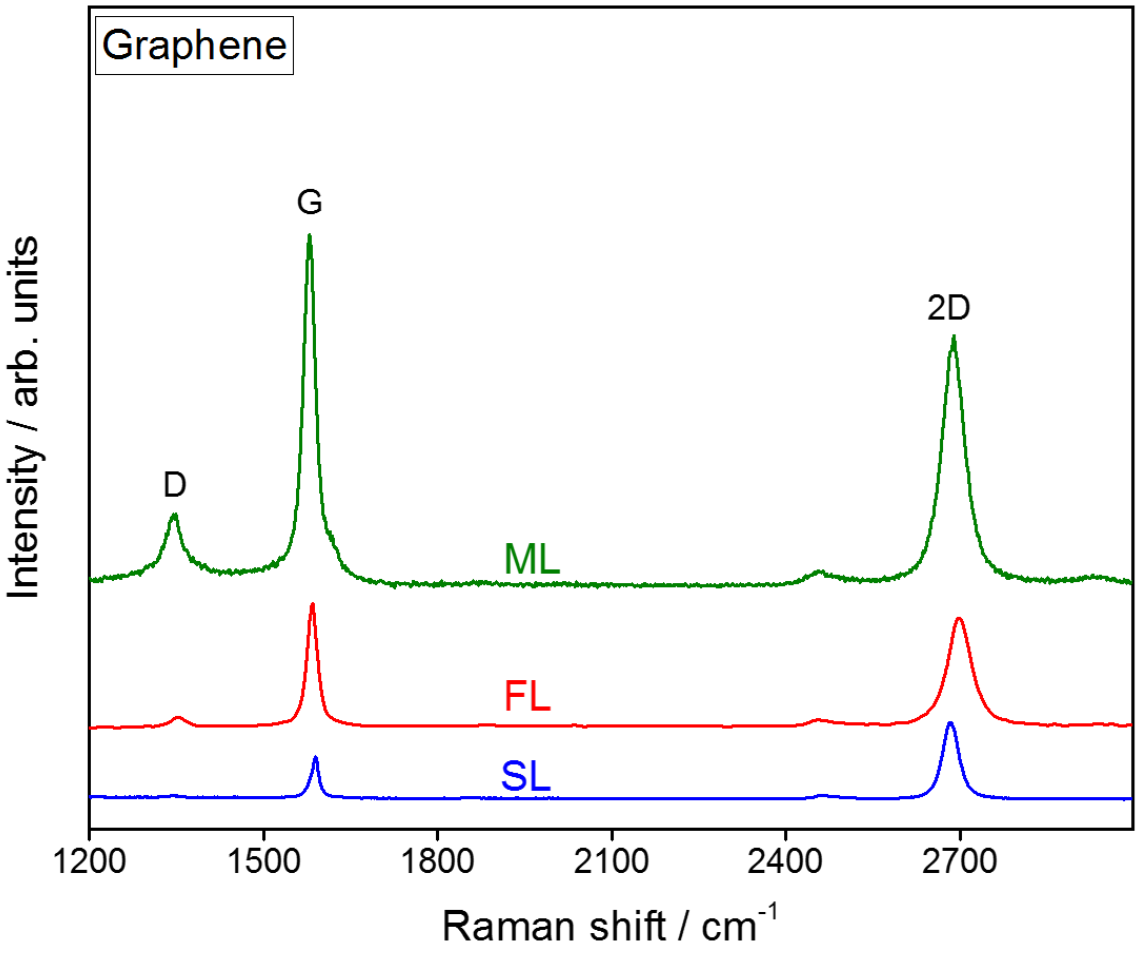

Figure 3.3. The Raman spectra of multi-layer (ML), few-layer (FL), and single-layer (SL) CVD grown graphene crystals.

The Raman frequencies, the shift of G band, the Intensity ratios, the FWHM values of the Raman spectra of CVD-grown SL, FL, and ML graphene are listed on the **table 3.1**. The Raman band intensities were normalized as the intensity of Raman I_G mode was being equal to 1.

Table 3.1. The Raman spectra parameters of CVD grown graphene in different thickness.

Thickness	Single Layer (SL)	Few Layer (FL)	Multi Layer (ML)
W_D (cm^{-1})	1347.1	1351.9	1345.8
W_G (cm^{-1})	1588.3	1583.7	1579.1
W_{2D} (cm^{-1})	2683.8	2698.9	2688.3
ΔW_G (cm^{-1})	0	4.6	9.2
I_D^*	0.08	0.16	0.24
I_G^*	1	1	1
I_{2D}^*	2.00	0.91	0.61
2D-FWHM (cm^{-1})	36	55	52
G-FWHM (cm^{-1})	18	24	29
D-FWHM (cm^{-1})	19	30	57

* The Raman peak intensities are normalized as I_G values equal to 1.

ΔW_G values are calculated as the wavenumber of Raman G peak's deviation from the Raman G peak value that of single layer.

The **Figures 3.4, 3.5, 3.6** show the thickness dependent trends of Raman spectra components that are listed on the **Table 3.1**. Raman 2D/G band ratios increase with the reducing the number of layers. The Raman G band shifts to the higher Raman frequencies with the reducing the number of layers. The value of Raman 2D band FWHM increases with the increasing number of layers.

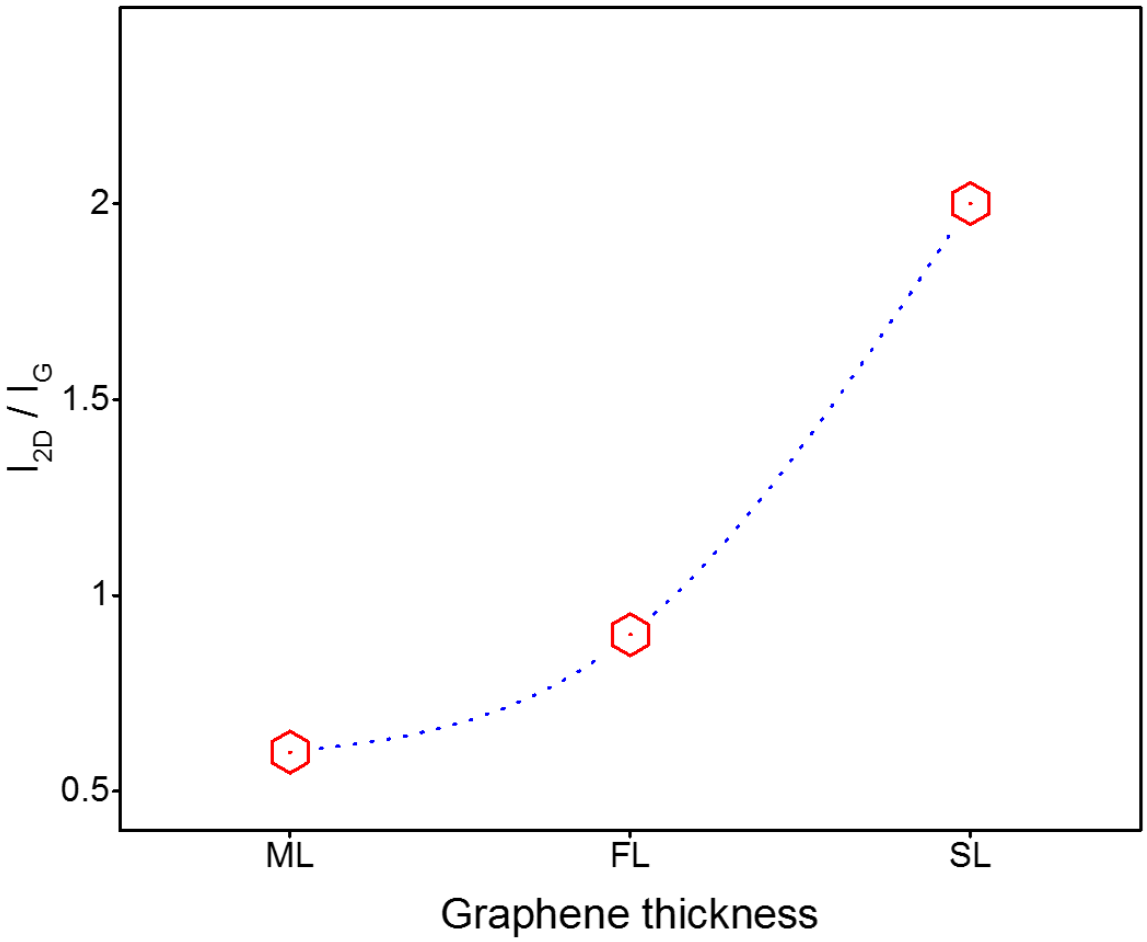

Figure 3.4. The Raman 2D and G band intensity ratios with changing graphene thickness.

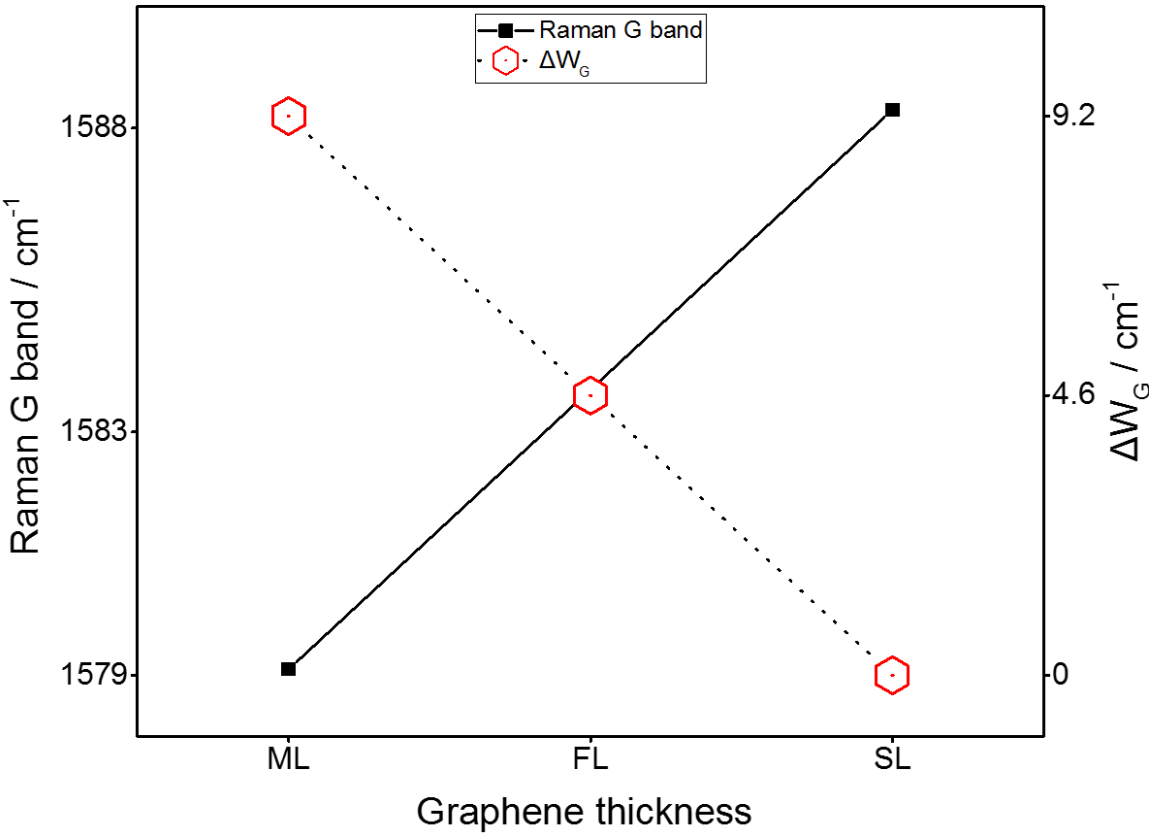

Figure 3.5. The Raman frequency and shift of D band with different graphene thickness as multi-layer (ML), few-layer (FL), and single layer (SL).

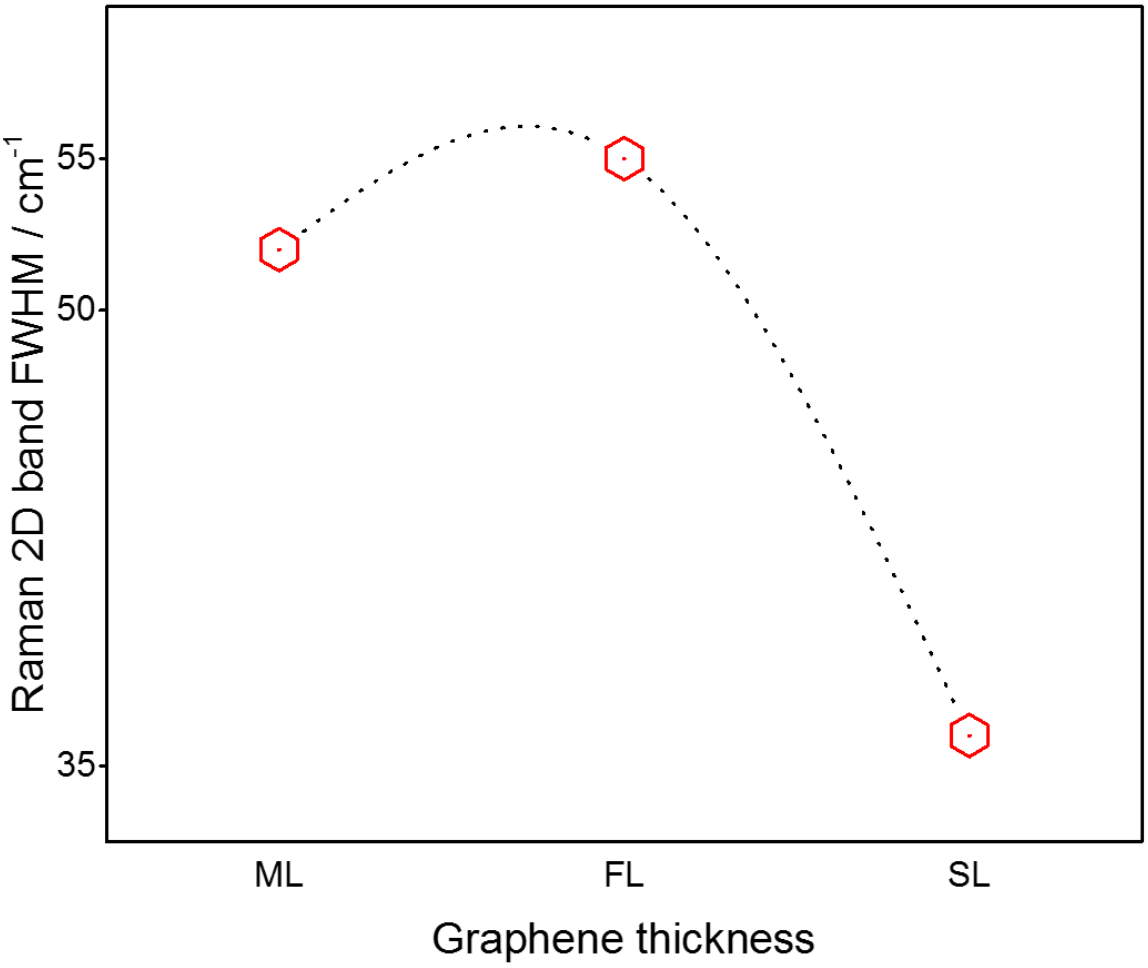

Figure 3.6. The FWHM of Raman 2D band with different graphene thickness as multi-layer (ML), few-layer (FL), and single-layer (SL).

Raman Spectroscopy of Micromechanically Exfoliated Graphene on PDMS:

Micromechanical exfoliation is a common technique for preparing high quality graphene samples in easy to handle and reliable operational process. The individual layers of graphene is isolated from highly ordered pyrolytic graphite (HOPG) by using adhesive surface of scotch tape while thinning and transferring the layers from the source material to final substrate. The graphene crystal exfoliated onto the PDMS substrate reveal major

Raman peaks along with the Raman peaks of PDMS, in **Figure 3.7**. The FWHM of 2D band is calculated as 22 cm^{-1}, this indicates very high quality of graphene. Furthermore, the intensity ratio of the Raman 2D and G band (I_{2D}/I_G) is calculated as 5.26, and this very high intensity ratio indicates single layer (SL), high quality graphene on PDMS substrates. The Raman spectra of exfoliated graphene on PDMS reveals that the very sharp Raman 2D peak, very high intensity ratio of Raman 2D/G modes, and lack of Raman D mode. These interesting results implies that the Raman features, which are linked to crystalline quality, are significantly enhanced by the choice of the type of synthesis method and substrate.

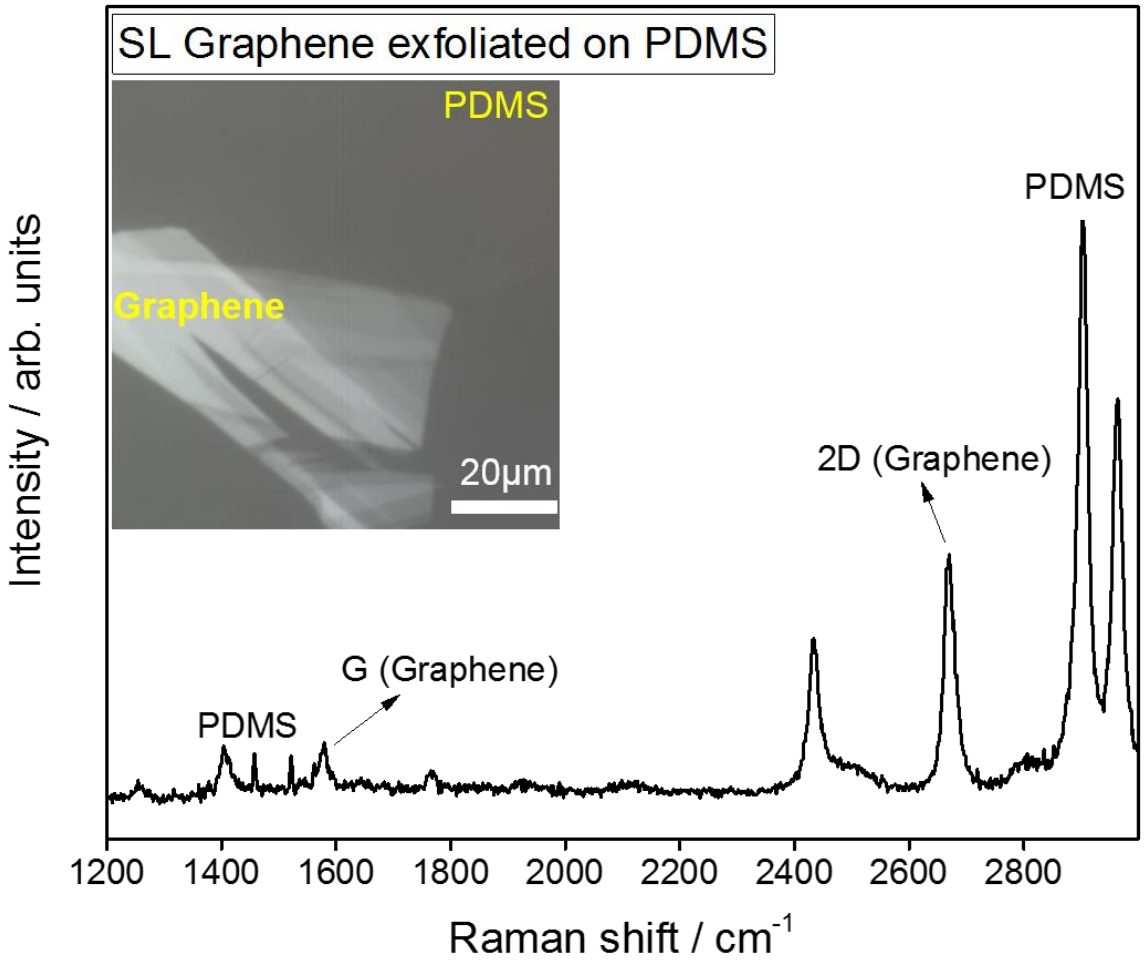

Figure 3.7. The Raman spectra of micro-mechanically exfoliated graphene on PDMS substrate. The inlet presents the optical microscopy image of micromechanically exfoliated graphene on PDMS.

3.3.1.2. Raman Spectroscopy Characterization of h-BN

Raman spectroscopy is a practical technique to verify the h-BN single crystals and designates its characteristics such as thickness, etc. [46]. The h-BN crystals reveal a major E_{2g} peak between 1360 and 1375 cm^{-1} that its intensity and Raman wavenumber position depend on the thickness of the crystals, as in usually observed blue shift with the decreasing thickness [47]. The in-plane Raman E_{2g} mode is analogous to graphene Raman D band,

however it is not dispersive in contrary to graphene Raman D band. Due to large band gap of h-BN, the Raman scattering is not resonant with the laser source in the visible spectrum. Hence, the Raman interlayer shear modes of h-BN are much weaker in intensity than that of the other 2D materials and graphene.

Figure 3.8 shows typical Raman spectra of the h-BN crystal micromechanically exfoliated on PDMS substrate. The vibrational mode of E_{2g} is located at the Raman wavenumber of 1362 cm^{-1} with the corresponding FWHM of 10.1 cm^{-1}. **Figure 3.9** shows typical Raman spectra of the h-BN crystal micromechanically exfoliated on SiO_2/Si substrate. The vibrational mode of E_{2g} is located at the Raman wavenumber of 1372 $cm^{-1}$with the corresponding FWHM of 10.4 cm^{-1}. The h-BN crystals exfoliated on different substrates does not show any dramatic change on their Raman spectra.

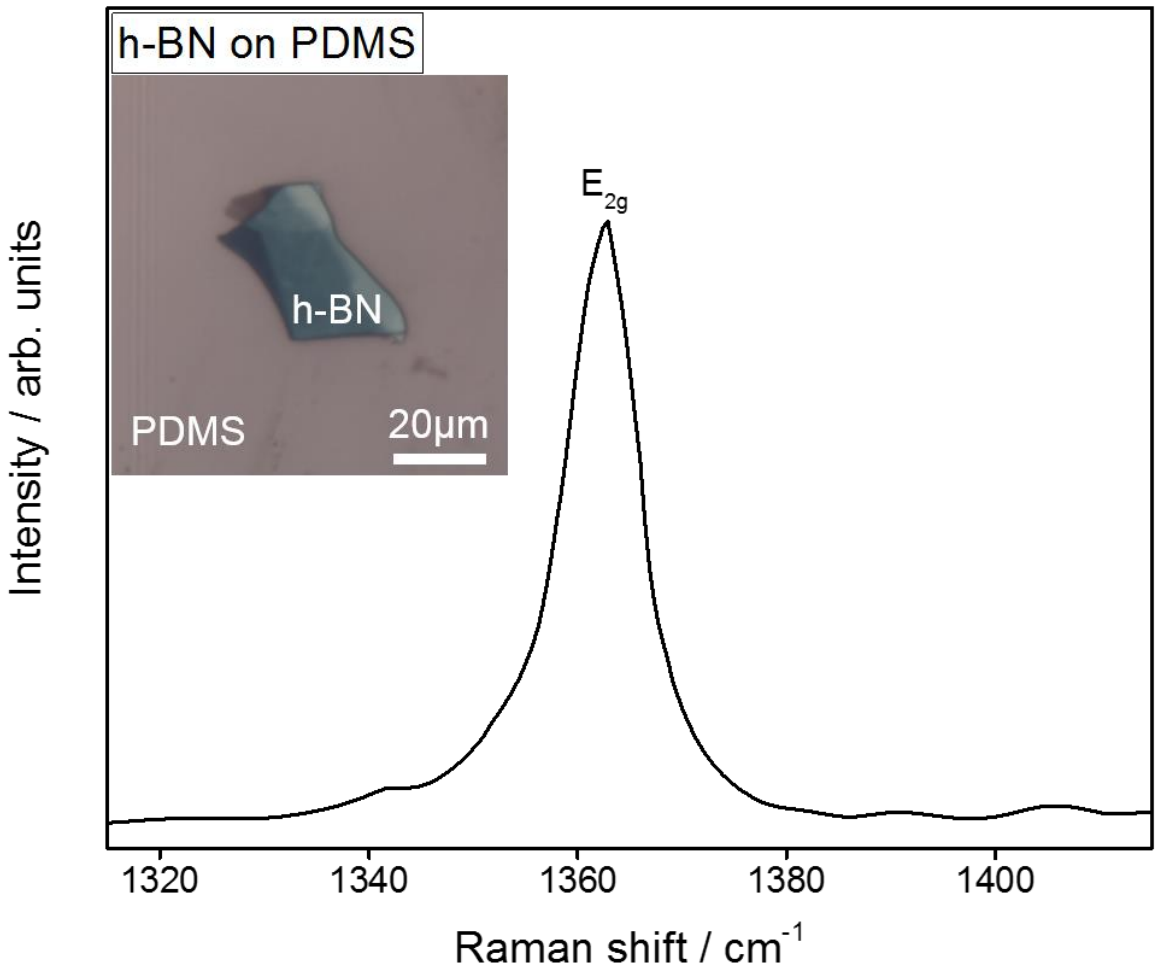

Figure 3.8. Raman spectra of h-BN on PDMS. The inlet presents the optical microscopy image of micromechanically exfoliated h-BN on PDMS.

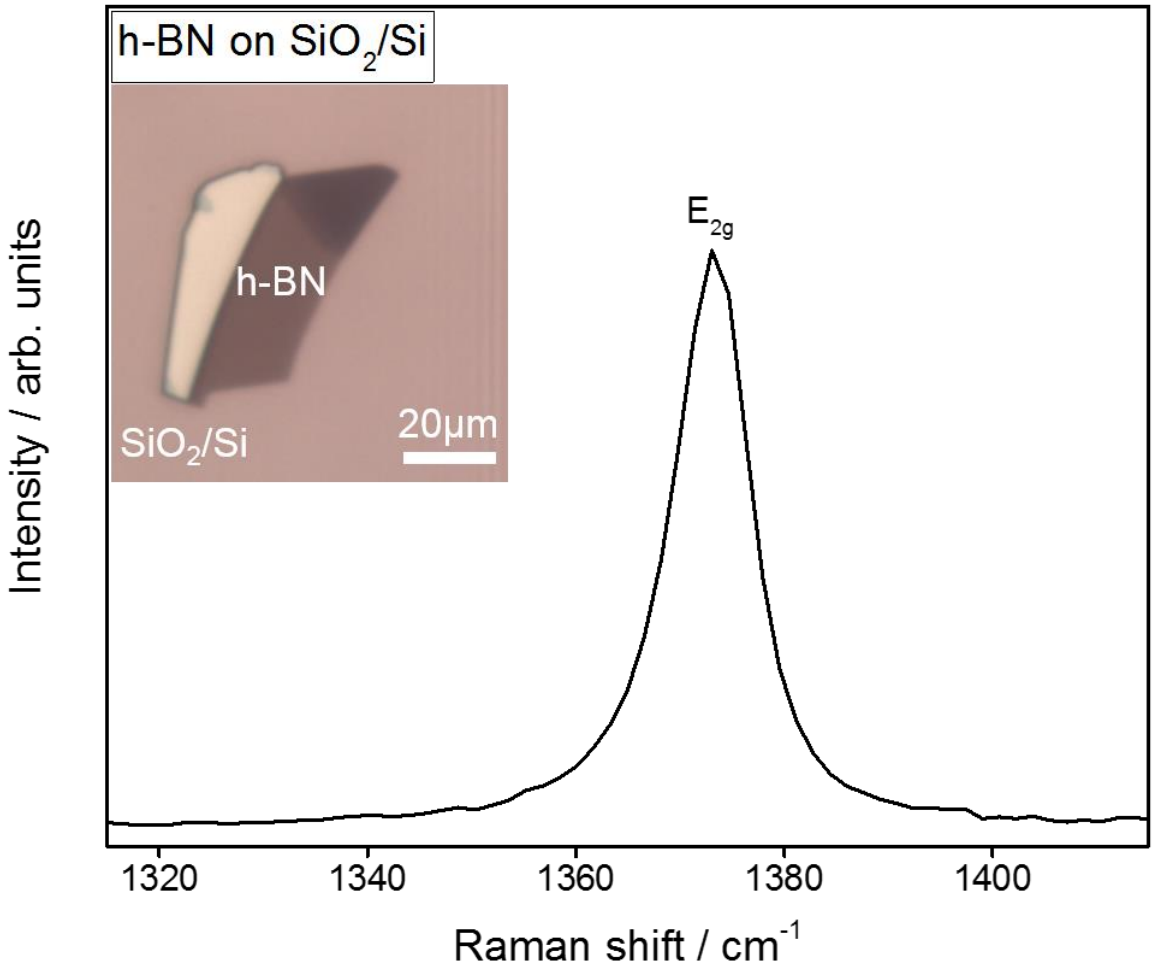

Figure 3.9. Raman spectra of h-BN on SiO_2/Si. The inlet presents the optical microscopy image of micromechanically exfoliated h-BN on SiO_2/Si.

3.3.1.3. Raman Spectroscopy Characterization of Graphene / h-BN

Graphene/h-BN heterostructures can be built on different substrates in according to the purpose of application. We build heterostructures on SiO_2/Si for Raman spectroscopy characterization, and on TEM grids for the high resolution electron microscopy analysis. **Figure 3.10** displays the optical microscopy images of graphene / h-BN heterostructures on SiO_2/Si (**a**) and on TEM grid (**b**). Raman spectroscopy analysis have been done on the

graphene/h-BN heterostructures that are built on SiO_2/Si and TEM grid substrates. The Raman spectra (**Figure 3.11**), which is taken from the junction, with the characteristic h-BN Raman peak of E_{2g} at 1363 cm^{-1} with the FWHM of 9.7 cm^{-1}, and graphene Raman peaks of G band is located at 1579 cm^{-1} with FWHM of 15.8 cm^{-1}, 2D peak is located at 2699 cm^{-} with FWHM of 69 cm^{-1}verifies that the graphene / h-BN heterostructures are successfully built on SiO_2/Si. The Raman spectra does not reveal graphene Raman D band, which is believe to be suppressed by the strong Raman E_{2g} peak of the h-BN. The Raman spectra implies that h-BN is multilayer, and graphene consists of multi layers of graphene sheets. The large FWHM of Raman 2D band also indicates the low quality of graphene or misalignment structure at interface [48, 49].

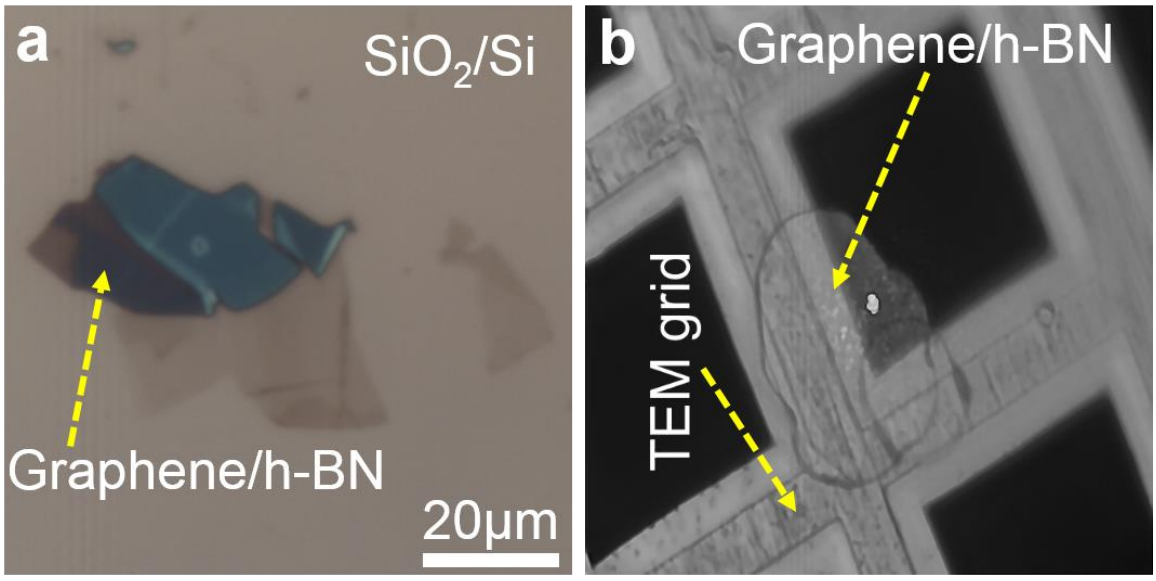

Figure 3.10. The optical microscopy images of the micromechanically exfoliated graphene/h-BN heterostructures on SiO2/Si (**a**), and graphene/h-BN heterostructures consist of CVD grown graphene and micromechanically exfoliated h-BN on TEM grid (**b**).

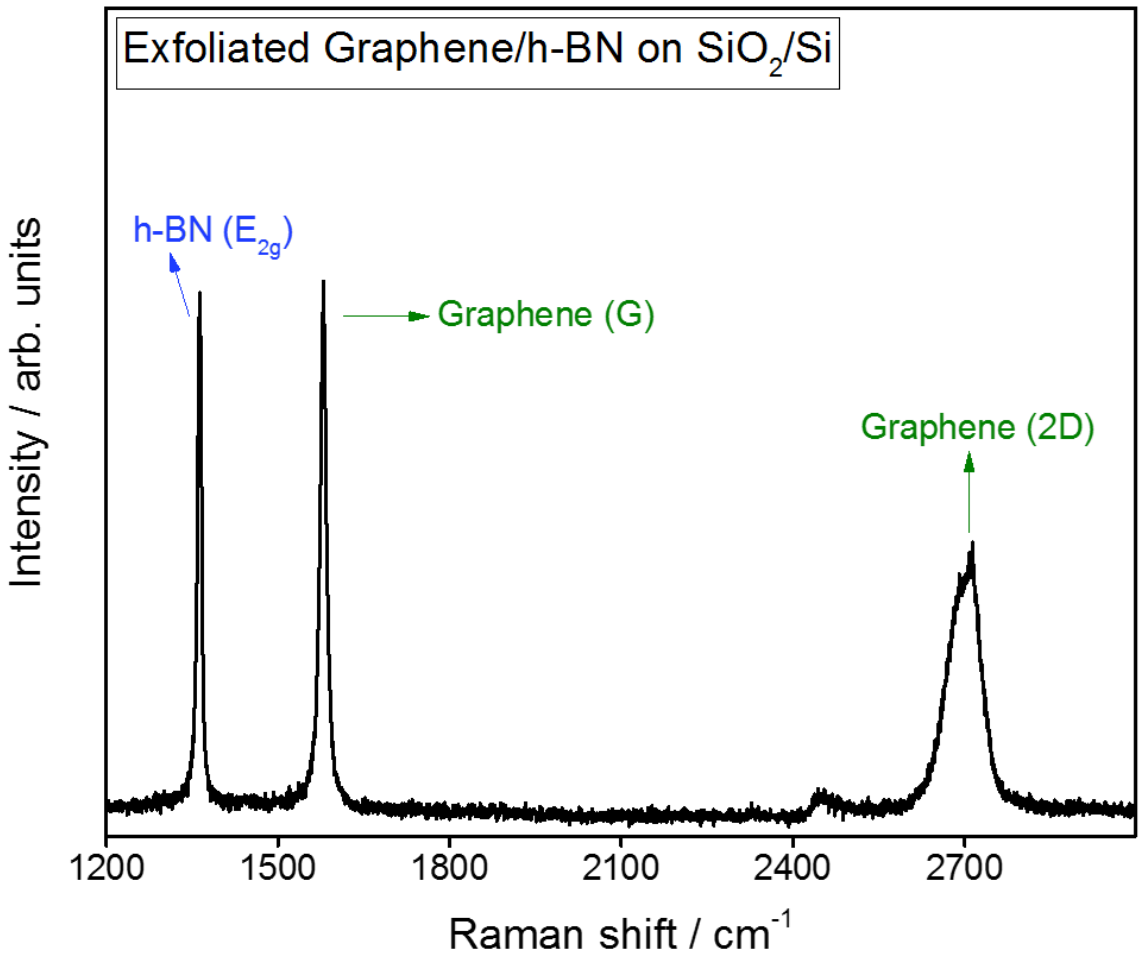

Figure 3.11. Raman spectra of graphene/h-BN on SiO_2/Si.

Figure 3.12 shows the Raman spectra that were taken from the junction of graphene/h-BN heterostructure on a TEM grid for the free-standing structure as the longer scan (a) and the shorter scan from same spot (b). The longer scan Raman spectra of the heterostructure on TEM grid reveals with typical graphene Raman peaks of G peak 1578 cm^{-1} with FWHM of 19.5 cm^{-1}, 2D peak is 2683 cm^{-1} with FWHM of 35.9 cm^{-1}, and Raman h-BN characteristic of E_{2g} peak 1362 cm^{-1} with FWHM of 10.2 cm^{-1}. The Raman 2D and

G band intensity ratio, location of Raman G band and FWHM of Raman 2D band indicate that graphene is single layer. The Raman spectra indicates h-BN crystal consist of few layers of sheets. The shorter scan Raman spectra may reveal splitting the Raman D peak of graphene and Raman E_{2g} peak of h-BN.

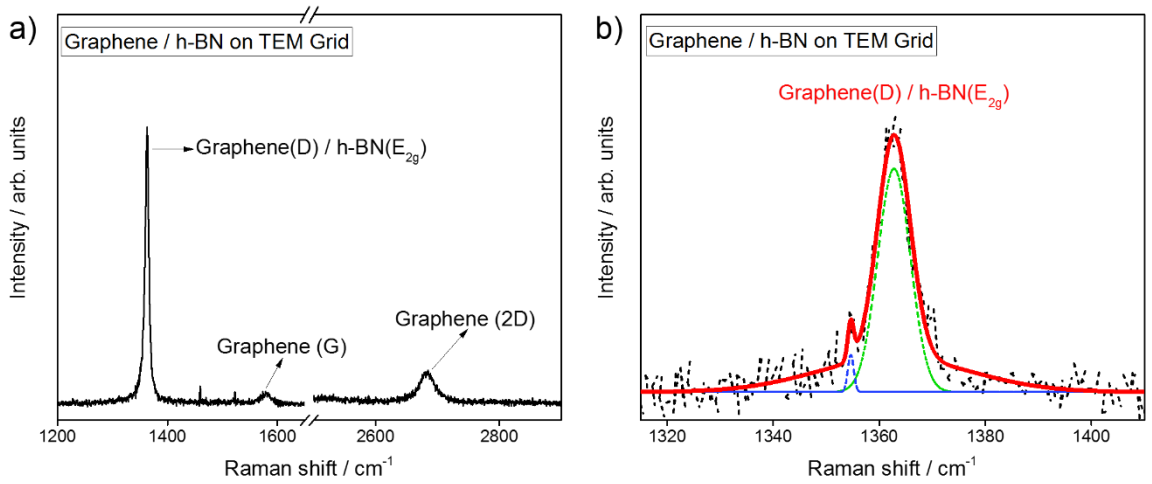

Figure 3.12. The Raman spectra of graphene/h-BN heterostructure on TEM grid as the long spectra (**a**), and zoom in spectra (**b**).

3.3.2. Surface Morphology Characterization of Graphene

Scanning electron microscopy (SEM) is a useful technique that allows one to obtain structural information on the surface of the solid state samples by analyzing the contrast through the primarily backscattered electrons, and compositional information by examining the emitted secondary electrons. The surface morphology of graphene crystals grown by chemical vapor deposition (CVD) on copper (Cu) foils is investigated by the SEM microscopy [50, 51].

Surface contamination is a major challenge in CVD synthesis of graphene on Cu foils. CVD synthesis of graphene on Cu foils presents an interesting detail that the self-limited crystal growth happens on both surfaces of Cu foils. SEM images (**Figure 3.13** and **Figure 3.14**) clearly reveal that surface of graphene grown on the top side of Cu foil has more contamination and surface non-uniformity than that of graphene grown on the bottom side of Cu foil, thus the choice of the graphene from the bottom Cu surface results in better product quality.

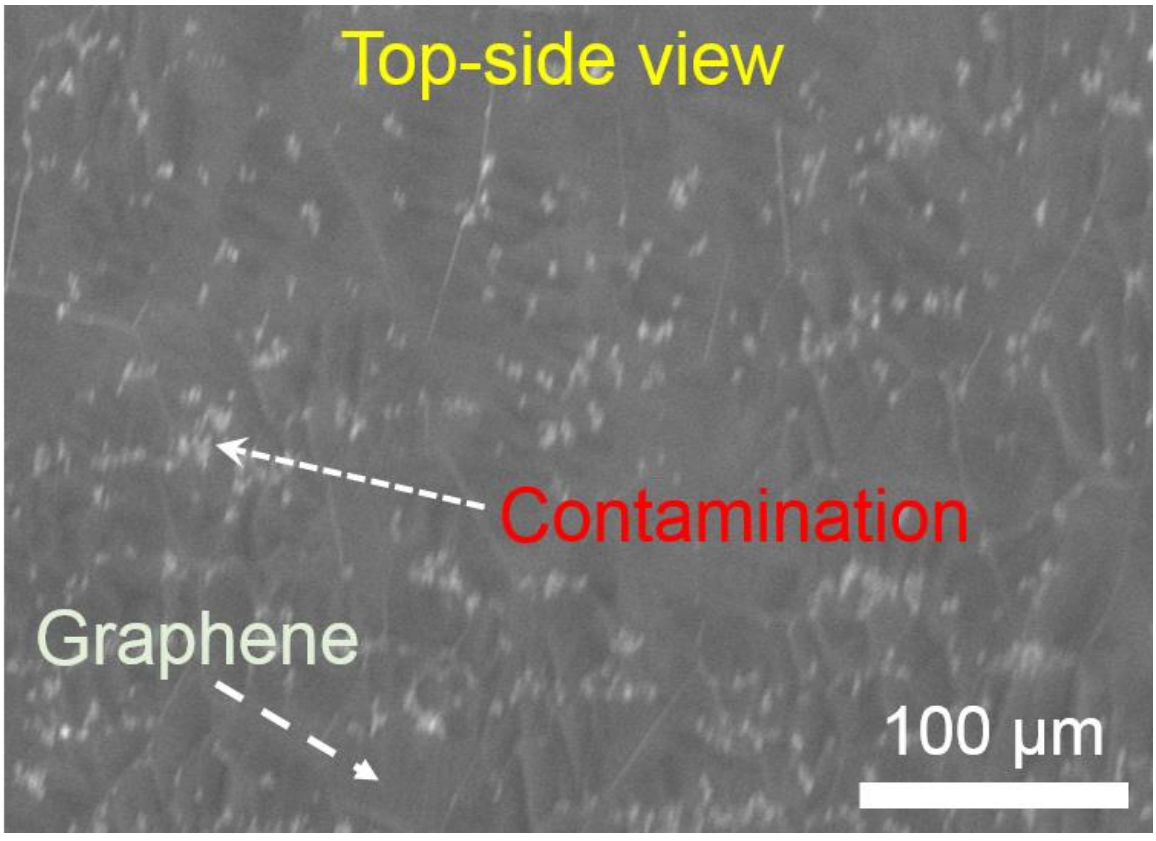

Figure 3.13. SEM Image of graphene crystals grown on the top surface of Cu foil.

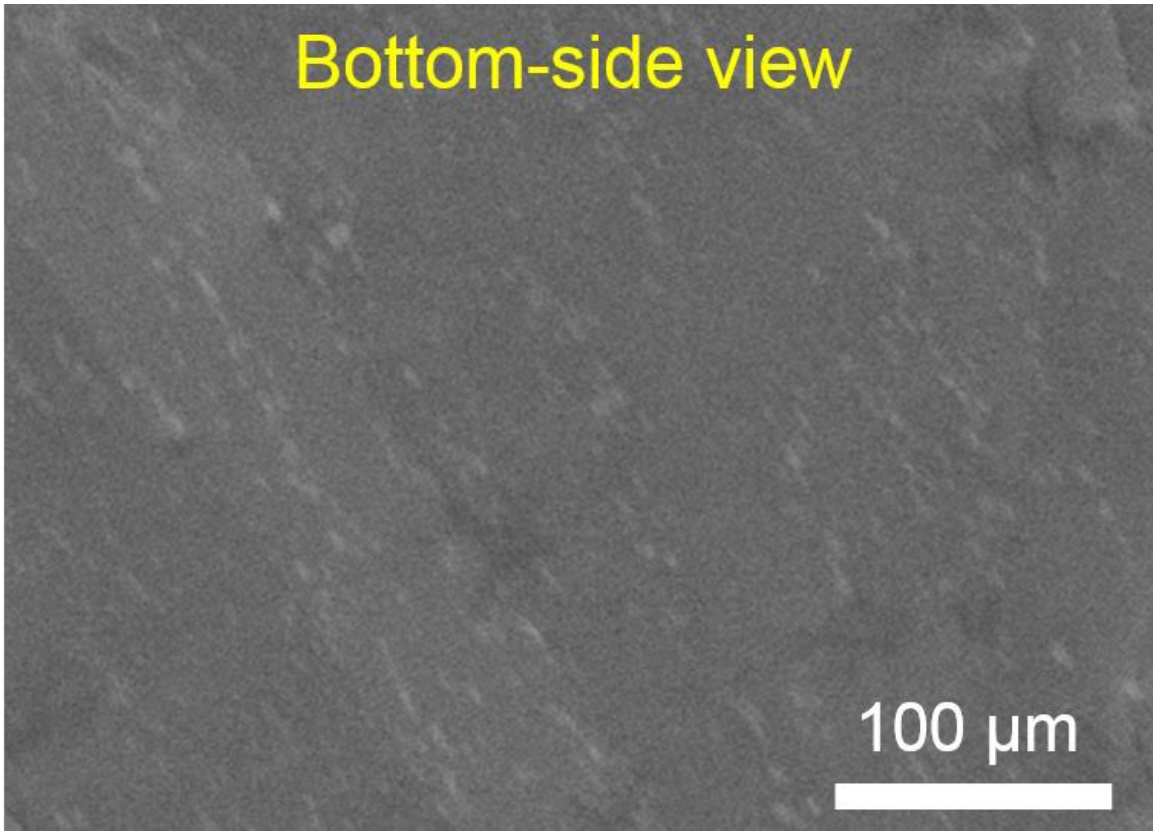

Figure 3.14. SEM Image of graphene crystals grown on the bottom surface of Cu foil.

3.3.3. Scanning Transmission Electron Microscopy Characterization and Complementary Electron Energy Loss Spectroscopy Analysis on Graphene/h-BN Heterostructures

The transmission electron microscopy (TEM) is an advanced imaging technique based on the interaction between the high energy electron beam and sufficiently thin specimen through the diffraction phenomena of the transmitted electron beam. Scanning transmission electron microscopy (STEM) employs a finely focused electron beam scanning over the sample for higher resolution imaging [52, 53]. The high resolution STEM

image of graphene region is shown in **Figure 3.15.** The high resolution STEM image of graphene does not show any sign of contamination. The corrresponding the Fast Fourier transform (FFT) image of Figure 3.22 is displayed in **Figure 3.16.** The FFT image exhibits 12 spots, and the evaluation of this structure indicates that two hexagonal structures are stacked together by 30° angular offset. Hence, the STEM and corresponding FFT images confirmed that we are dealing with double layer graphene crystal.

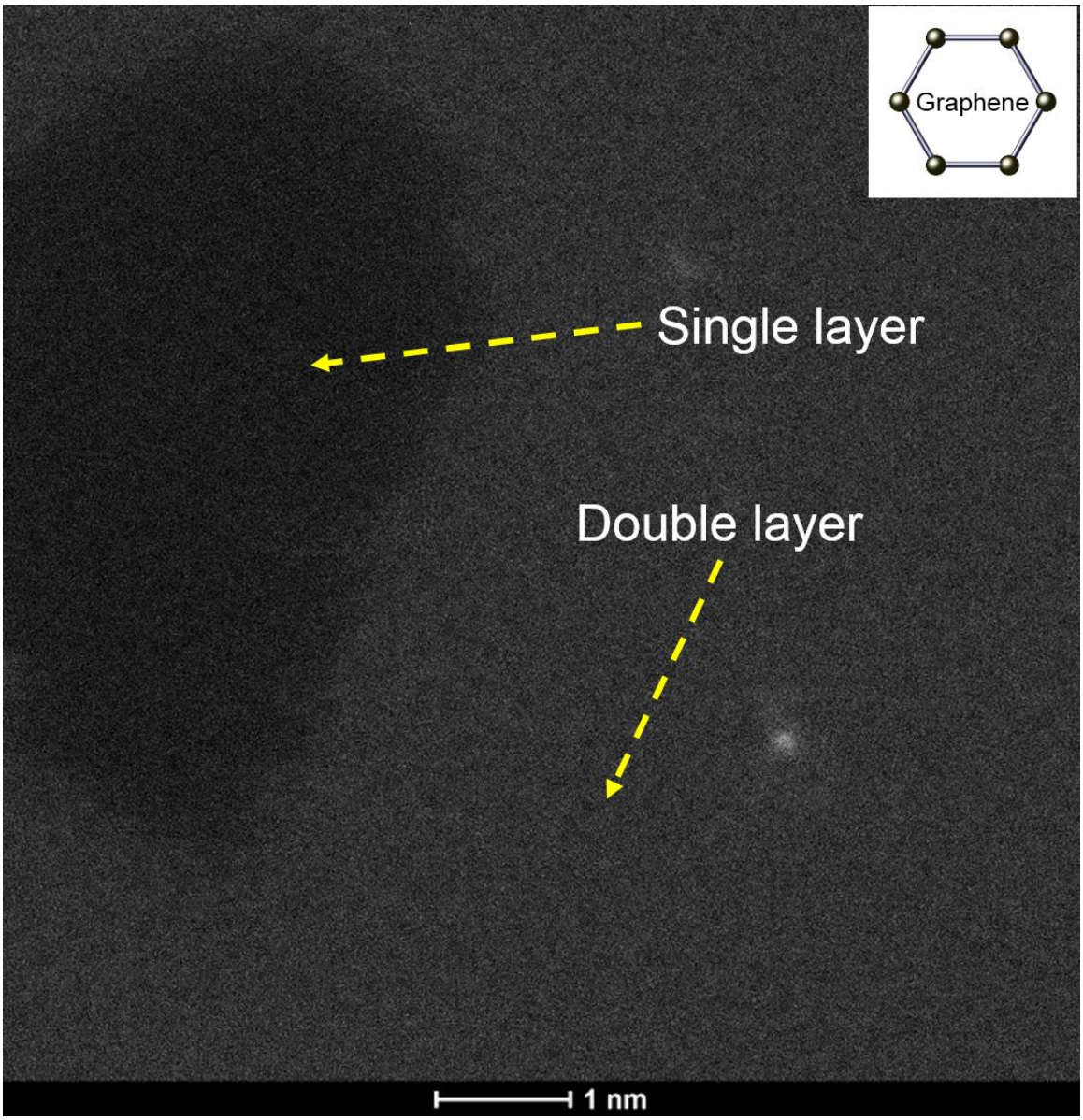

Figure 3.15. The high resolution real space STEM image of graphene, the inset illustrates the crystal structure graphene.

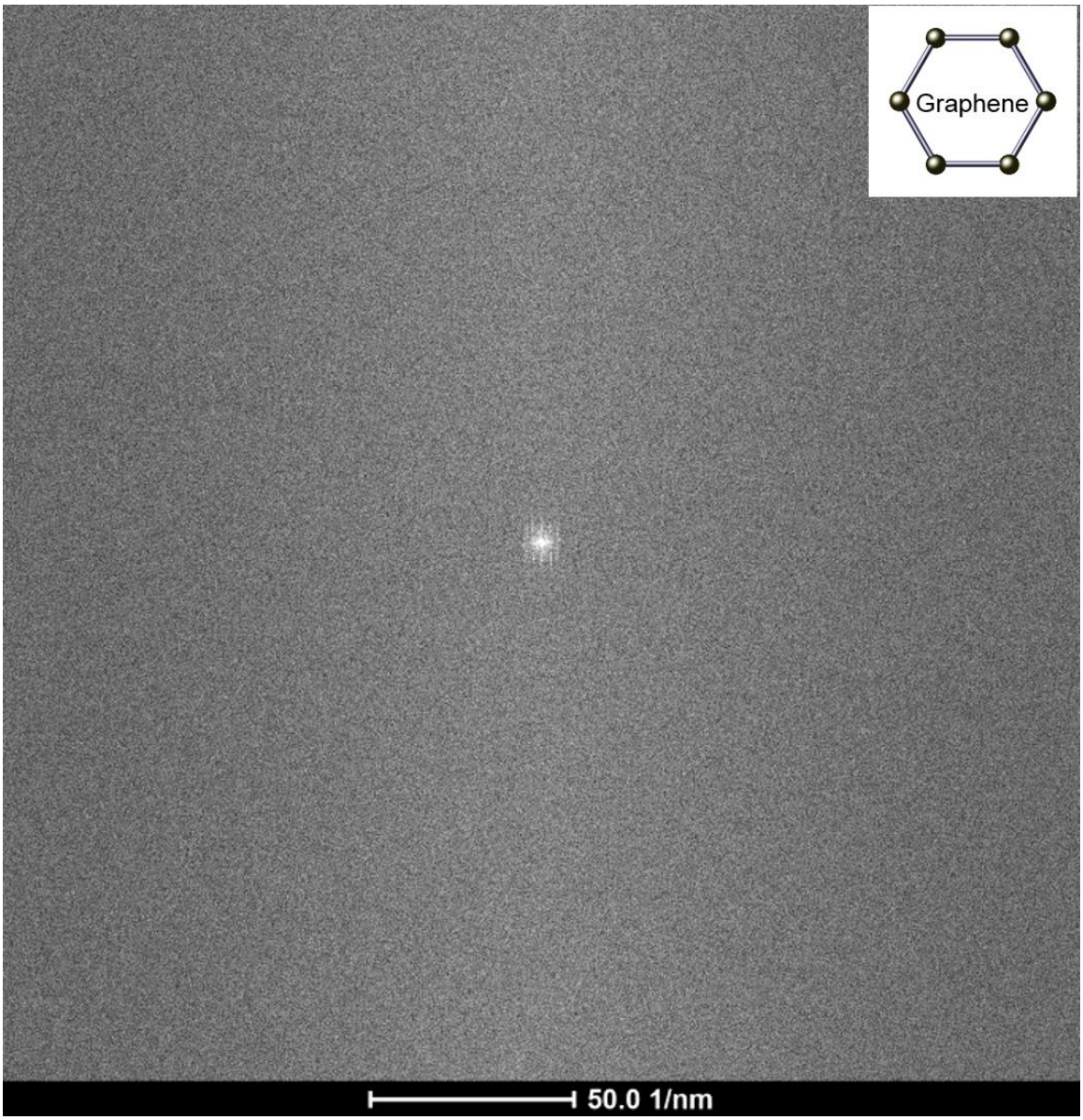

Figure 3.16. The resulting fast Fourier transform image of high resolution real space STEM image of graphene. (The inset illustrates the crystal structure of graphene).

The low magnification STEM image of graphene does not show any sigh of contamination in **Figure 3.17.** Even though high and low magnification STEM images do not prove any contamination agent in graphene structure, we were able to observe

significant contamination in the intermediate magnification of STEM images in **Figure 3.18**. The darker regions on the background represent graphene, while the bright regions may exhibit polymer from transfer process and other contaminants arisen from CVD furnace during graphene synthesis in the intermediate magnification STEM image.

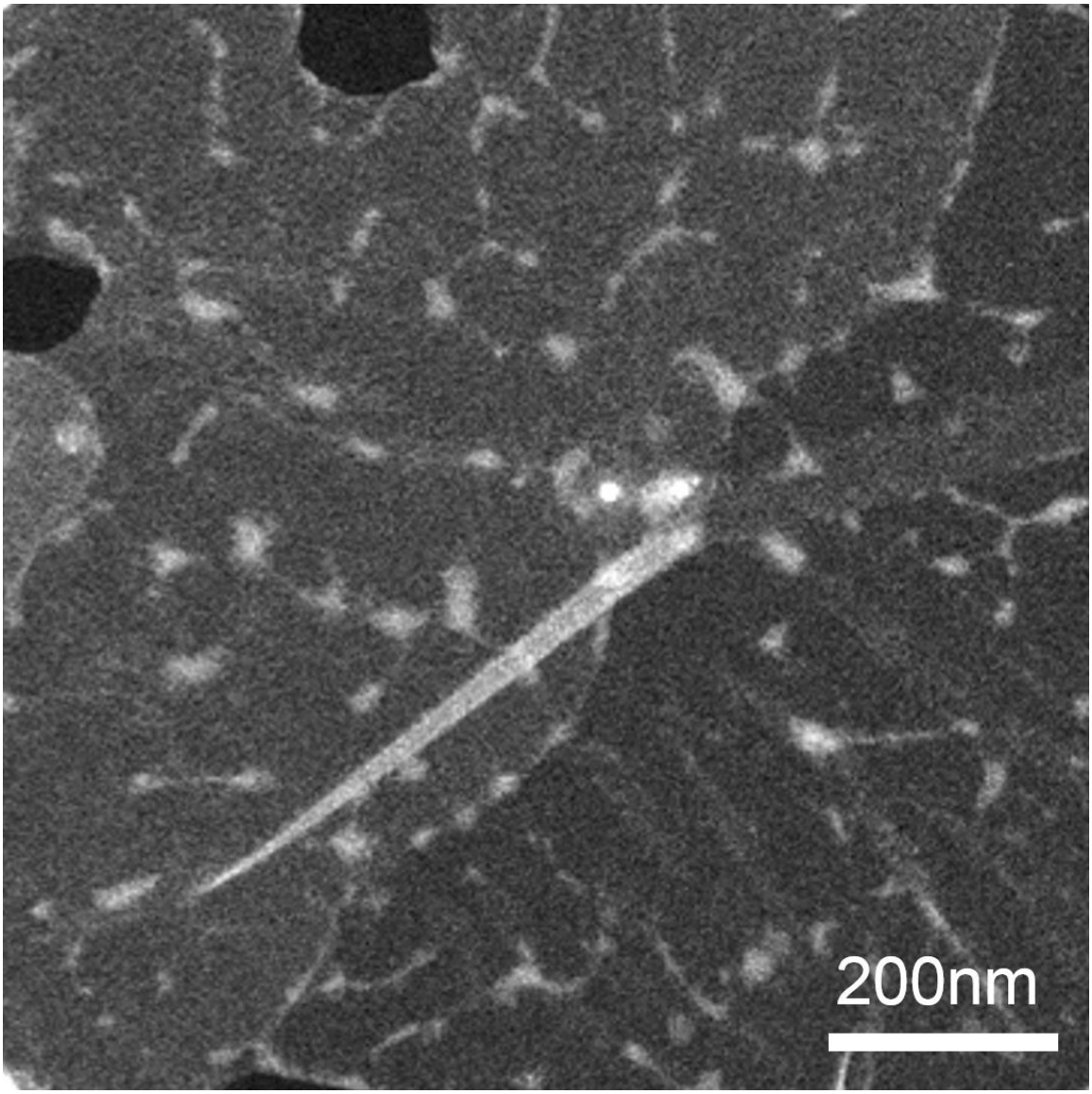

Figure 3.17. The low magnification STEM image of graphene.

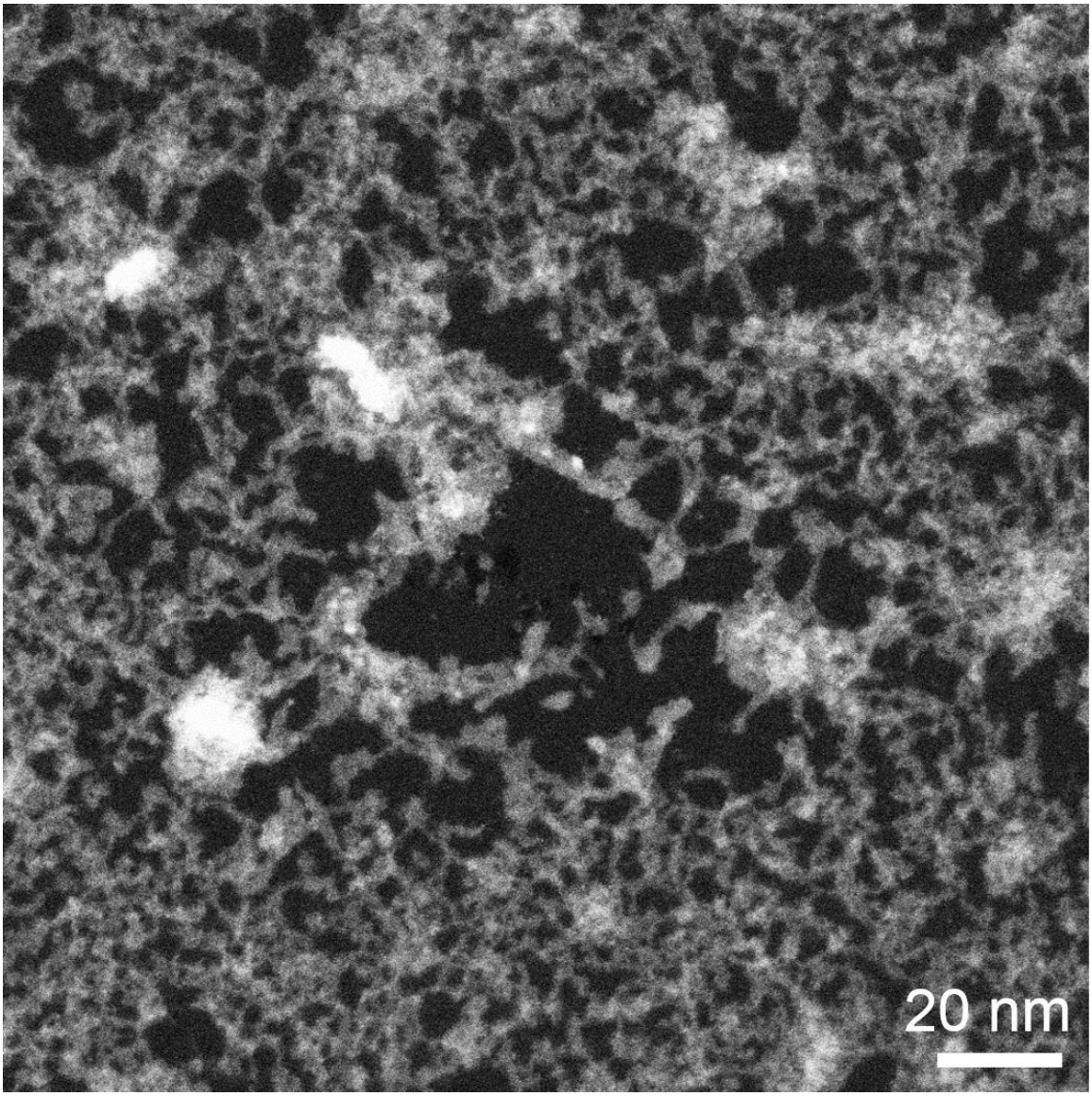

Figure 3.18. The Intermediate magnification STEM image of graphene.

The hexagonal structure of only h-BN region is shown in high resolution STEM images in **Figure 3.19.** The contrast represents different thickness of h-BN crystals, which is the result of lack of uniformity of the synthesis method of micromechanical exfoliation of atomically thin layer materials.

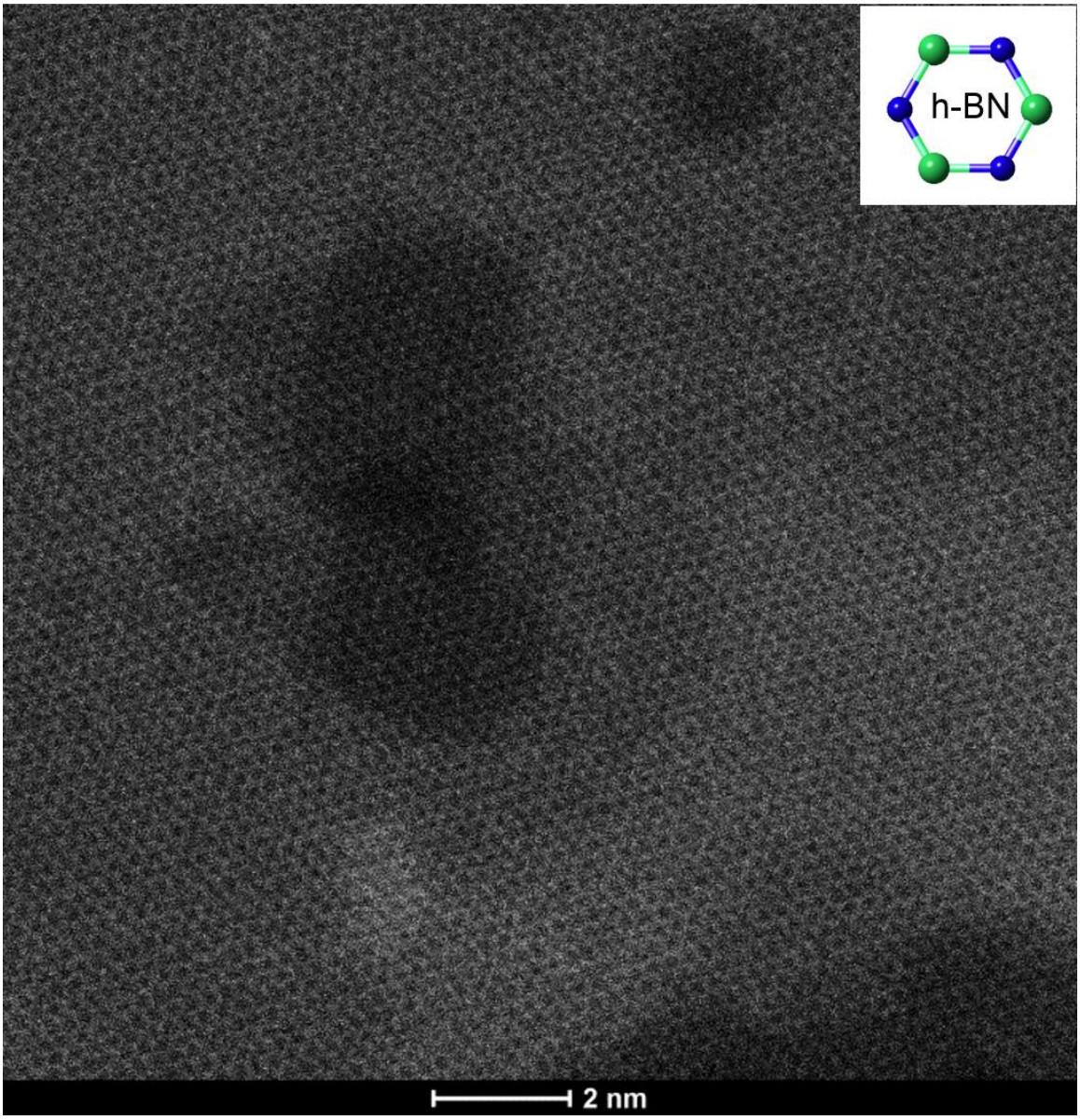

Figure 3.19. The high resolution STEM image of h-BN, the inset illustrates the crystal structure of h-BN.

The high resolution STEM images of h-BN region display few layers thick regions of crystal structure and almost no sign of contamination (**Figure 3.20**). The small scale

periodic structure shows closely-packed atoms in a hexagonal arrangement indicates high crystallinity [54]. The larger scale contrast comes from the intenstity variations of the signals, and indicates the different thickness of h-BN crystals. The high resolution STEM images demonstrates that the hexagonal structure of graphene is similar to that of h-BN.

Figure 3.21 presents the low magnification STEM image of graphene/h-BN heterostructures as the junction and constituent elements. The different regions of graphene/h-BN components are moderately distinguishable in the STEM image. Some degree of polymer residue can also be seen as the contaminant comes from the transfer process of graphene / h-BN from Cu foils to TEM grids.

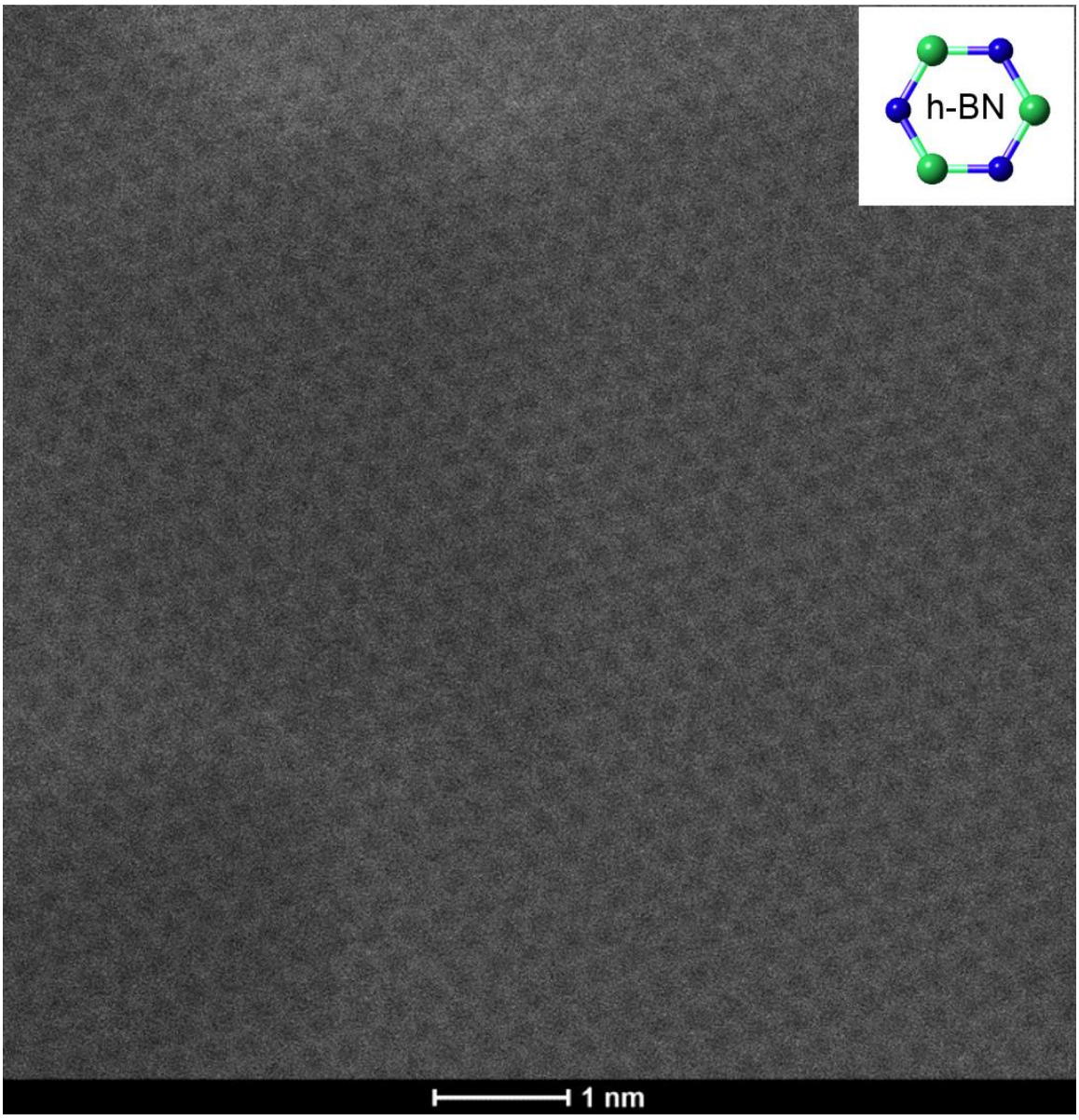

Figure 3.20. The high resolution STEM image of h-BN, the inset illustrates the crystal structure of h-BN.

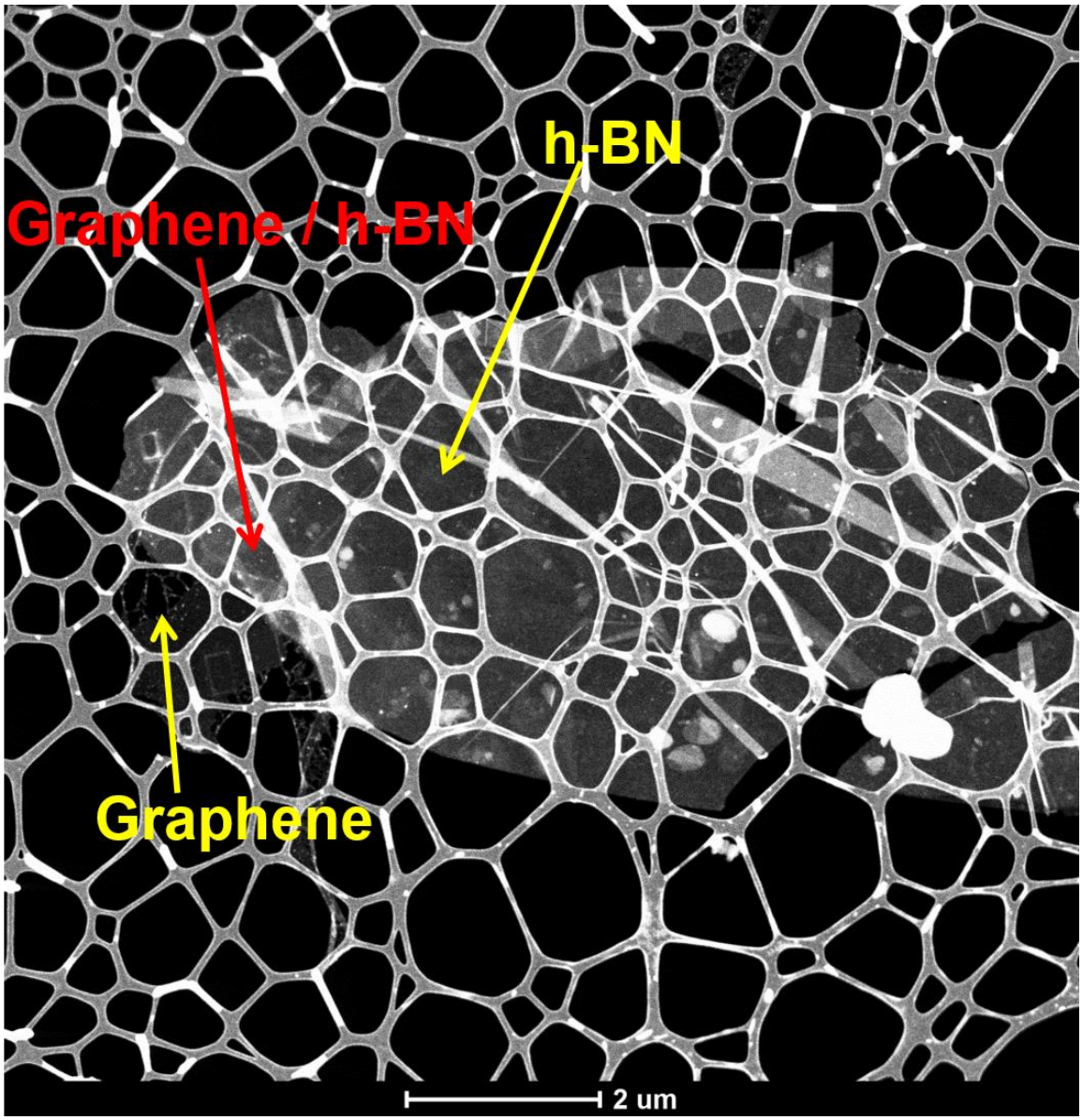

Figure 3.21. Low magnification STEM Image of graphene / h-BN.

Electron energy loss spectroscopy (EELS) is an analytical technique that evaluates the change on kinetic energy of the inelastically scattered primary electrons upon the interaction with a sample in a modified STEM set up [55]. EELS provides information of the atomic structure and chemical properties of the sample within the limits of atomic

resolution [56, 57]. The EELS enable one to investigate the interface by detecting the electronic interaction supposedly takes place at van der Waals junction of graphene and h-BN. The **Figure 3.22** presents the core level EELS spectra of graphene/h-BN taken from the designated regions in low magnification STEM image (Fig. 3.21). The graphene only region of EELS spectra reveals Carbon K edge, however does not show any sign of Boron and Nitrogen K edge. Similarly, h-BN only region of EELS spectra reveals Boron and Nitrogen K edge, however does not show any sign of Carbon K edge. The core level EELS spectra does not show any difference in the electronic state between the junction and graphene, h-BN separate regions, thus we can conclude that the interlayer coupling did not occur or negligible at interface.

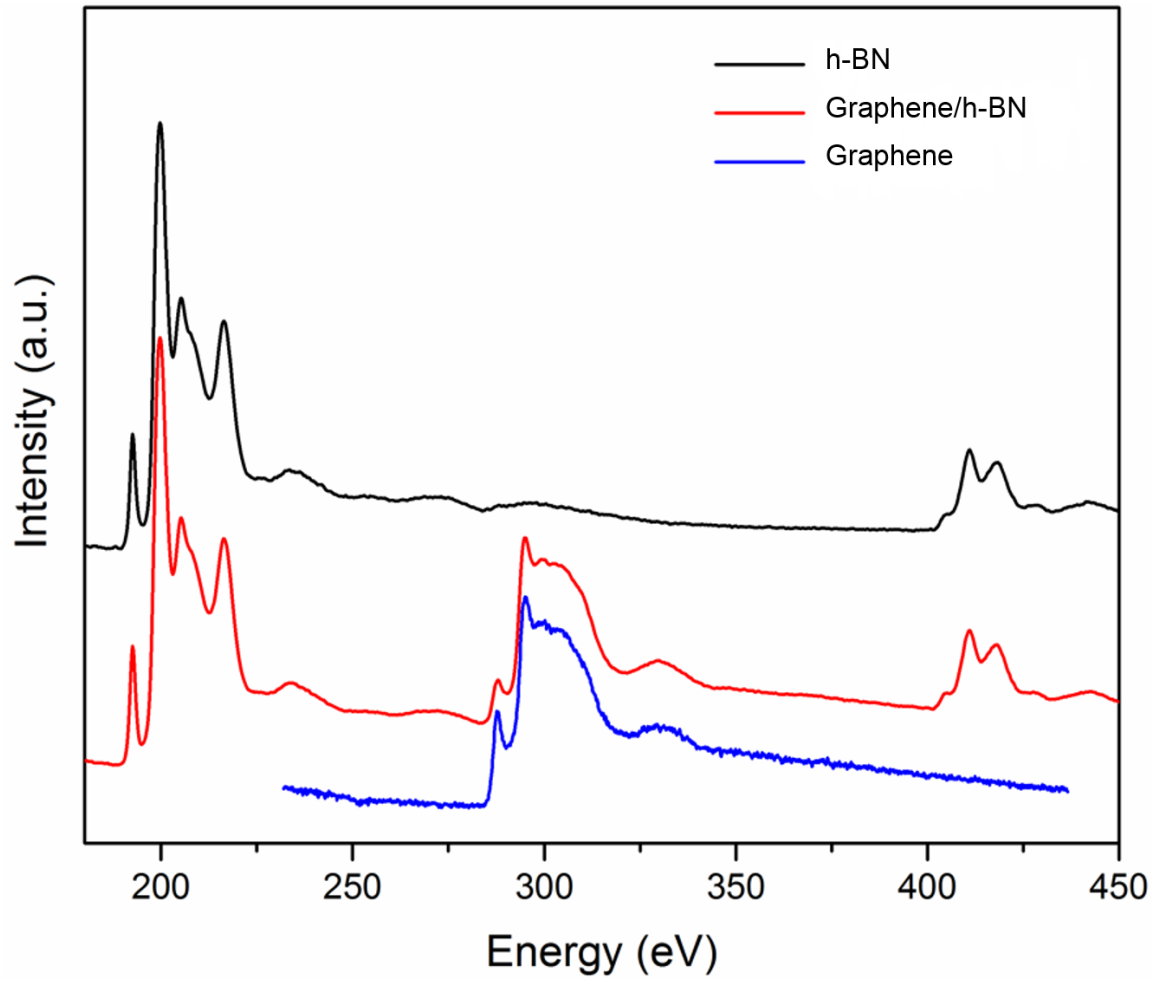

Figure 3.22. The core level EELS spectra of K shell excitations of graphene / h-BN.

Figure 3.23-25 present Boron K Edge, Carbon K Edge, and Nitrogen K Edge EELS spectra, at which the zoom in spectra are clearly shows that no electronic state coupling or hybridization between graphene and h-BN van der Waals structures at interface.

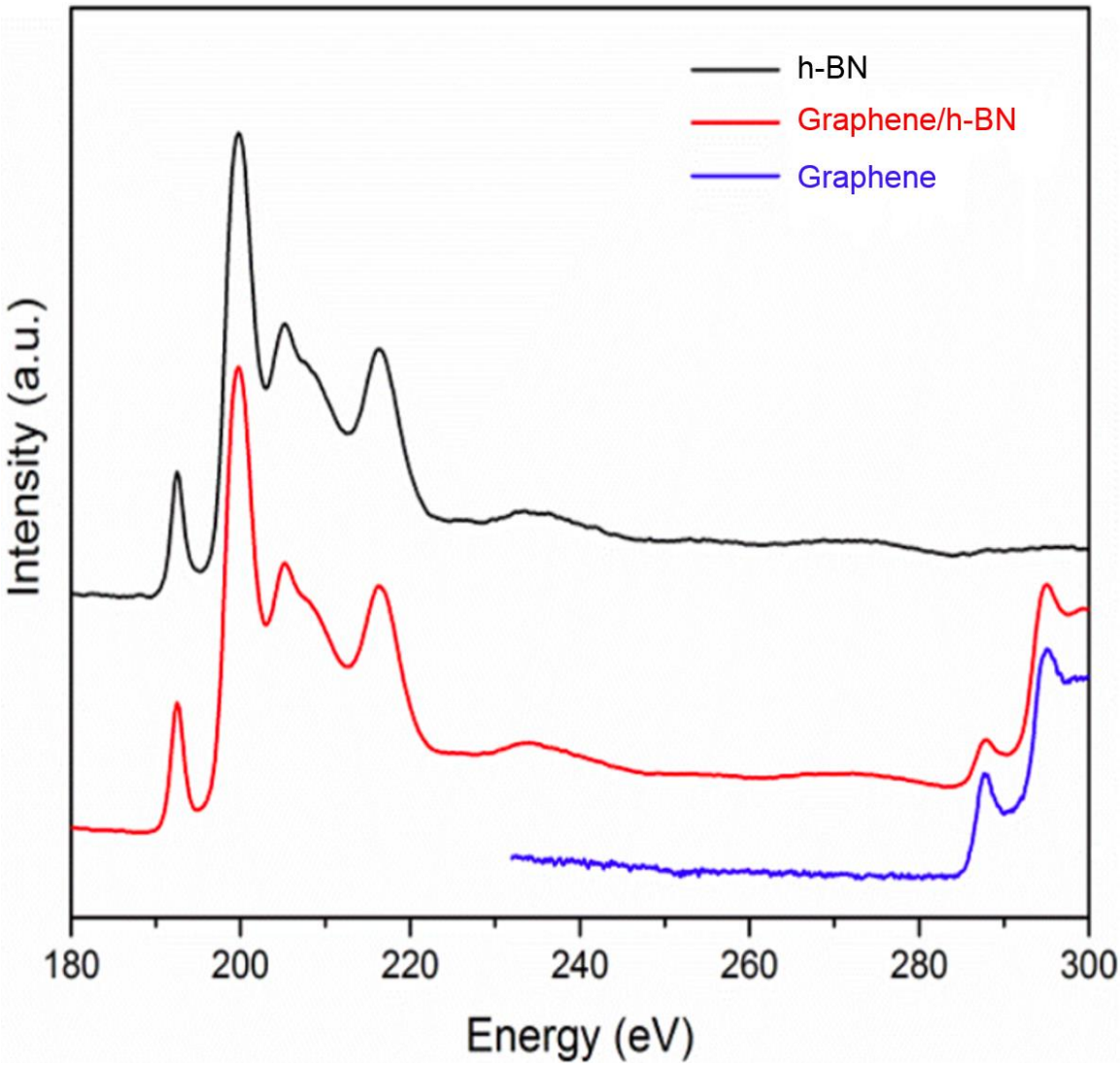

Figure 3.23. The zoom in core level Boron K shell excitations of EELS spectra of graphene/h-BN.

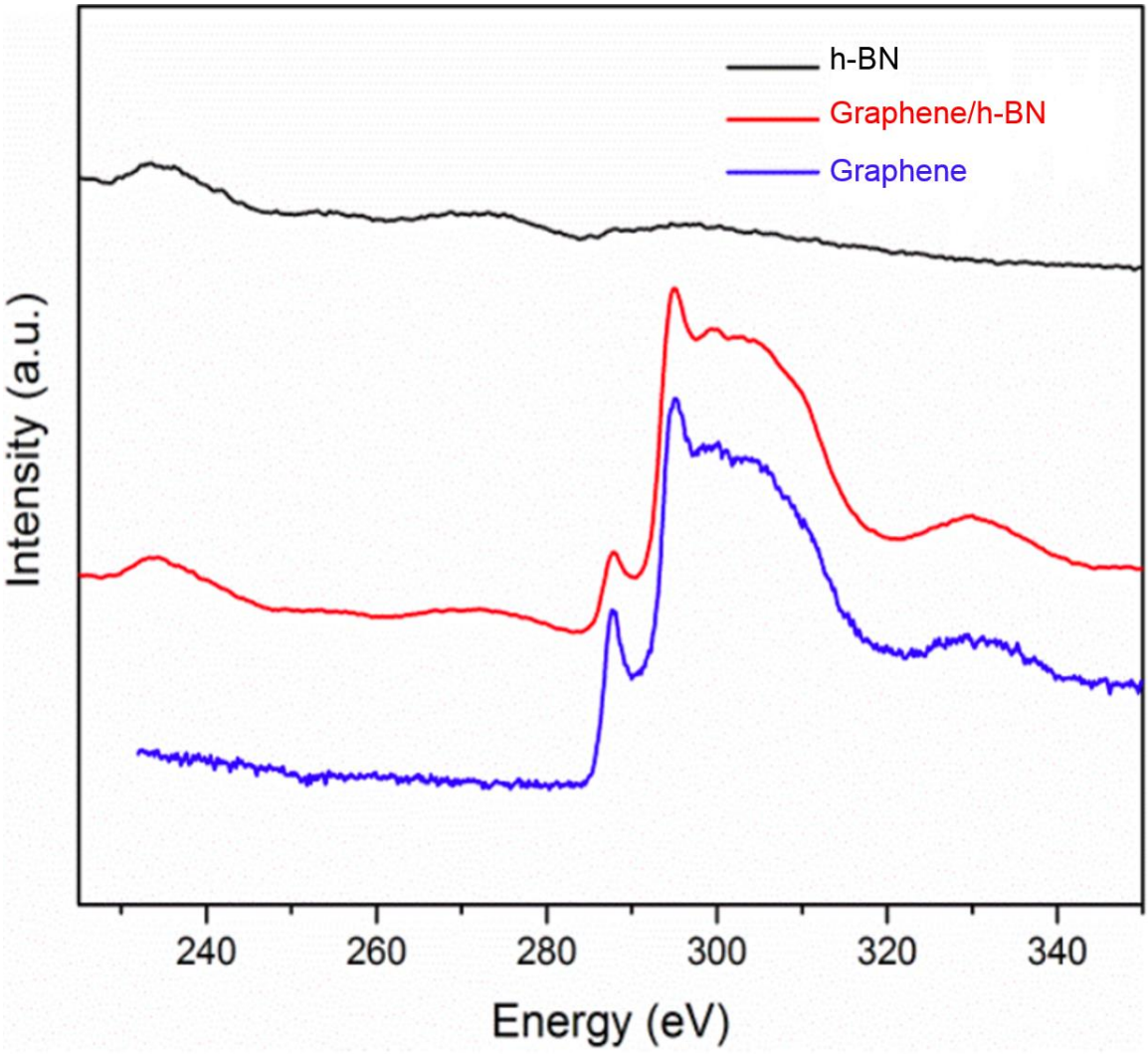

Figure 3.24. The zoom in core level Carbon K shell excitations of EELS spectra of graphene/h-BN.

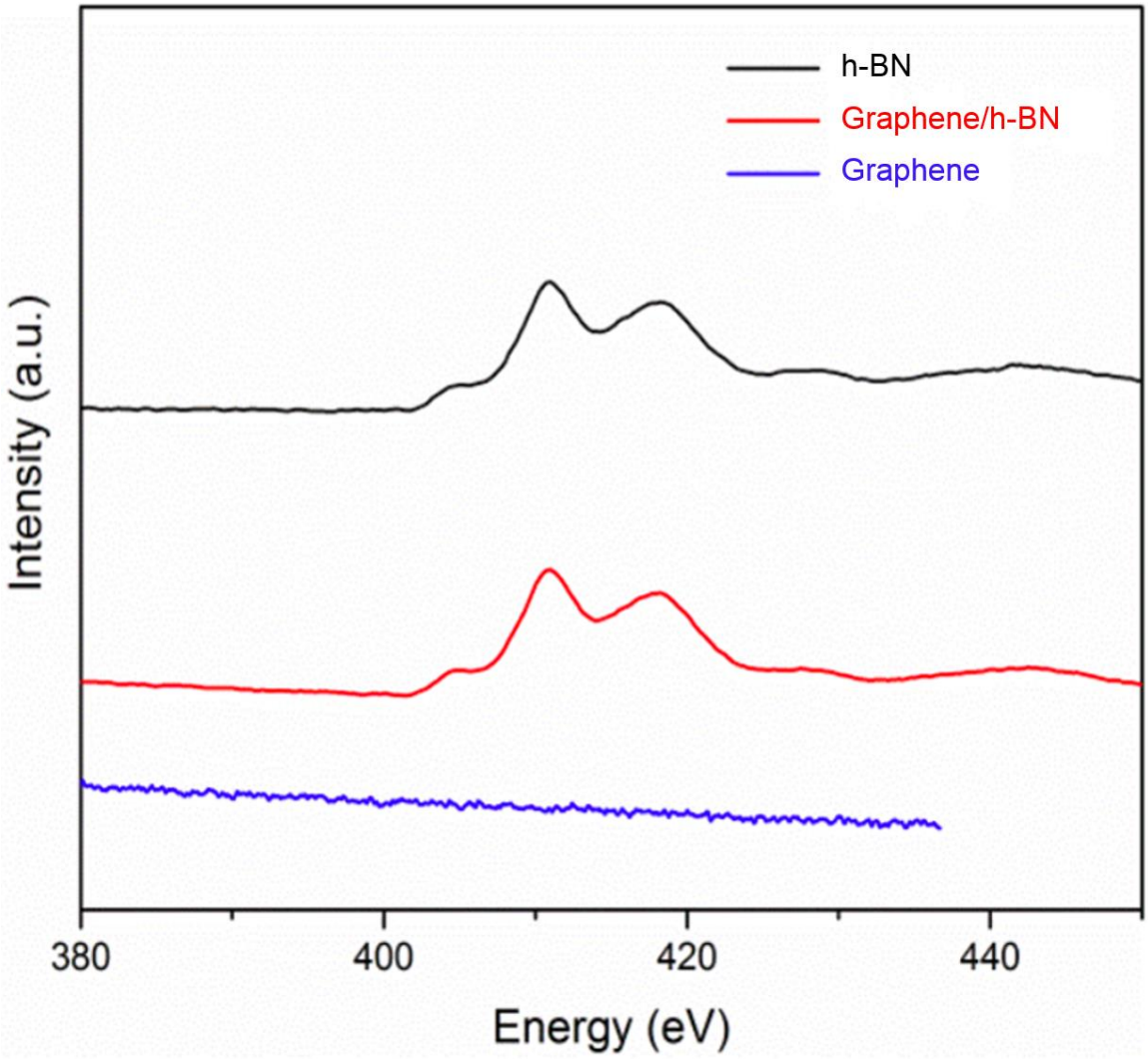

Figure 3.25. The zoom in core level Nitrogen K shell excitations of EELS spectra of Graphene/h-BN.

3.3.4. Energy Dispersive X-Ray Spectroscopy Analysis of Contamination of Graphene

Energy dispersive X-ray spectroscopy (EDX) is an analytical technique which is complementary to electron microscopy techniques. The emitted X-ray spectrum out of electron-specimen interaction provides the chemical information of the matter [58]. The

graphene's surface contamination is analyzed by EDX spectroscopy performed in STEM. **Figure 3.26** shows STEM high angle annular dark field (HAADF) image of graphene (**a**), and the corresponding EDX mappings of contaminants of Carbon (**b**), Oxygen (**c**), and Silicon (**d**). The EDX mappings of contaminants reveals that the graphene surface mainly consist of Carbon and Oxygen. Oxygen may be bonded to graphene during the transfer process because of breaking the Cu-Graphene bonding. There are also small amount of Silicon contamination may come from the quartz tube during the CVD growth of graphene.

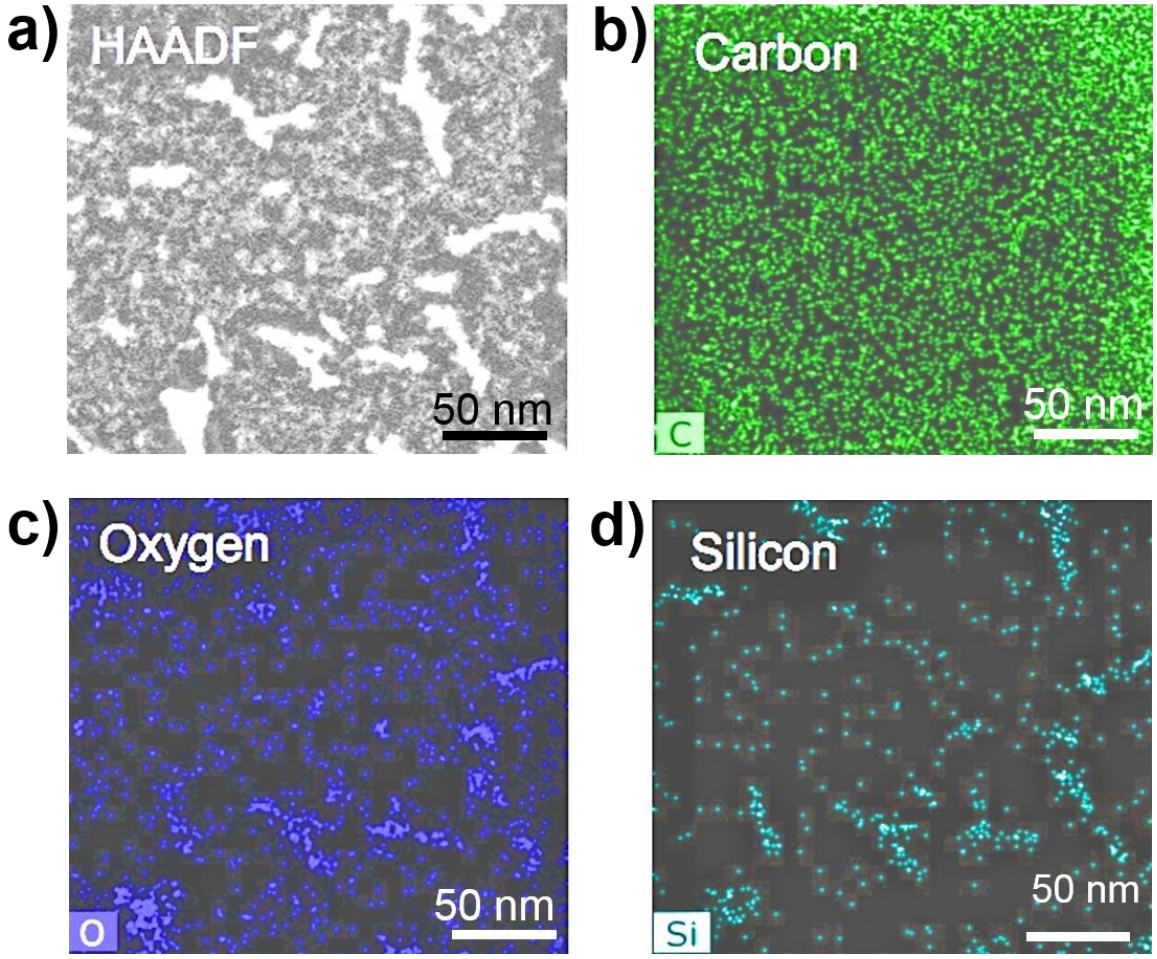

Figure 3.26. The HAADF image (**a**) and corresponding EDX Mappings of graphene crystal as EDX Carbon mapping (**b**), EDX Oxygen mapping (**c**), and EDX Silicon mapping (**d**).

3.4. Conclusions

The graphene research is involved in a large variety of applications in electronics, and remarkable improvement has been succeed on synthesis of these excellent materials. The graphene is considered as a clean interface thanks to characterization done by powerful tools of field such as Raman spectroscopy, SEM, STEM, etc. However, the high resolution STEM microscopy images at intermediate magnification reveals contaminated structure of

CVD grown graphene. The further sign of contamination has been experienced by performing EELS spectroscopy through investigation of fine structure of graphene/h-BN interface. The combined STEM and EELS spectra analysis has proved that the interlayer coupling at interface of graphene/h-BN heterostructures has not been detected. We attribute the lack of hybridization of electronic properties stems from the graphene surface contamination in atomic level.

CVD growth of graphene is a prevalent method with its scalability, uniformity, and repeatability, however it is momentous to obtain atomically clean graphene for sensitive device applications further beyond the current conventional technology.

3.5. References for chapter 3

[1] A. K. Geim and K. S. Novoselov: *The rise of graphene*. Nature Materials **6**, (2007) 183-191

[2] A.K. Geim: *Graphene: status and prospects.* Science **324,** no. 5934 (2009), 1530-1534

[3] AH Castro Neto, F. Guinea, Nuno MR Peres, Kostya S. Novoselov, and Andre K. Geim: *The electronic properties of graphene*. Reviews of modern physics **81**, no. 1 (2009) 109.

[4] N.D. Zhigadlo: *Crystal growth of hexagonal boron nitride (hBN) from Mg–B–N solvent system under high pressure*. Journal of Crystal Growth **402,** (2014) 308-311.

[5] D. Golberg, Y. Bando, Y. Huang, T. Terao, M. Mitome, C. Tang, and C. Zhi: *Boron nitride nanotubes and nanosheets*. ACS nano **4,** no. 6 (2010) 2979-2993.

[6] L. Liu, Y. P. Feng, and Z. X. Shen: *Structural and electronic properties of h-BN*. Physical Review B **68,** no. 10 (2003) 104102.

[7] L. Song, L. Ci, H. Lu, P. B. Sorokin, C. Jin, J. Ni, A. G. Kvashnin, D.G. Kvashnin, J. Lou, B.I. Yakobson, and P.M. Ajayan: *Large scale growth and characterization of atomic hexagonal boron nitride layers*: Nano letters **10**, no. 8 (2010) 3209-3215.

[8] N. Kostoglou, K. Polychronopoulou, and C. Rebholz: *Thermal and chemical stability of hexagonal boron nitride (h-BN) nanoplatelets*. Vacuum **112** (2015) 42-45.

[9] K. Watanabe, T. Taniguchi, and H. Kanda. Dire*ct-bandgap properties and evidence for ultraviolet lasing of hexagonal boron nitride single crystal*: Nature materials **3**, no. 6 (2004) 404.

[10] M. Xu, T. Liang, M. Shi, and H. Chen. *Graphene-like two-dimensional materials*: Chemical reviews **113**, no. 5 (2013) 3766-3798.

[11] T. Palacios: *Graphene electronics: thinking outside the silicon box*. Nature nanotechnology **6**, no. 8 (2011) 464-465.

[12] K.S. Novoselov, V. I. Fal, L. Colombo, P. R. Gellert, M. G. Schwab, and K. Kim: *A roadmap for graphene*: nature **490**, no. 7419 (2012) 192-200.

[13] S.J. Kim, K. Choi, B. Lee, Y. Kim, and B. H. Hong. *Materials for flexible, stretchable electronics: graphene and 2D materials*: Annual Review of Materials Research **45** (2015) 63-84.

[14] Z. Chen, Y.-M. Lin, M.J. Rooks, and P. Avouris: *Graphene nano-ribbon electronics*. *Physica E*: Low-dimensional Systems and Nanostructures **40**, no. 2 (2007) 228-232.

[15] G. Eda, and M. Chhowalla: *Graphene-based composite thin films for electronics:* Nano Letters **9**, no. 2 (2009) 814-818.

[16] S. Pang, Y. Hernandez, X. Feng, and K. Müllen: *Graphene as transparent electrode material for organic electronics.* Advanced Materials **23**, no. 25 (2011) 2779-2795.

[17] J. Hass, R. Feng, T. Li, X. Li, Z. Zong, W. A. De Heer, P. N. First, E. H. Conrad, C. A. Jeffrey, and C. Berger: *Highly ordered graphene for two dimensional electronics*. Applied Physics Letters **89**, no. 14 (2006) 143106.

[18] S. Dutta, and S.K. Pati: *Novel properties of graphene nanoribbons: a review*. Journal of Materials Chemistry **20**, no. 38 (2010) 8207-8223.

[19] M.J. Allen, V.C. Tung, and R.B. Kaner: *Honeycomb carbon: a review of graphene.*" Chemical reviews **110**, no. 1 (2009) 132-145.

[20] C. Berger, Z. Song, T. Li, X. Li, A.Y. Ogbazghi, R. Feng, Z. Dai, A.N. Marchenkov, E.H. Conrad, P.N. First, and W. A de Heer: *Ultrathin epitaxial graphite: 2D electron gas properties and a route toward graphene-based nanoelectronics*. The Journal of Physical Chemistry B **108**, no. 52 (2004) 19912-19916.

[21] F. Schwierz: *Graphene transistors*. Nature nanotechnology **5**, no. 7 (2010) 487-496.

[22] H.J. Yoon, J.H. Yang, Z. Zhou, S.S. Yang, and M.M-Cheng Cheng: *Carbon dioxide gas sensor using a graphene sheet*. Sensors and Actuators B: Chemical **157**, no. 1 (2011) 310-313.

[23] Y. Liu, X. Dong, and P. Chen*: Biological and chemical sensors based on graphene materials*. Chemical Society Reviews **41**, no. 6 (2012) 2283-2307.

[24] K.H. Lee, H.-J. Shin, J. Lee, I. Lee, G. Kim, J. Choi, and S. Kim: *Large-scale synthesis of high-quality hexagonal boron nitride nanosheets for large-area graphene electronics.* Nano letters **12**, no. 2 (2012) 714-718.

[25] C.R. Dean, A.F. Young, I. Meric, C. Lee, L. Wang, S. Sorgenfrei, K. Watanabe, T. Taniguchi, P. Kim, K.L. Shepard, and J. Hone: *Boron nitride substrates for high-quality graphene electronics*. Nature nanotechnology **5**, no. 10 (2010) 722-726.

[26] K.K. Kim, A. Hsu, X. Jia, S.M. Kim, Y. Shi, M. Dresselhaus, T. Palacios, and J. Kong: *Synthesis and characterization of hexagonal boron nitride film as a dielectric layer for graphene devices*. ACS nano **6**, no. 10 (2012) 8583-8590.

[27] W. Gannett, W. Regan, K. Watanabe, T. Taniguchi, M. F. Crommie, and A. Zettl: *Boron nitride substrates for high mobility chemical vapor deposited graphene*. Applied Physics Letters **98**, no. 24 (2011) 242105.

[28] L. Ci, L. Song, C. Jin, D. Jariwala, D. Wu, Y. Li, A. Srivastava, Z.F. Wang, K. Storr, L. Balicas, F. Liu, and P.M. Ajayan: *Atomic layers of hybridized boron nitride and graphene domains*. Nature materials **9**, no. 5 (2010) 430.

[29] R. Decker, Y. Wang, V.W. Brar, W. Regan, H.-Z. Tsai, Q. Wu, W. Gannett, A. Zettl, and M.F. Crommie*: Local electronic properties of graphene on a BN substrate via scanning tunneling microscopy*. Nano letters **11**, no. 6 (2011) 2291-2295.

[30] G. Giovannetti, P.A. Khomyakov, G. Brocks, P.J. Kelly, and J.V.D. Brink: *Substrate-induced band gap in graphene on hexagonal boron nitride: Ab initio density functional calculations*. Physical Review B **76**, no. 7 (2007) 073103.

[31] K.S. Novoselov, A. Mishchenko, A. Carvalho, and A.H.C. Neto: *2D materials and van der Waals heterostructures*. Science **353**, no. 6298 (2016) aac9439.

[32] I.V. Antonova: *Vertical heterostructures based on graphene and other 2D materials*. Semiconductors **50**, no. 1 (2016) 66-82.

[33] F. Withers, O.D P-Zamudio, A. Mishchenko, A. P. Rooney, A. Gholinia, K. Watanabe, T. Taniguchi, S.J. Haigh, A.K. Geim, A.I. Tartakovskii, and K.S. Novoselov: *Light-emitting diodes by band-structure engineering in van der Waals heterostructures*. Nature materials **14**, no. 3 (2015) 301-306.

[34] A. Pant, Z. Mutlu, D. Wickramaratne, H. Cai, R.K. Lake, C.S. Ozkan, and S. Tongay: *Fundamentals of lateral and vertical heterojunctions of atomically thin materials*. Nanoscale **8**, no. 7 (2016) 3870-3887.

[35] L. Wang, B. Wu, J. Chen, H. Liu, P. Hu, and Y. Liu: *Monolayer Hexagonal Boron Nitride Films with Large Domain Size and Clean Interface for Enhancing the Mobility of Graphene‐Based Field‐Effect Transistors*. Advanced Materials **26**, no. 10 (2014) 1559-1564.

[36] R.I. Lewis and H. Edwards: *Handbook of Raman spectroscopy: from the research laboratory to the process line*. CRC Press, 2001.

[37] S.L. Zhang: *Raman spectroscopy and its application in nanostructures*. John Wiley & Sons, 2012.

[38] X. Zhang, X.-F. Qiao, W. Shi, J.-B. Wu, D.-S. Jiang, and P.-H. Tan: *Phonon and Raman scattering of two-dimensional transition metal dichalcogenides from monolayer, multilayer to bulk material*. Chemical Society Reviews **44**, no. 9 (2015) 2757-2785.

[39] D. Yoon, H. Moon, H. Cheong, J.S. Choi, J.A. Choi, and B.H. Park: *Variations in the Raman Spectrum as a Function of the Number of Graphene Layers*. J. Korean Phys. Soc **55**, no. 3 (2009) 1299-1303.

[40] J. Zabel, R.R. Nair, A. Ott, T. Georgiou, A.K. Geim, K.S. Novoselov, and C. Casiraghi: *Raman spectroscopy of graphene and bilayer under biaxial strain: bubbles and balloons*. Nano letters **12**, no. 2 (2012) 617-621.

[41] A.C. Ferrari: *Raman spectroscopy of graphene and graphite: disorder, electron–phonon coupling, doping and nonadiabatic effects*. Solid state communications **143**, no. 1 (2007) 47-57.

[42] Y.Y. Wang, Z.H. Ni, T. Yu, Z.X. Shen, H.M. Wang, Y.H. Wu, W. Chen, and A.T.S. Wee: *Raman studies of monolayer graphene: the substrate effect*. The Journal of Physical Chemistry C **112**, no. 29 (2008) 10637-10640.

[43] Z.H. Ni, H. M. Wang, J. Kasim, H. M. Fan, T. Yu, Y. H. Wu, Y. P. Feng, and Z. X. Shen: *Graphene thickness determination using reflection and contrast spectroscopy*. Nano letters **7**, no. 9 (2007) 2758-2763.

[44] A.C. Ferrari, and D.M. Basko: *Raman spectroscopy as a versatile tool for studying the properties of graphene*. Nature nanotechnology **8**, no. 4 (2013) 235-246.

[45] R. Beams, L.G. Cançado, and L. Novotny: *Raman characterization of defects and dopants in graphene.* Journal of Physics: Condensed Matter **27**, no. 8 (2015) 083002.

[46] S. Reich, A. C. Ferrari, R. Arenal, A. Loiseau, I. Bello, and J. Robertson: *Resonant Raman scattering in cubic and hexagonal boron nitride*. Physical Review B **71**, no. 20 (2005) 205201.

[47] R.V. Gorbachev, I. Riaz, R.R. Nair, R. Jalil, L. Britnell, B.D. Belle, E.W. Hill, K.S. Novoselov, K. Watanabe, T. Taniguchi, A.K. Geim, and P Blake: *Hunting for monolayer boron nitride: optical and Raman signatures*. Small **7**, no. 4 (2011) 465-468.

[48] A. Eckmann, J. Park, H. Yang, D. Elias, A.S. Mayorov, G. Yu, R. Jalil, K.S. Novoselov, R.V. Gorbachev, M. Lazzeri, and A.K. Geim: 2013. *Raman fingerprint of aligned graphene/h-BN superlattices*. Nano letters **13,** no. 11(2013) pp.5242-5246.

[49] C. Neumann, L. Banszerus, M. Schmitz, S. Reichardt, J. Sonntag, T. Taniguchi, K. Watanabe, B. Beschoten, and C. Stampfer: *Line shape of the Raman 2D peak of graphene in van der Waals heterostructures*. physica status solidi b **253**, no. 12 (2016) 2326-2330.

[50] H. Wang, C. Yamada, and Y. Homma: *Scanning electron microscopy imaging mechanisms of CVD-grown graphene on Cu substrate revealed by in situ observation*. Japanese Journal of Applied Physics **54**, no. 5 (2015) 050301.

[51] Y. Cheng, Y. Song, D. Zhao, X. Zhang, S. Yin, P. Wang, M. Wang, Y. Xia, S. Maruyama, P.Zhao, and H. Wang: *Direct identification of multilayer graphene stacks on copper by optical microscopy*, Chemistry of Materials **28,** no. 7 (2016) 2165-2171.

[52] J, Borysiuk, R. Bożek, W. Strupiński, A. Wysmołek, K. Grodecki, R. Stępniewski, and J.M. Baranowski: *Transmission electron microscopy and scanning tunneling microscopy investigations of graphene on 4 H-SiC (0001)*. Journal of Applied Physics, **105**, no. 2 (2009) 023503.

[53] U. Bangert, M. Gass, R. Zan, and C.T. Pan: *Scanning transmission electron microscopy and spectroscopy of suspended graphene*. In Physics and Applications of Graphene-Experiments. InTech (2011).

[54] N. Alem, R. Erni, C. Kisielowski, M.D. Rossell, W. Gannett, and A. Zettl: Atomically thin hexagonal boron nitride probed by ultrahigh-resolution transmission electron microscopy. Physical Review B **80**, no. 15 (2009) 155425.

[55] F. Hofer, F. P. Schmidt, W. Grogger, and G. Kothleitner: *Fundamentals of electron energy-loss spectroscopy*. IOP Conference Series: Materials Science and Engineering **109**, no. 1 (2016) 012007

[56] L.S. Panchakarla, K.S. Subrahmanyam, S.K. Saha, A. Govindaraj, H.R. Krishnamurthy, U.V. Waghmare, and C.N.R. Rao: *Synthesis, Structure, and Properties of Boron- and Nitrogen- Doped Graphene*. Advanced Materials, **21**, no. 46 (2009) 4726-4730.

[57] M.H. Gass, U. Bangert, A.L. Bleloch, P. Wang, R.R. Nair, and A. K. Geim: *Free-standing graphene at atomic resolution*. Nature nanotechnology **3**, no. 11 (2008) 676-681.

[58] S. Yang, X. Feng, L. Wang, K. Tang, J. Maier, and K. Müllen: *Graphene- Based Nanosheets with a Sandwich Structure*. Angewandte Chemie International Edition **49**, no. 28 (2010) 4795-4799.

Chapter 4. The Study of Second Order Resonant Raman Scattering on Layered Metal Dichalcogenides and Their Heterostructures

Abstract:

The Atomically thin layered metal and transition metal dichalcogenides are recently emerging concentration of materials research thanks to their unique physical, chemical, and electronic properties. Raman spectroscopy is a versatile and non-destructive technique for the identification of structural properties and phonon features of atomically thin layered materials. Especially, the second order resonant Raman spectroscopy, which can be applied to the resonance conditions in energy of the incoming photon and interband transitions of an electron in a crystal lattice, reveals additional phonon modes to typical Raman active modes in the spectra. Various 2D materials, including $SnSe_2$, WSe_2, SnS_2, and $MoTe_2$, and their heterostructures are fabricated by dry transfer method as a top-down approach. The vibrational characteristics of these 2D materials systems are unambiguously established by using second order Resonant Raman spectroscopy.

4.1. Introduction

Atomically thin layered materials are single or few layers of sheets of materials in which atoms form strong chemical bonds in plane, while weak van der Waals bonds take place between the layers of sheets. In these materials; electrons are free to move in two dimensions, but its movements are restricted in the third direction. This quantum mechanical confinement effect of electrons give rise to interesting properties such as;

exceptional electronic and heat conductivity, dangling bond free and extremely smooth interfaces, energy independent step-like density of states, etc. These materials are expected to form the future electronics by involving as the channel or base material in device applications such as; transistors, sensors, solar cells, semiconductors, battery electrodes, and spin devices. The applications of these novel materials are directly related to their fundamental properties. Raman spectroscopy is a powerful tool to characterize and analyze the most possible states of these materials. The results of Raman spectroscopy are directly related to structural properties of atomically thin layered materials [1].

Atomically thin layered materials family consist of a wide range of different characteristic materials including graphene, metal dichalcogenides, transition metal dichalcogenides (TMDs), topological insulators (TIs), insulators, semiconductors, super conductors, transition metal oxides (TMOs). The metal and transition metal dichalcogenides materials are represented by the MX_2 formulation (M: Mo, W, Sn; X: S, Se, Te). Each layer consists by repeating X-M-X type unit cell, and different stacking orders of layers designate the crystal structures. The electronic properties are correlated to the crystal structure and symmetry groups of these materials [2]. TMDs (WSe_2, MoS_2, $MoTe_2$, etc) are usually crystallized in 2H (trigonal prismatic molecular geometry) polytype structure and belong to D_{6h} group, while metal dichalcogenides $SnSe_2$ and SnS_2 are mostly crystallized in and 1T (octahedral molecular geometry) type structure belong to D_{3d} group. However, the symmetry shows different behavior in bulk and few layer or monolayer forms since the translational symmetry around z-axis exists in bulk crystals only. For example, D_{6h} group symmetry of bulk form of TMDs is reduced to D_{3d} and D_{3h}

group symmetries for even layer numbers and odd layer numbers crystals, respectively. Therefore, the physical and electronic properties of 2D layered materials crucially depend on their layer thickness [3]. The Raman spectroscopy is the most versatile tool to determine the most characteristic properties of atomically thin layered materials and their heterostructures by providing information about stacking order, thickness, crystalline quality, chemical and structural modifications, interlayer interaction, etc. [4]. Raman spectroscopy is a method based on the evaluation of the backscattered light from a material to probe its lattice vibrations and phonon dispersion [5]. Lattice vibrations are systematized by the irreducible representation of the symmetry group of the crystals, and the optical and acoustic phonons are able to be designated from this set of vibration modes [6-9]. The phonon modes for bulk MX_2 type materials with D_{6h} group symmetry are given by $\Gamma_{bulk}= A_{1g} + 2A_{2u} + 2B_{2g} + B_{1u} + E_{1g} + 2E_{1u} + 2E_{2g} + E_{2u}$, where A_{1g}, E_{1g}, and E_{2g} are Raman active modes, while A_{2u} and E_{1u} are acoustic modes. The phonon modes for few layer MX_2 type materials with D_{3d} group symmetry is given by $\Gamma= 3A_{1g} + 3A_{2u} + 3E_g + 3E_u$, where A_{1g}, and E_g modes are Raman active, while A_{2u}, and E_u are acoustic modes. The phonon modes for few layer MX_2 type materials with D_{3h} group symmetry are given by $\Gamma=2A''_2 + A'_1 + 2E' + E''$, where A'_1, and E'' are Raman active, while one of the A'' and E' are acoustic modes[2] [3]. The Raman active modes are the E symmetry modes stem from in-plane, and the A symmetry modes stem from out of plane vibrations, which are called shear and breathing modes, respectively. The E symmetry modes are two-fold degenerate, while the A modes are non-degenerate.

The low frequency Raman investigation provides critical insights on weak interlayer interactions of van der Waals type heterostructures that are formed by the integration of MX_2 type materials together [10]. The low frequency interlayer shear mode is defined as the oscillation of which the amplitude is perpendicular to the normal of the planes. The low frequency interlayer breathing mode is defined as the oscillation of which the amplitude is parallel to the normal of the plane.

Heterojunctions of materials with different characteristic properties present a useful foundation to discover, understand, and optimize complex condensed matter systems that its properties are shaped by new physical states. The non- resonant Raman spectroscopy provides information about the interaction between the incident photon and crystal lattice through Raman active vibration modes at the center of the Brillouin zone. On the other hand, the second order resonant Raman spectroscopy (two phonon involves) provides elaborate information on especially very thin sheets of transition metal dichalcogenides by revealing infrared active and optically inactive modes in addition to Raman active modes thanks to the resonance conditions of incoming photon energy and interband transitions of an electron from occupied to unoccupied state [11, 12]. The second order resonant Raman scattering is a process that enables the inactive phonon modes, at the edge of the Brillouin zone to, be probed by enhancing the scattered signal due to the resonance between incoming photon with excitonic transitions. The second order Raman process is dispersive with respect to energy of the incoming photon; hence it is related to the electronic structure of the semiconductor materials due to the nature of excitonic interactions. The second order resonant spectra do not only reveals structural information of TMDs, but also specifies the

phonon behavior, which is critical in terms of thermal, electrical conductivity and many other technical aspects in terms of application point of view. In the case of WSe_2, the two-longitudinal acoustic phonons mode (2LA(M)) appears in the spectra as a result of resonant excitation resonant excitation at the M point of the Brillouin zone [13]. There is still not a final agreement on the peak assignments around wavenumber of 245 cm^{-1} and 265 cm^{-1}, on the Raman spectra of WSe_2. To understand 2LA(M) phonon mode is very important since it is located in the close proximity to degenerate E^1_{2g} and A_{1g} peaks. The previous studies have ignored the 2LA(M) phonon mode [14, 15], however recent studies have shown the E^1_{2g} and A_{1g} modes appear as one peak, and second order resonant phonon mode (2LA(M)) appears as an another peak [16]. We have shown that the E^1_{2g} and A_{1g} peaks are split, and the 2LA(M) peak appears as a third peak around that wavenumber range. We believe that the splitting effect has been observed due to local wrinkles induced strain effects. As a contribution to ongoing discussion about the peak assignment, it is proved that the degeneracy of the E^1_{2g} and A_{1g} modes can be lifted. In addition, the red shift of the 2LA(M) peak with the increasing thickness also provides useful information on the synthesis of these materials.

Similar to WSe_2, we have observed the second order resonant phonon modes for $MoTe_2$. Two-phonon transverse acoustic mode (2TA(M)), at the M point of the Brillouin zone, appears in the Raman spectra of $MoTe_2$. The 2TA(M) mode exhibits a blue shift with increasing thickness. Another inactive mode of B^1_{2g} appears in spectra in resonance with the incoming photon. The B^1_{2g} mode also provides information about thickness due to its appearance that is limited for monolayer and bulk, but only for few layers.

The Raman spectroscopy demonstrates properties of vertically stacked layers of atomically thin layered materials by differentiating the response of in plane, out of plane, interlayer shear and breathing modes. The resonant Raman spectroscopy investigation have been conducted to $SnSe_2$, SnS_2, and heterostructures of $SnSe_2/WSe_2$ and $SnS_2/MoTe_2$.

4.2. Methods

4.2.1. Materials Synthesis

The few layer crystals were micromechanically exfoliated from their single crystal bulk form on the SiO_2/Si (300 nm thick Oxide layer for effective optical contrast) substrates by using scotch tape, or PDMS stamps. The heterostructures were achieved on SiO_2/Si wafers by using dry transfer tool. The dry transfer method allows one to determine the desired orientation and selection of flakes in micro-scale. In the dry transfer method, one specific type of 2D material is transferred onto a PDMS (**Figure 4.1 a, b**), while another specific type 2D material is transferred onto a SiO_2/Si (**Figure 4.1 b, c**) substrate. The dry transfer tool (**Figure 4.2**) is able to integrate dissimilar materials by proximity of stamp to Si substrate through intermediate-controlled contact of two materials in a very short time period. The step by step detailed images of fabrication of $SnSe_2/WSe_2$ is shown in **Figure 4.3.** The heterostructures can be treated by applied heat to eliminate the water bubbles formed at the junction.

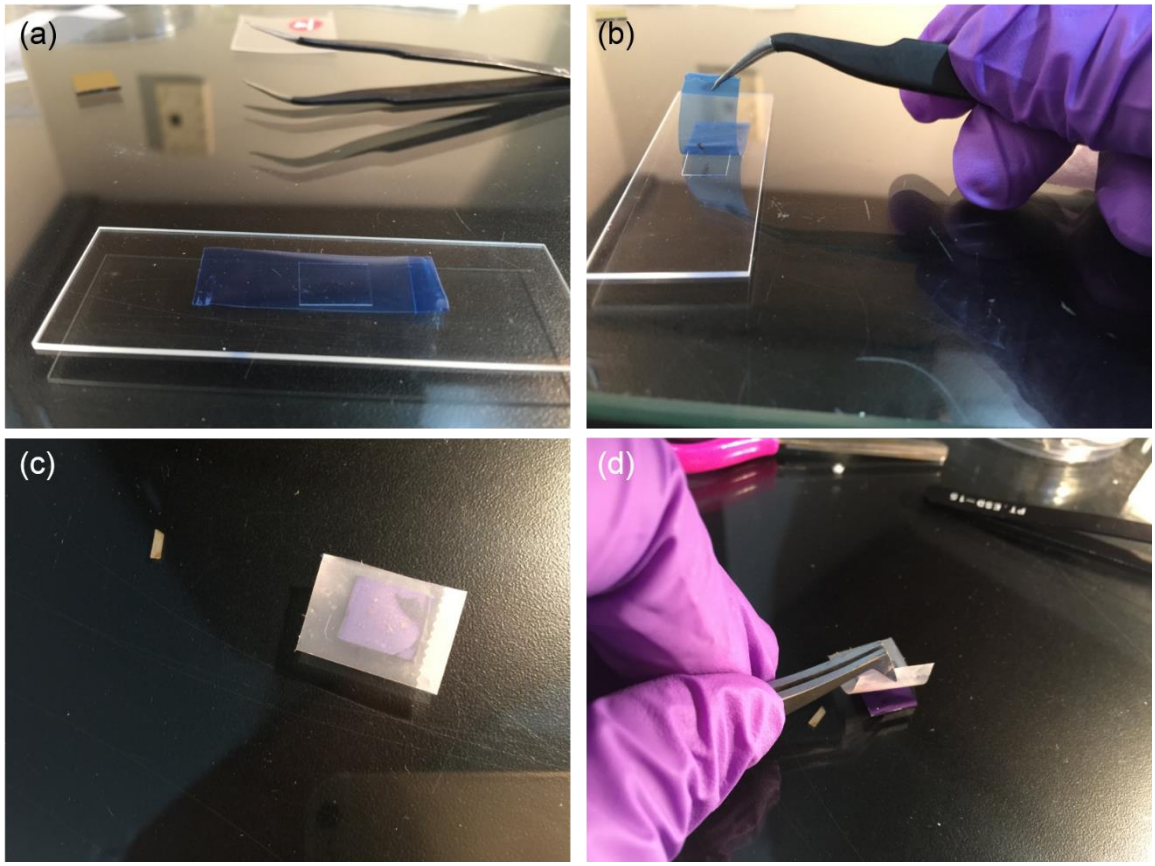

Figure 4.1.The micromechanical exfoliation of 2D layered materials. Materials transferred onto PDMS (**a, b**) and SiO_2/Si (**c, d**).

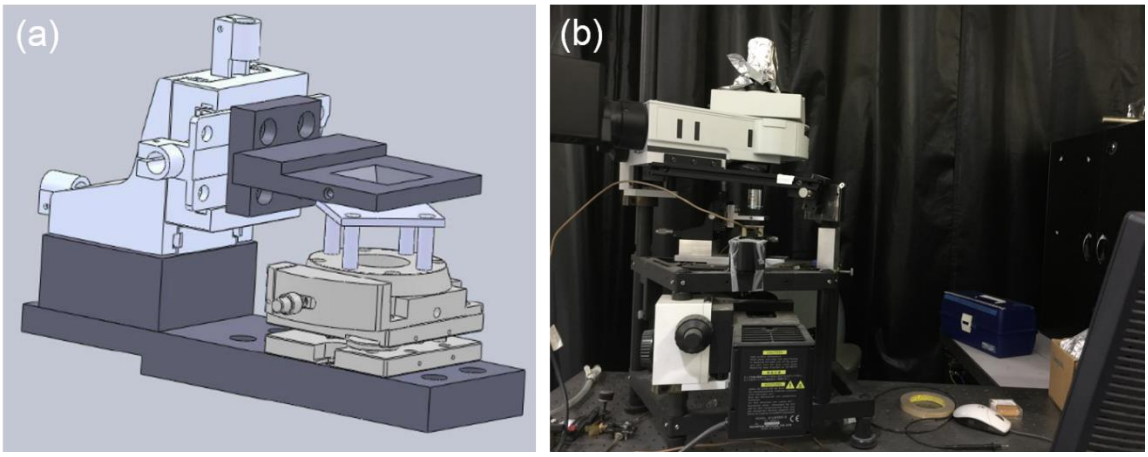

Figure 4.2. The transfer tool for heterostructures assembly. The schematic (**a**) and actual picture (**b**) of the transfer tool.

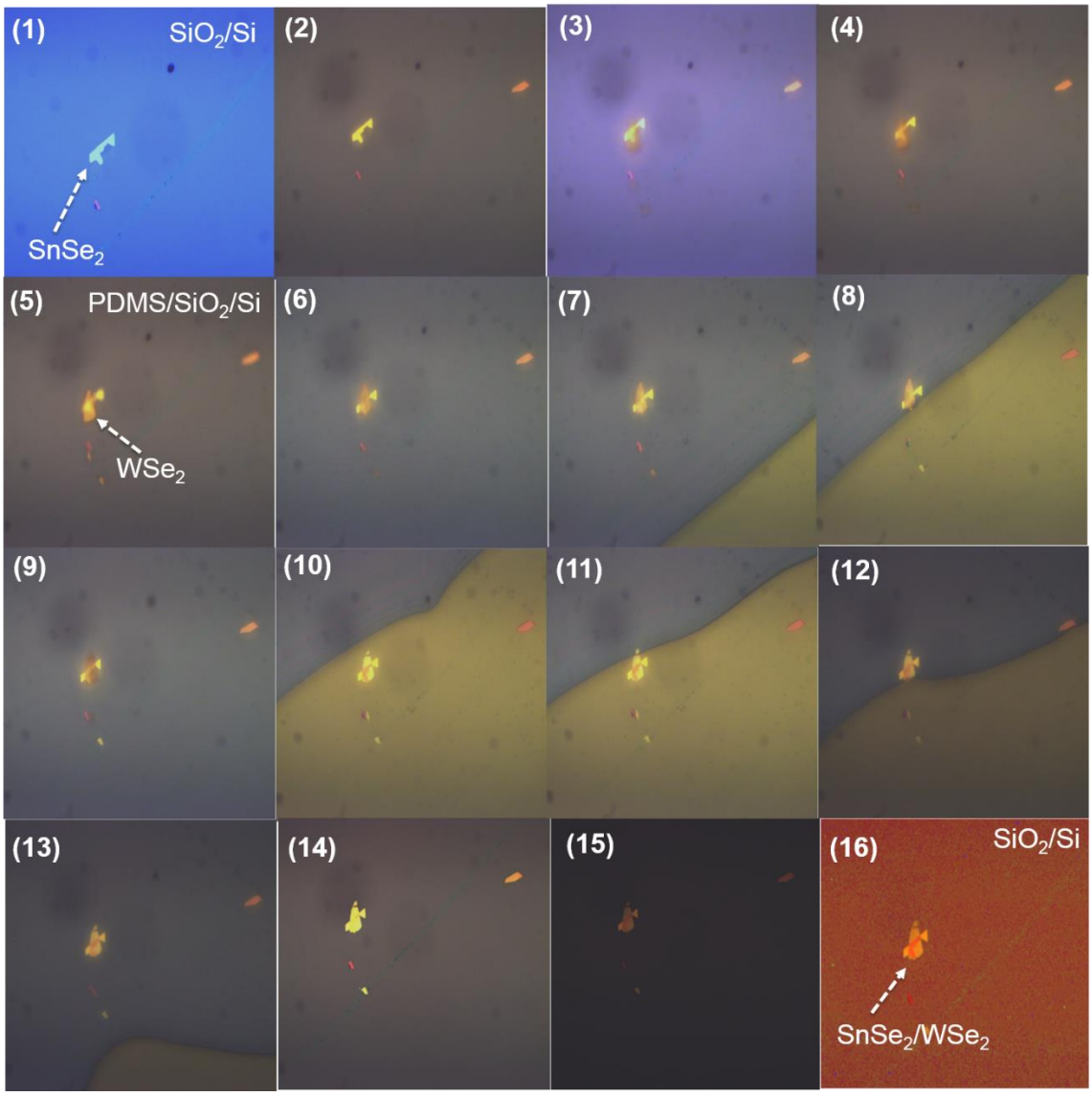

Figure 4.3. The heterostructures assembly process by dry transfer tool method.

4.2.2. Materials Characterization

The Raman spectroscopy measurements were performed by using 532 nm and 633 nm excitation by solid state lasers. The magnification for the objective lens was 100x, and

groove density was 1800 g/mm. The laser power was kept below 300 μW in order to avoid the effect of local heating. The PL measurements were performed by using 2.33 eV laser with the laser power of 200 μW.

4.3. Results

4.3.1. $SnSe_2$

The two-dimensional MX_2 (M: transition and main group metal, X: chalcogenide) type materials are mostly crystallized in 2H and 1T types structures with D_{6h} and D_{3d} point-group symmetry, respectively [17, 18]. The crystal structure of $SnSe_2$ is classified in many polytypes resulting the wide spectrum of physical and chemical properties. The various combinations of crystal orientations of $SnSe_2$ promises broad range of applications due to the distinct electronic and optical properties in different polytypes. $SnSe_2$ has been mostly studied on their 2H form, however there has been limited studies done on 1T form. Herein, we study the 1T stacking order of $SnSe_2$ single crystals [19, 20] with D_{3h} group symmetry in monolayer, few layer, and bulk form since the symmetry group does not depend on thickness for this specific polytype. **Figure 4.4** displays the optical microscopy image of multilayer $SnSe_2$ exfoliated on SiO_2/Si substrates (300 nm thick oxide layer for the best optical contrast). The thin and thick regions of the $SnSe_2$ crystal can be distinguished by the difference of the optical contrast of the reflected light.

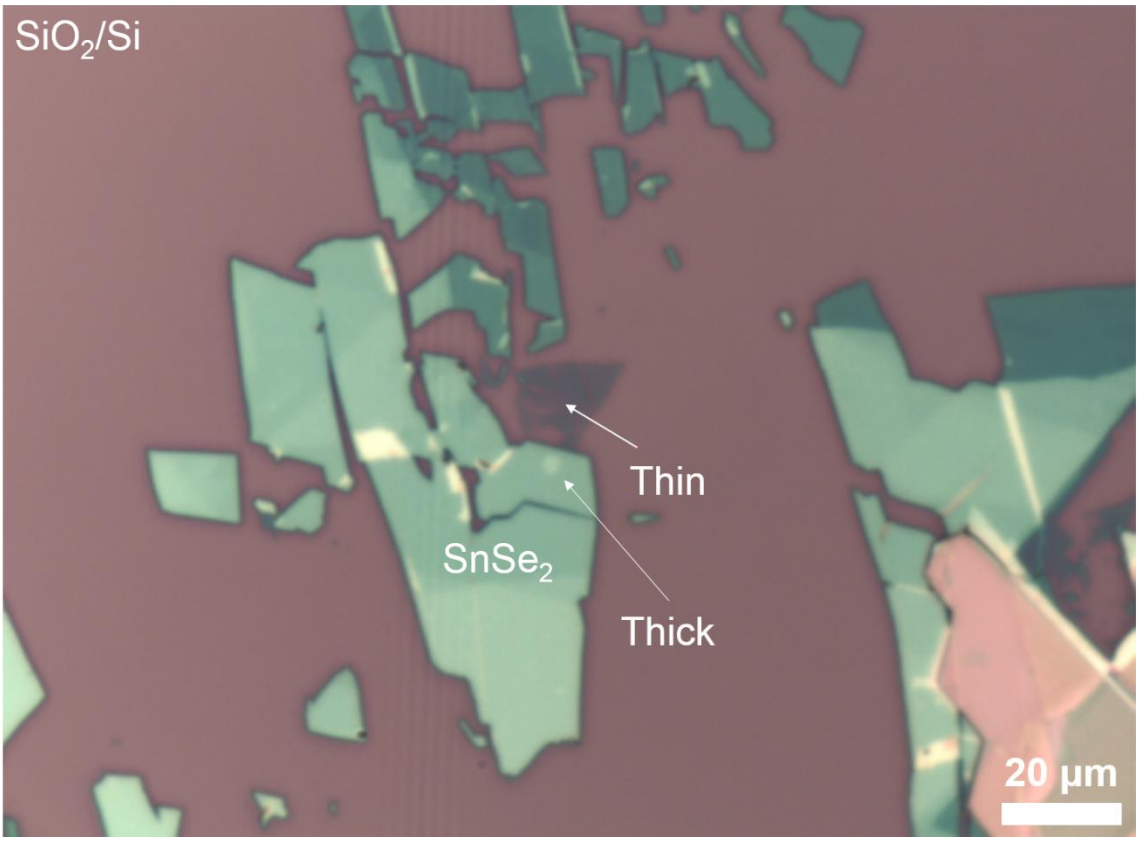

Figure 4.4. The optical microscopy image of $SnSe_2$ flakes of thin and thick regions on SiO_2/Si substrate.

`The Raman spectroscopy characterization of $SnSe_2$ single crystal is an effective method that provides structural and chemical identification [21, 22]. For 1T polytype $SnSe_2$, the irreducible representation of 12 vibrational modes at the center of Brillouin zone is given by $\Gamma = A_{1g} + E_g + 2A_{2u} + 2E_u$ [23].

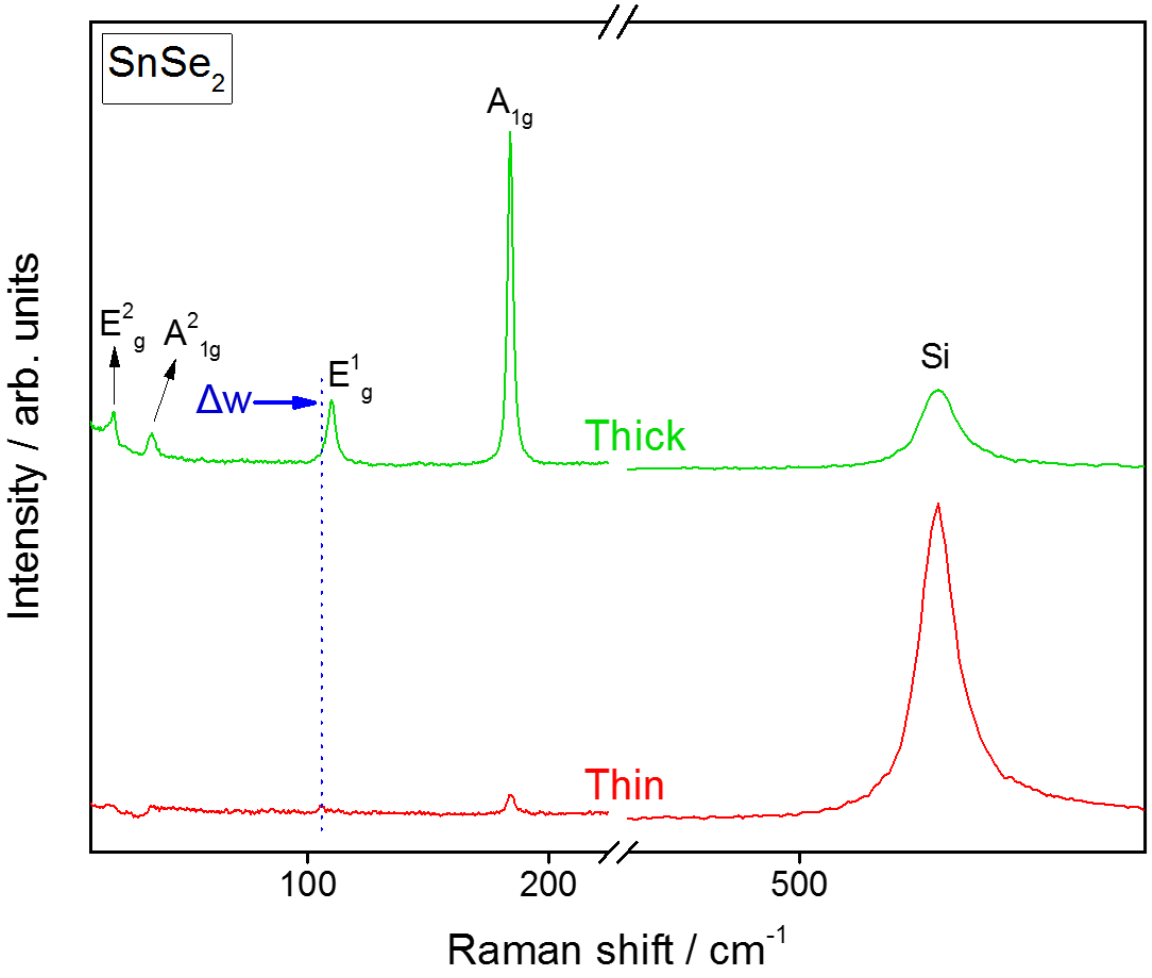

Figure 4.5. The Raman spectra were taken from thin and thick regions of $SnSe_2$ crystals.

The Raman spectra were taken from two different regions (thin and thick) of a flake of the $SnSe_2$ crystals on SiO_2/Si substrate (**Figure 4.5**). The Raman spectra taken from the thick region exhibits four Raman active modes, which are the typical in plane vibration mode of E^1_g (109.8 cm^{-1}), and out of plane vibration mode of A_{1g} (184.1 $cm^{-1)}$ and additional two low frequency interlayer shear and breathing modes namely E^2_g (19.6 cm^{-1}) and A^2_{1g} (35.3 cm^{-1}), respectively. For the thin region of the flake, the Raman spectra reveals two Raman active modes as the shear and breathing modes were not exist. The in

plane E^1_g mode is located at the Raman wavenumber of 105.65 cm^{-1} while out of plane A_{1g} is at 184.2 cm^{-1}. The comparison of the Raman spectra of thin and thick regions demonstrates that there is a blue shift (4.2 cm^{-1}) on the E^1_g mode with increasing thickness of the $SnSe_2$. The blue shift of E^1_g mode implies that the stiffening of the in plane bonds. We did not observe any shift on out of plane A_{1g} mode with the function of layer thickness.

4.3.2. WSe_2

WSe_2 is a two-dimensional layered semiconductor material that belongs to TMDs family in the MX_2 form. In each plane, one Tungsten (W) atom is connected with two Selenium (Se) atoms via covalent bonding, while the adjacent layers are coupled with each other by weak van der Waals interaction resulting the trigonal prismatic molecular orientation. WSe_2 crystallized in the 2H structure with D_{6h} group symmetry for bulk form. WSe_2 samples are synthesized by the micromechanical exfoliation method as top down approach for isolation of few layer thick crystals from its bulk form. **Figure 4.6** displays the optical microscopy image of WSe_2 crystals on SiO_2/Si substrate (300 nm oxide thickness).

The irreducible phonon representations of modes of WSe_2 in bulk form are given as $\Gamma = A_{1g} + 2A_{2u} + B_{1u} + 2B_{2g} + E_{1g} + 2E_{1u} + E_{2u} + 2E_{2g}$. There are four Raman active modes, which are A_{1g}, E_{1g}, E^1_{2g}, and E^2_{2g}. There are four infrared active modes, which are E^1_{1u}, E^2_{1u}, A^1_{2u}, and A^2_{2u}. There are also four optically silent modes, which are E_{2u}, B^2_{2g}, B_{1u}, and B^1_{2g}. The symmetry is reduced by the reducing thickness, the symmetry group of D_{6h} for bulk WSe_2 is reduced to D_{3h} (for odd number of few layers form) and D_{3d} (for even

number of few layers form) with the transition from bulk to few layers [24, 25]. Raman spectroscopy characterization of WSe_2 is very sensitive to laser power due to the vulnerable nature of low melting point materials open to immediate damage of local heating that alters the Raman scattering [26]. There is a discrepancy in the literature about the assignment of the two Raman peaks, which are located at the Raman wavenumber between 248 cm^{-1} and 262 cm^{-1}, of WSe_2 crystals. The Raman active E_{1g} mode is not observed in Raman spectra because the backscattering is forbidden.

Figure 4.7 presents the Raman spectra of bulk form WSe_2 exfoliated on SiO_2/Si substrate. The typical Raman peaks reveals two major high frequency peaks at the Raman wavenumber of 248.3 cm^{-1} and 257.4 cm^{-1} for bulk crystals. Although, the first peak was assigned as the in plane E^1_{2g} mode, there is no standard peak assignment for the latter peak. In the literature, some studies have assigned the second peak as out of plane A_{1g} mode at, however some studies recently have assigned this peak as the second order resonant Raman mode 2LA(M), which stems from the two-phonon scattering at the symmetry point of M at the Brillouin zone. The theoretical calculations state that the E^1_{2g} and A_{1g} modes are degenerate, and the peaks are overtone. The E^1_{2g} mode is the in plane displacement of W and Se atoms, and A_{1g} mode for the out of plane displacement of Se atoms. Sahin et al stated that the degeneracy between E^1_{2g} and A_{1g} modes is calculated that to be lifted by breaking symmetry to in monolayer WSe_2 [14], however empirical results do not verify this expectation due to substrate effect of uniaxial strain. The interlayer shear (E^2_{2g}) and breathing (B^2_{2g}) peaks are observed at 23.6 cm^{-1} and 36.3 cm^{-1}, respectively. The Raman active interlayer shear mode of E^2_{2g} is defined as the vibrations of adjacent layers as the

oscillation amplitude is perpendicular to the normal of the plane, and the optically inactive interlayer breathing mode of B^2_2 is defined as the vibrations of adjacent layers as the oscillation amplitude is parallel to the normal of the plane. The existence of B^2_{2g} mode in Raman spectra of WSe_2 is only possible for thre crystals that are thicker than three layers, hence it is not expect to observe this mode for the monolayer. The B^1_{2g} peak is located at the Raman wavenumber of 308.5 cm^{-1}. B^1_{2g} peak is theoretically defined and calculated as optically inactive mode. However, it is observed experimentally, which suggests that the breaking of selection rules for phonons due to excitonic resonant Raman scattering. Therefore, the appearance of the B^1_{2g} peak in the Raman spectra of WSe_2 depends on the wavelength of the incoming light since the resonance is required. The B^1_{2g} peak is observed in the Raman spectra of the WSe_2 crystals that are consist of double or thicker layers, hence it can also be employed for easy thickness assignment for monolayer crystals. The peaks at 359 cm^{-1} ($2E_{1g}$) and 373 cm^{-1} (A_{1g}+LA) are the combination of the scattering of $E^1_{2g,\,LO}$ +LA(M) and $E^1_{2g,TO}$+LA(M) phonons [27, 28].

Figure 4.8 displays optical microscopy image of few layer WSe_2 crystals on SiO_2/Si substrate (300 nm oxide thickness). The two different thickness of the flake can be distinguished from the optical contrast as the thin and thick regions.

Figure 4.9 presents the Raman spectra of the monolayer and few layer WSe_2 crystals exfoliated on SiO_2/Si substrate. It is expected to see lesser modes in the Raman spectra of monolayer due reducing symmetry. Indeed, we do not observe the interlayer shear (E^2_{2g}) and breathing (B^2_{2g}) modes, and other second other phonon modes. According

to the Raman footprint for the thickness determination of WSe_2, the B^1_{2g} mode is also not observed in the spectra taken monolayer. The Raman spectra comparison indicates that the 2LA(M) peak performs red shift (5 cm^{-1}) with increasing thickness from monolayer to few layers. The E^1_{2g} and A_{1g} peaks are located at the Raman wavelength of 250.3 cm^{-1} for monolayer WSe_2. The as E^1_{2g}, A_{1g} peaks are also shown to have small amount of red shift (0.5 cm^{-1}) with increasing thickness. In Raman spectroscopy, red shift implies that the softening of the bonds [28, 29].

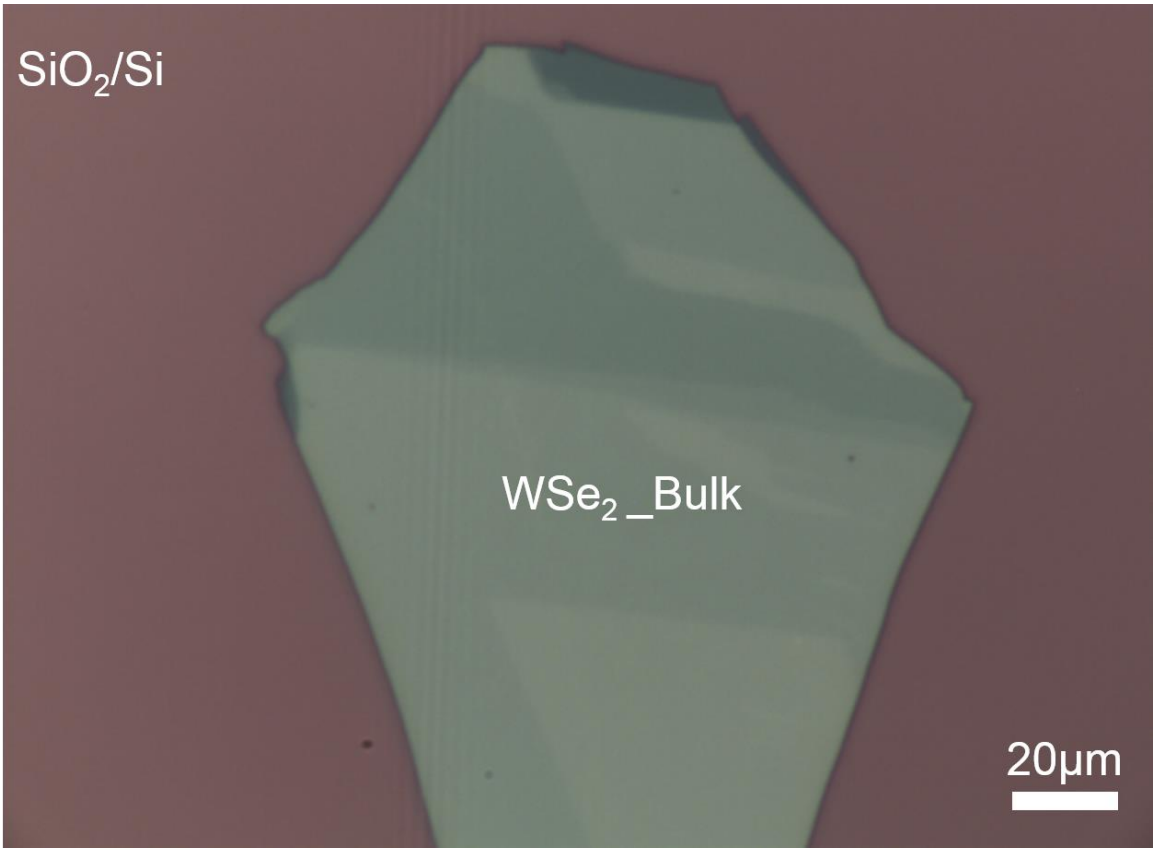

Figure 4.6. The Optical microscopy image of bulk WSe_2.

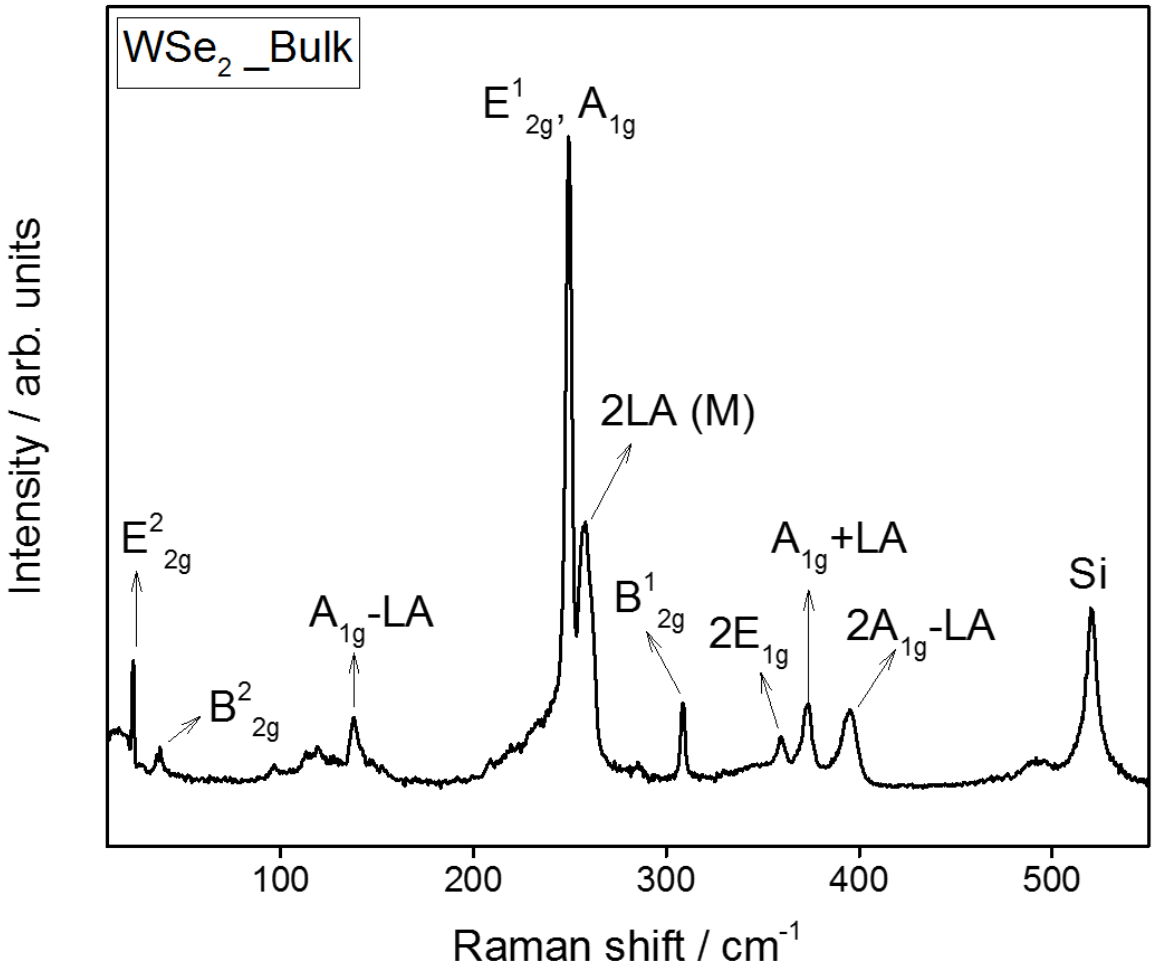

Figure 4.7. Raman spectra of bulk form WSe_2.

Figure 4.10 displays the optical microscopy image of WSe_2 homostructure that consists of three flakes stacked together by offset. The flake 1 (few layers) is stacked by two other thicker flakes on its sides. The Raman spectra (**Figure 4.11**) were taken from the flake at the middle as laser beam pointed. The Raman spectra reveal a clear splitting of phonon modes of E^1_{2g}, A_{1g}, and 2LA(M). We believe this is a confirmation of the theoretical calculations that indicates three different peaks, but never observed clearly to the date. We believe this is a result of strain induced by the stacking of three layers

vertically. The in plane covalent bonds are responsive to induced strain, hence the E^1_{2g} mode performs red shift, while the out of plane A_{1g} mode does not respond significantly.

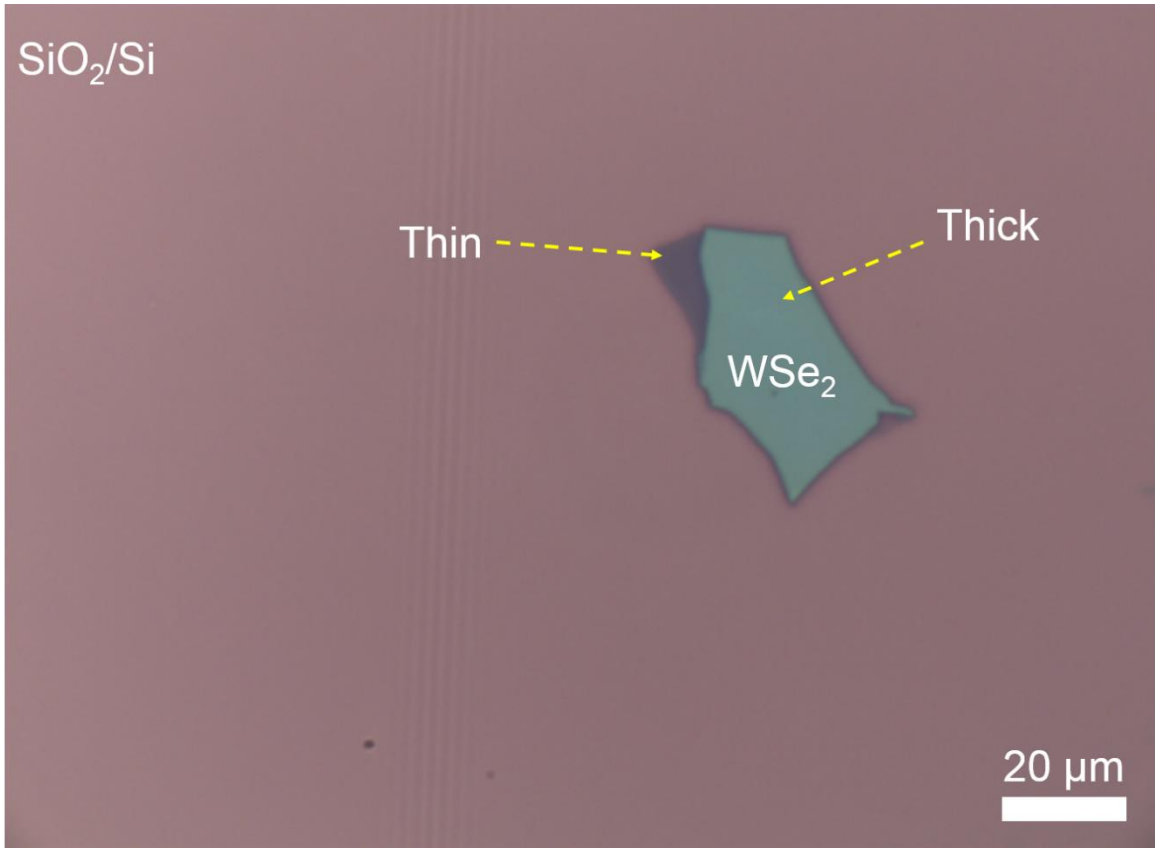

Figure 4.8. The optical microscopy image of few layer WSe_2.

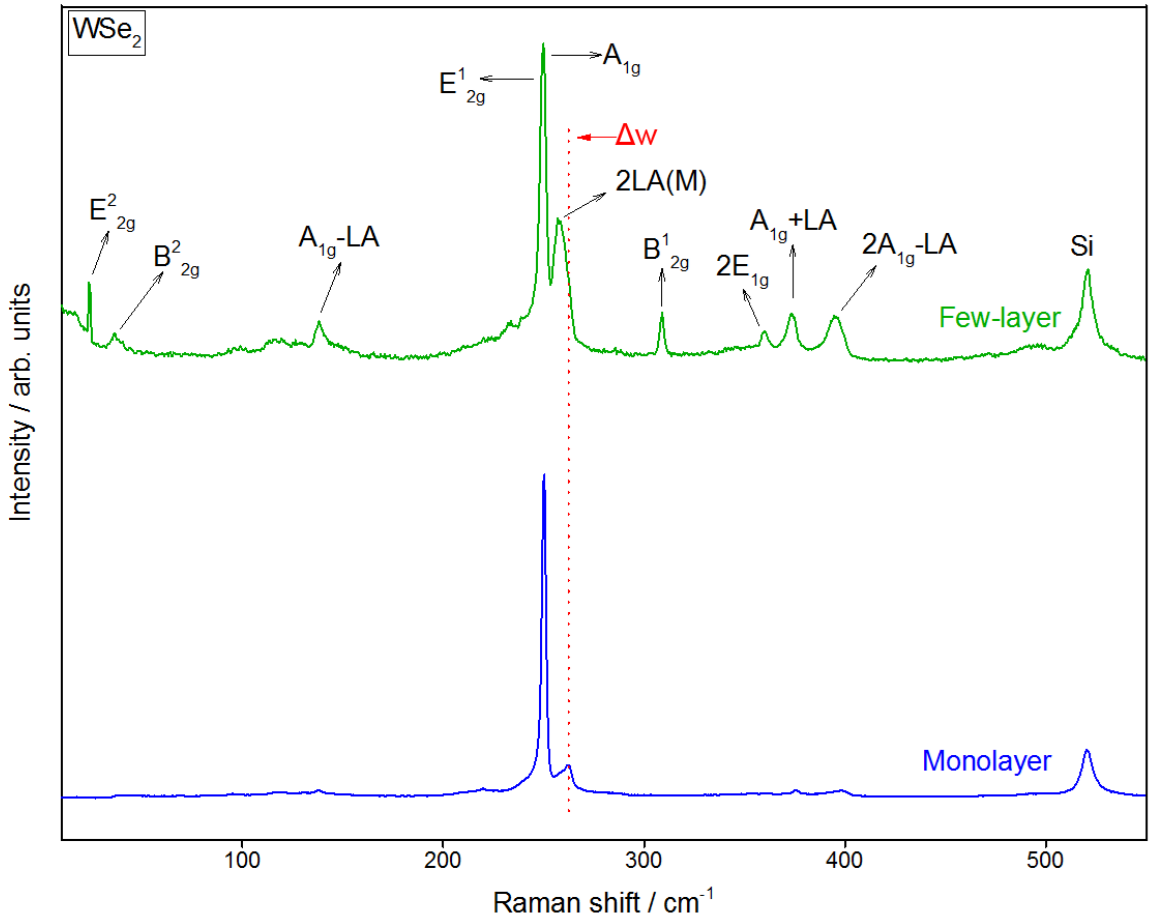

Figure 4.9. The Raman spectra of monolayer and few layers WSe_2.

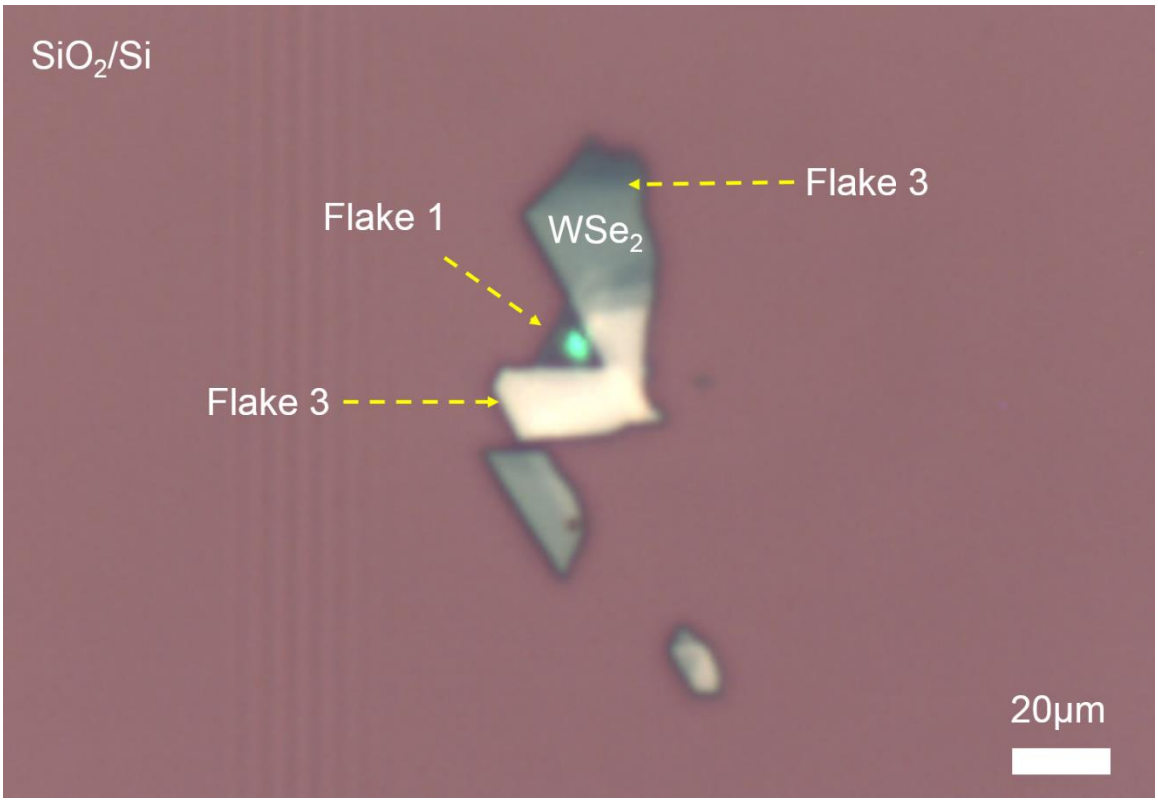

Figure 4.10. Optical microscopy image of few layer WSe_2 crystals.

.

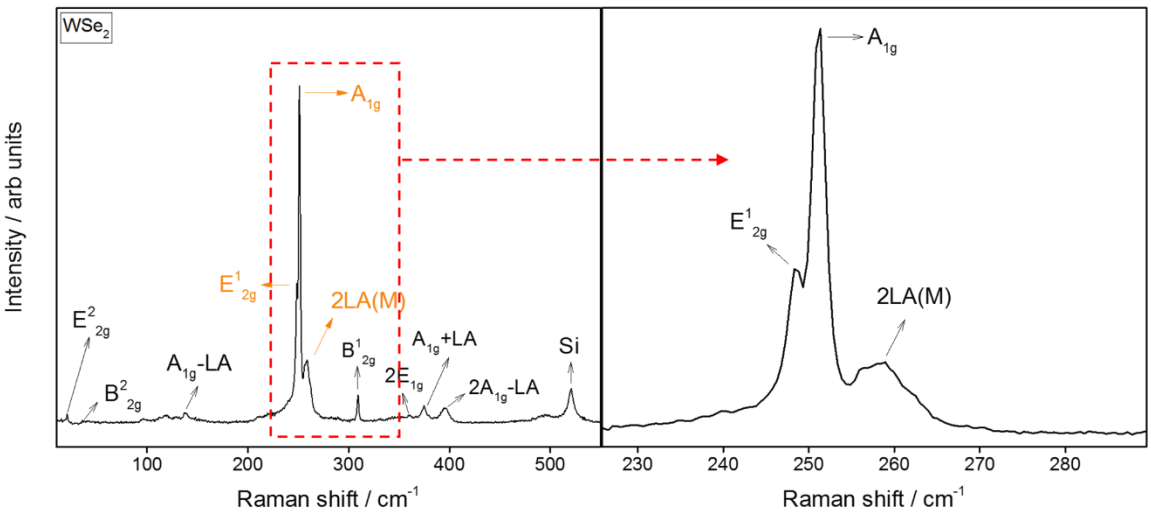

Figure 4.11. The Raman spectra taken from few layer WSe_2 (flake 1 in Fig 4.10).

WSe_2, as a member of the MX_2 type atomically thin layered semiconductor materials, exhibits indirect to direct electronic bandgap transition from bulk and few layers to monolayer. Photoluminescence (PL) spectroscopy is an easy method to confirm the monolayer crystals of WSe_2 thanks to the sharp PL peak assigned to the only monolayer form of these materials [30-32]. **Figure 4.12** presents the PL spectrum of monolayer WSe_2. The PL peak is located at the wavelength of 747.7 nm, which corresponds to 1.65 eV in energy. Therefore, we verified monolayer WSe_2 crystal with the measured direct electronic bandgap of 1.65 eV. We can confirm the synthesized monolayer WSe_2 by obtaining the high intensity sharp of PL peak, which is limited to occur in single layer due to direct bandgap transition.

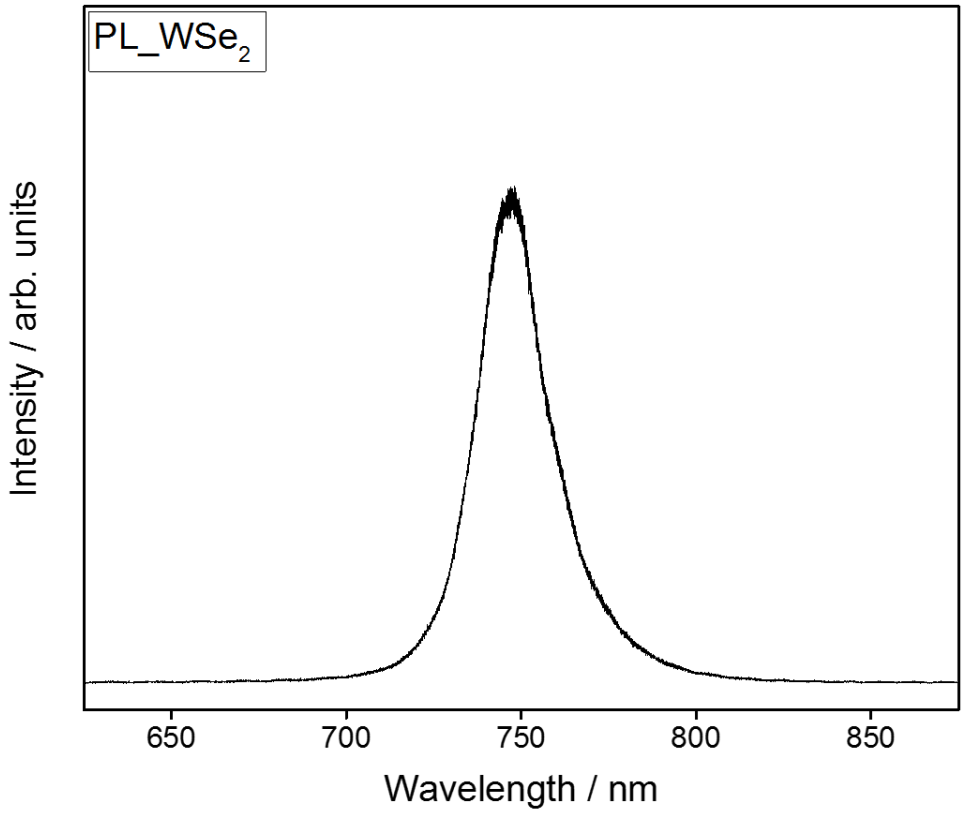

Figure 4.12. The PL spectra of monolayer WSe_2.

4.3.3. SnS_2

Tin disulfide (SnS_2), as a member of MX_2 type layered materials, is a popular material with promising physical, electronic, and chemical properties for advanced nanotechnology applications. SnS_2 can exist in the form of diverse polytype due to various stacking order of layers that consist of covalently bonded S-Sn-S atoms in a plane. The stacking is provided by weak van der Waals interactions between adjacent layers. Among many polytype, 2H and 1T are the common polytype thanks to their relatively stable conditions [33]. Herein, we study 2H type crystal orientation of SnS_2. We synthesize SnS_2 crystal on SiO_2/Si substrates by isolating thin layers from its bulk form by performing micromechanical exfoliation method. **Figure 4.13** displays the optical microscopy image of SnS_2 crystal on SiO_2/Si substrate with different thick regions can be distinguished from the optical contrast of the reflected light.

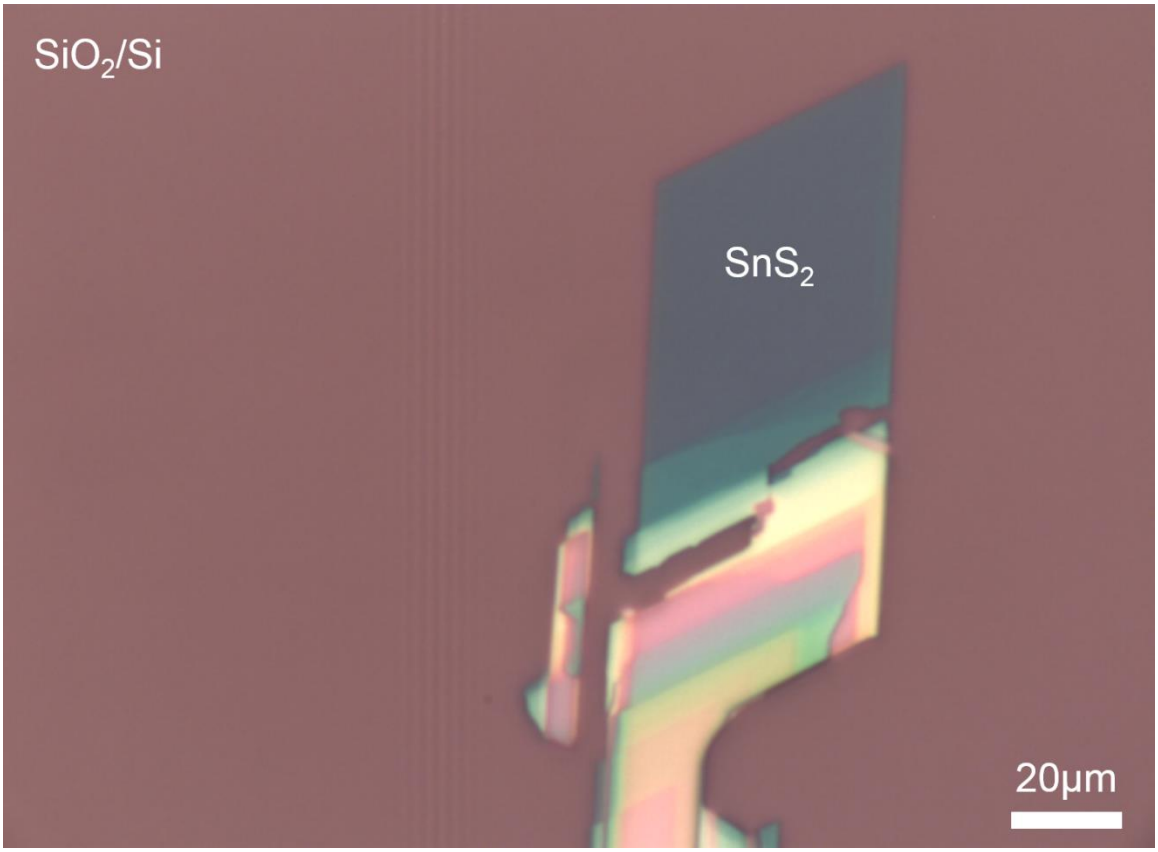

Figure 4.13. Optical microscopy image of SnS_2 on SiO_2/Si substrate.

The 2H form few layer SnS_2 has D_{3d} type group symmetry, the irreducible representation of the phonon modes at the center of Brillouin zone is given by $\Gamma = E_{2g} + A_{1g} + 2E_u + 2A_{2u}$. The out of plane A_{1g} and in plane E_{2g} are the Raman active modes, while E_u and A_{2u} are the acoustic modes. The **Figure 4.14** presents the Raman spectra taken from thin and thick regions of SnS_2 crystals on SiO_2/Si. There are two Raman active modes appear in the spectra as A_{1g} located at the Raman wavenumber of 315 cm^{-1}, and E_{2g} is located at the Raman wavenumber of 206 cm^{-1}. For the thin flake the in plane E_{2g} mode is not visible for the thin flakes. The A_{1g} and E_{2g} peaks show small thickness dependence on

the non-polarized Raman spectroscopy measurements except the disappearance of E_{2g} peak for the thin SnS_2. We believe polarized Raman spectroscopy measurement would shed light on the thickness and polytype determination of the SnS_2 crsytals [34].

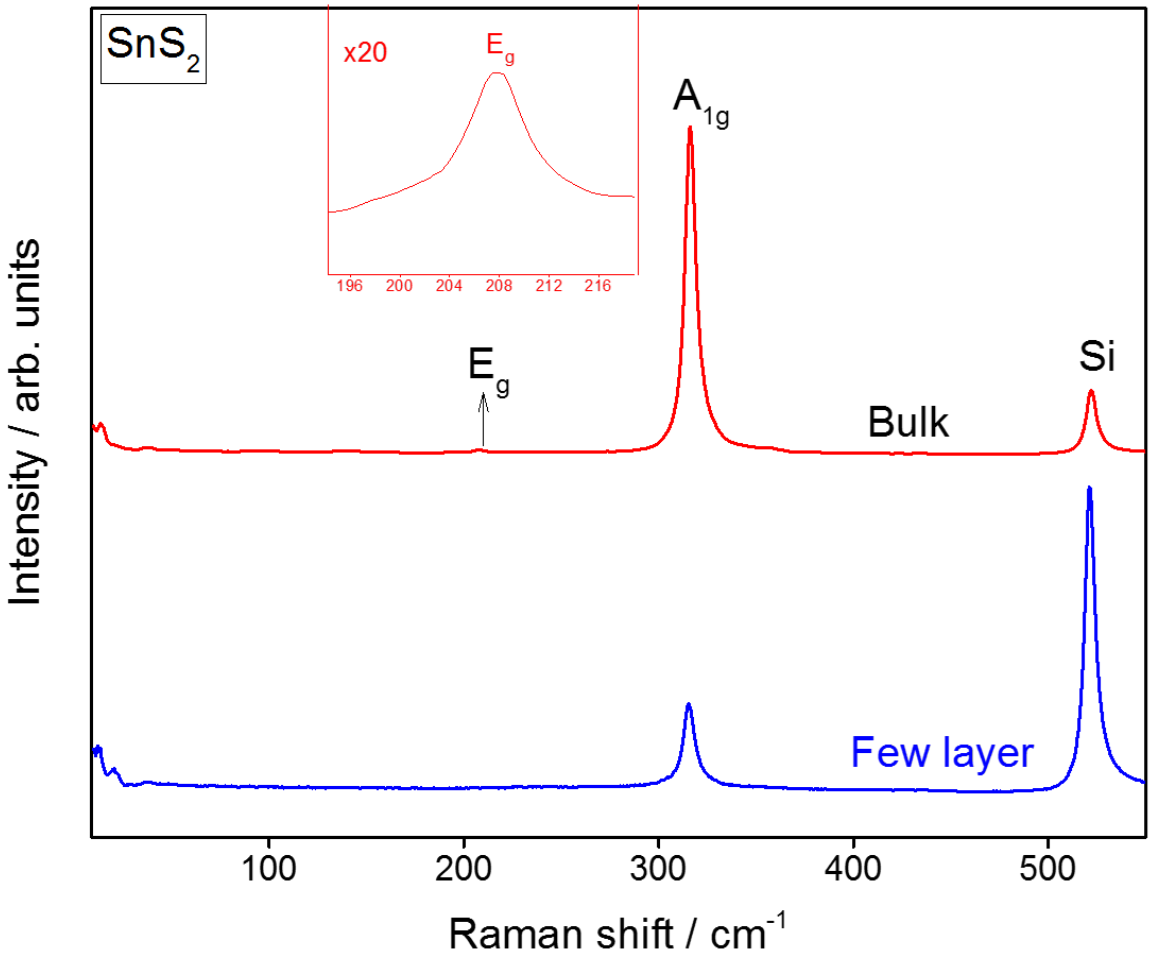

Figure 4.14. The Raman spectra of bulk and few layer form of SnS_2.

4.3.4. $MoTe_2$

Molybdenum dichalcogenides ($MoTe_2$), as a member of MX_2 type TMDs materials, exhibits interesting physical, electronic, chemical features that are useful to be utilized for the applications of electronics, spintronics, valleytronics, optics, and catalysis [35, 36].

$MoTe_2$ is crystallized in different crystal structures that results different characteristics depend on the polytype. The two common polytype of $MoTe_2$ are 2H (trigonal prismatic) and 1T (octahedral) as in the case of most TMDs [37]. Herein, we study the few layer 2H type $MoTe_2$ crystals. **Figure 4.15** displays the optical microscopy image of $MoTe_2$ crystal micromechanically exfoliated on SiO_2/Si as thin and thick layers can be distinguished by optical contrast.

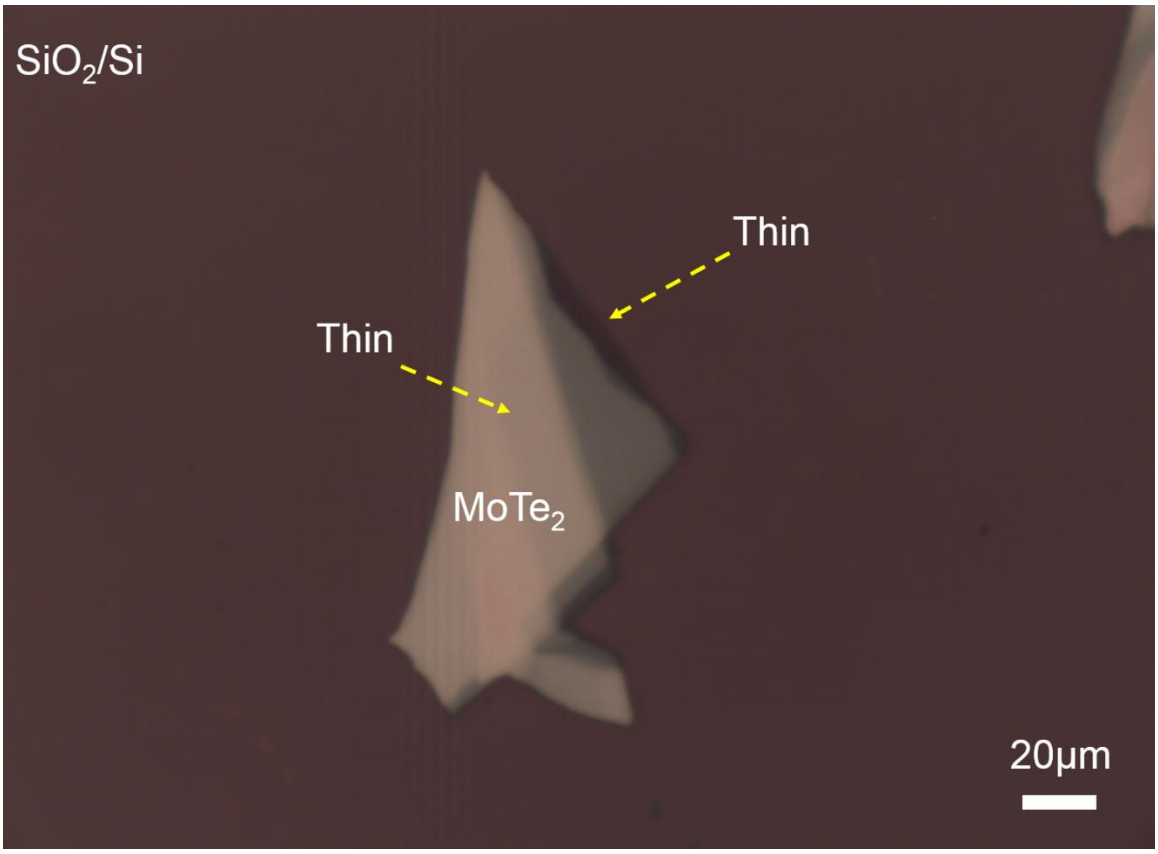

Figure 4.15. The Raman spectra of $MoTe_2$.

The 2H $MoTe_2$ has D_{6h} group symmetry and its phonon modes are given by irreducible representation of $\Gamma = A_{1g} + 2A_{2u} + 2B_{2g} + E_{1g} + 2E_{1u} + E_{2u} + B_{1u} + 2E_{2g}$ [38].

The Raman active modes are A_{1g}, E_{1g}, E^1_{2g}, and E^2_{2g}. The E^1_{1u}, E^2_{1u}, A^1_{2u}, and A^2_{2u} are infrared active modes. The other modes are optically inactive. The number of phonon modes reduces with reducing symmetry for few layers $MoTe_2$ crystals [39-42].

Figure 4.16 represents the Raman spectra taken thin and thick regions of $MoTe_2$. The E^1_{2g} mode defined as the in plane vibrations between Molybdenum and Tellurium atoms, and it is located at the Raman wavenumber of 234.7 cm^{-1} and 234.2 cm^{-1} for thin and thick regions, respectively. Small amount of red shift (0.5 cm^{-1}) is observed with increasing thickness. The out of plane A_{1g} peak is observed at the Raman wavenumber of 172.5 cm^{-1} and 173.5 cm^{-1} for thin and thick regions, respectively. The A_{1g} mode experiences a blue shift (1 cm^{-1}) with increasing thickness. The optically inactive out of plane B^1_{2g} mode is located at the Raman wavenumber of 290.8 and 290.3 for thin and thick regions, respectively. The B^1_{2g} mode is bulk inactive, is also not observed in monolayer form, however it exist only in atomically thin $MoTe_2$ as few layer form, hence it results the maximum Raman mode intensity in bilayer form. The intensity ratio of Raman B^1_{2g} and E^1_{2g} modes provides thickness information of the few layer $MoTe_2$. We calculated the intensity ratio (I (B^1_{2g}) / I (E^1_{2g})) of Raman modes of thin flake $MoTe_2$ of as 0.5, which corresponds to bilayer [43]. The second order Raman mode 2TA(M) is observed at the Raman wavenumber of 138.5 cm^{-1}, and 141 cm^{-1} for thin and thick regions, respectively. There is a blue shift (2.5 cm^{-1}) of the Raman spectra with increasing thickness of $MoTe_2$. The 2TA(M) mode appears as a result of second order resonant Raman scattering process at the M symmetry point of the Brillouin zone, where TA refers to the transverse acoustic phonon. The infrared active in plane mode E_{2u} is located at the Raman wavenumber of

118.8 cm^{-1} for thin region, but it is absent for the thick region. The low frequency interlayer shear and breathing modes are observed in the Raman spectra taken from thick region of $MoTe_2$, but these modes are not exist for thin regions. The interlayer shear mode E^2_{2g} is located at the Raman wavenumber of 26.7 cm^{-1}, while the interlayer breathing mode is at 35.8 cm^{-1}. Another way to decide the bilayer $MoTe_2$ from the Raman spectra is to compare the intensity of $A_{1g}$and B^1_{2g} modes, since the B^1_{2g} mode is stronger than A_{1g} mode only in bilayer form [44].

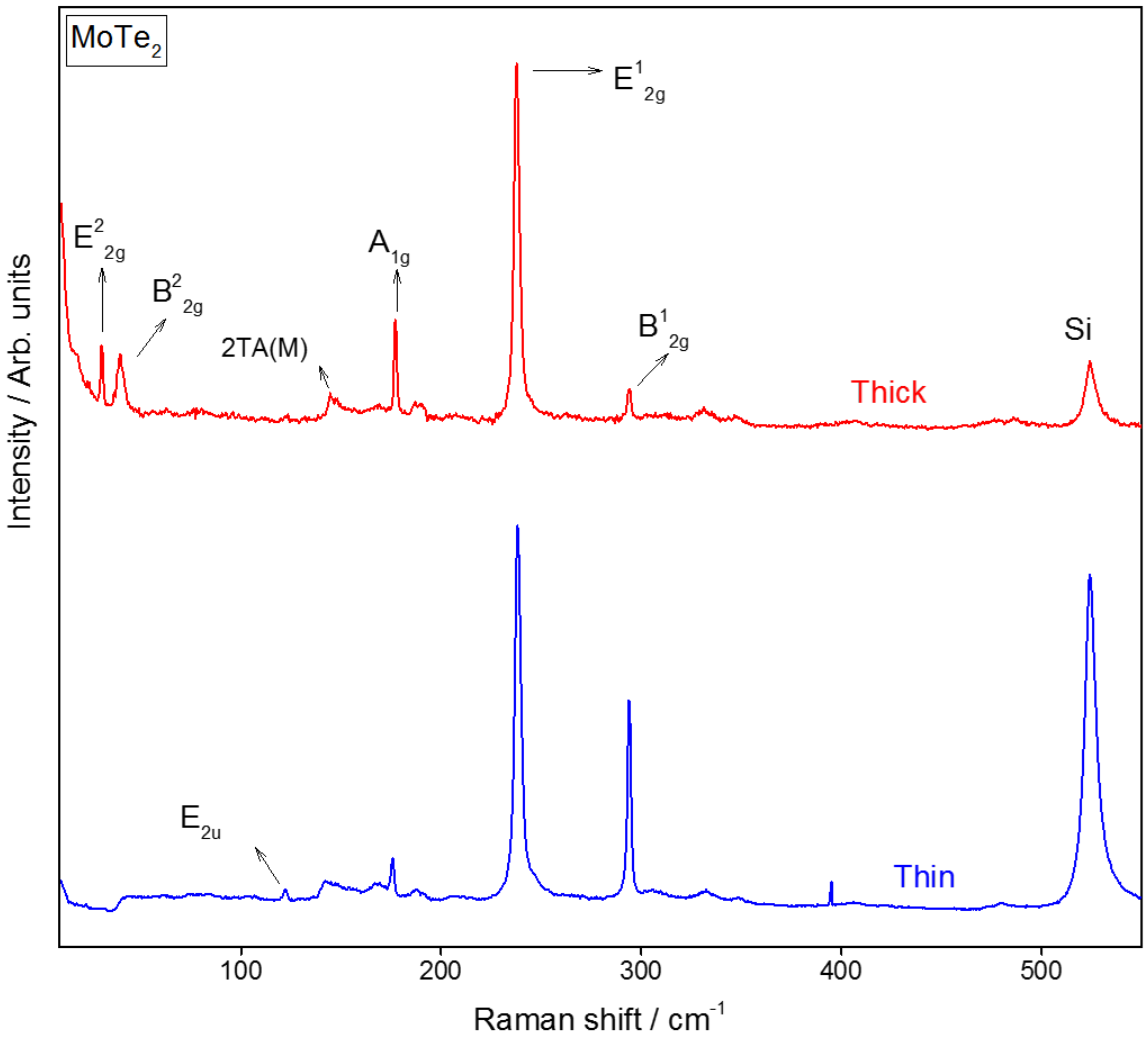

Figure 4.16. The Raman spectra taken from the thin and thick regions of $MoTe_2$.

4.3.5. $SnSe_2$ / WSe_2

We built the 1T-$SnSe_2$/2H-WSe_2 heterostructures, which are one of the potential candidates for new generation electronics application of tunnel field effect transistor (TFET) [45-47]. **Figure 4.17** presents the optical microscopy image of vertically stacked $SnSe_2$ / WSe_2 heterostructure on SiO_2/Si substrate. The $SnSe_2$ sits on the substrate, while WSe2 was transferred on top of $SnSe_2$.

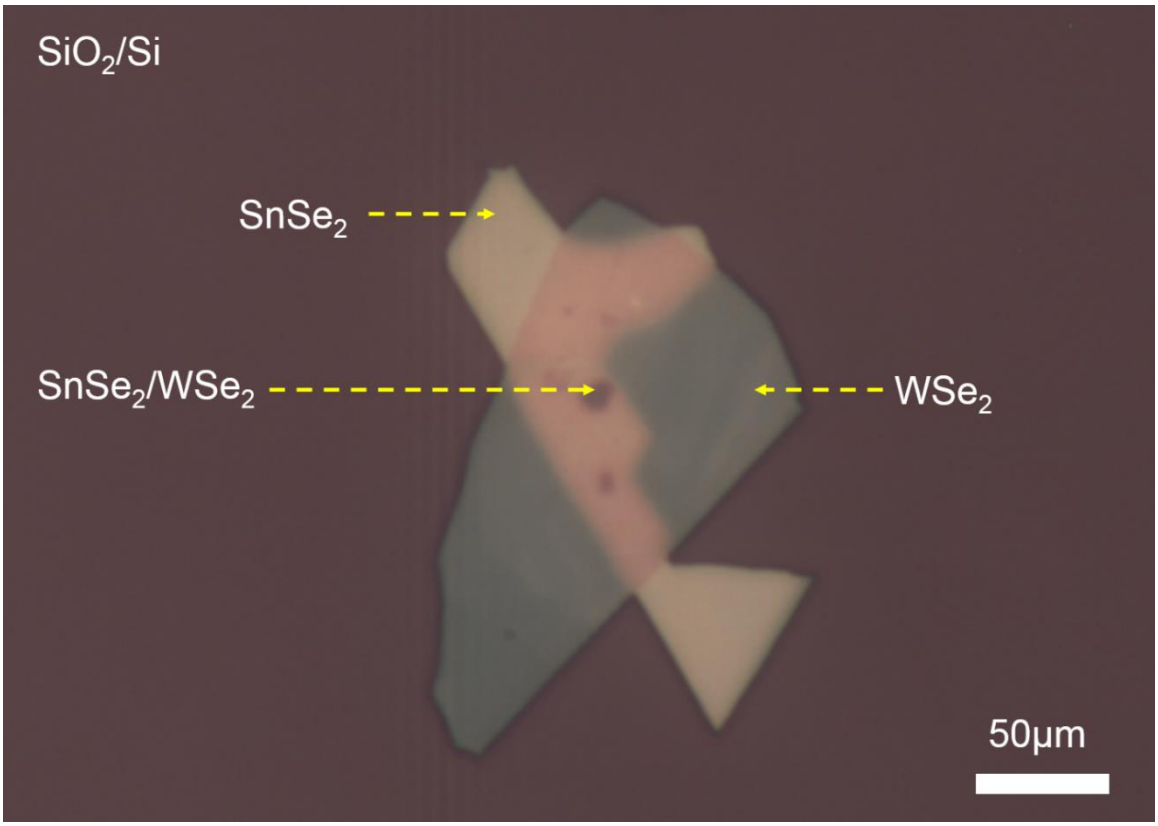

Figure 4.17. Optical microscopy image of $SnSe_2$/WSe_2 heterostructure on SiO_2/Si substrate.

The vertically stacked $SnSe_2/WSe_2$ heterostructures have been studied by Raman and photoluminescence spectroscopy [48, 49]. The Raman spectra (**Figure 4.18**), taken from three different components as $SnSe_2$, WSe_2, and junction, confirms that the vertically stacked heterostructure was achieved. The Raman spectra reveals typical first and second order modes of both $SnSe_2$ and WSe_2. The existence of second order resonant Raman modes confirms that the few layers of heterostructures. We observed a slight blue shift (0.5 cm^{-1}) on the in plane E^1_g mode of $SnSe_2$ after heterostructure formation. Blue shift of E_{1g} peak indicates the stiffening of the in plane bonds, and this same effect of blue shift was observed with the increasing thickness of bare $SnSe_2$. The in plane shear mode E^2_g mode was suppressed at the junction. We did not see any other dramatic shift on the other modes, and it is noteworthy that we did not see any shift on the any modes of the WSe_2.

The **figure 4.19** presents the PL spectra of multilayer (**a**) and monolayer (**b**) WSe_2. PL spectra reveals that indirect to direct band gap transition from multilayer to monolayer. The PL intensity is significantly higher for monolayer WSe_2 than that of multilayer, and this is the trend for all TMDs. The peak labeled as A in the spectra represent the direct band gap at K point of the Brillouin zone. The weak peak labeled as B in the spectra is assigned as the direct band gap transition at K point of the Brillouin zone. The difference on energy between B and A peaks (2.06eV -1.59 eV=0.45 eV) is stem from the spin orbit splitting at the valence band. The peak labeled as I in the spectra is assigned as the indirect band gap transition, and it disappears for monolayer WSe_2. The direct band gap is read as 1.65 eV for monolayer WSe_2 [50-58].

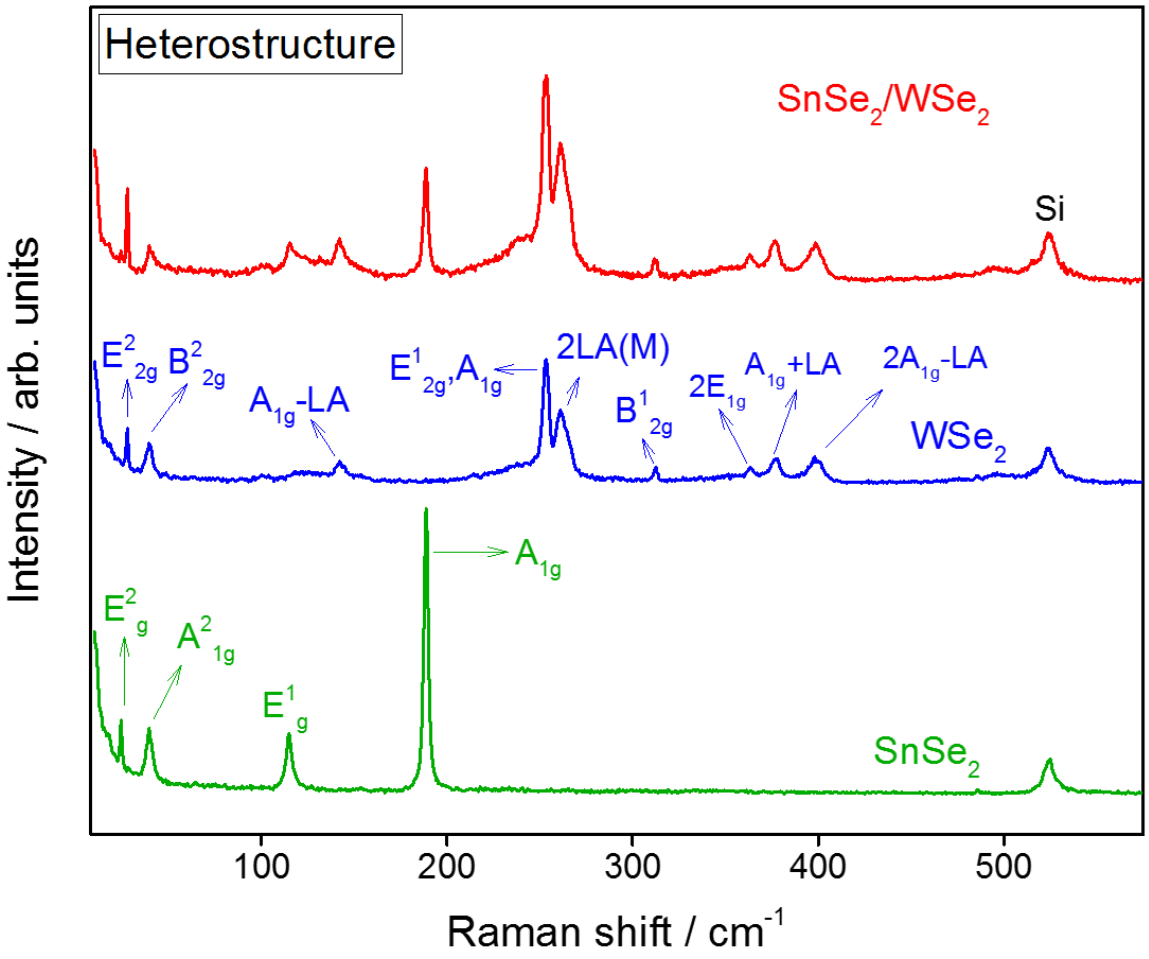

Figure 4.18. Raman spectra of the heterostructure of $SnSe_2/WSe_2$.

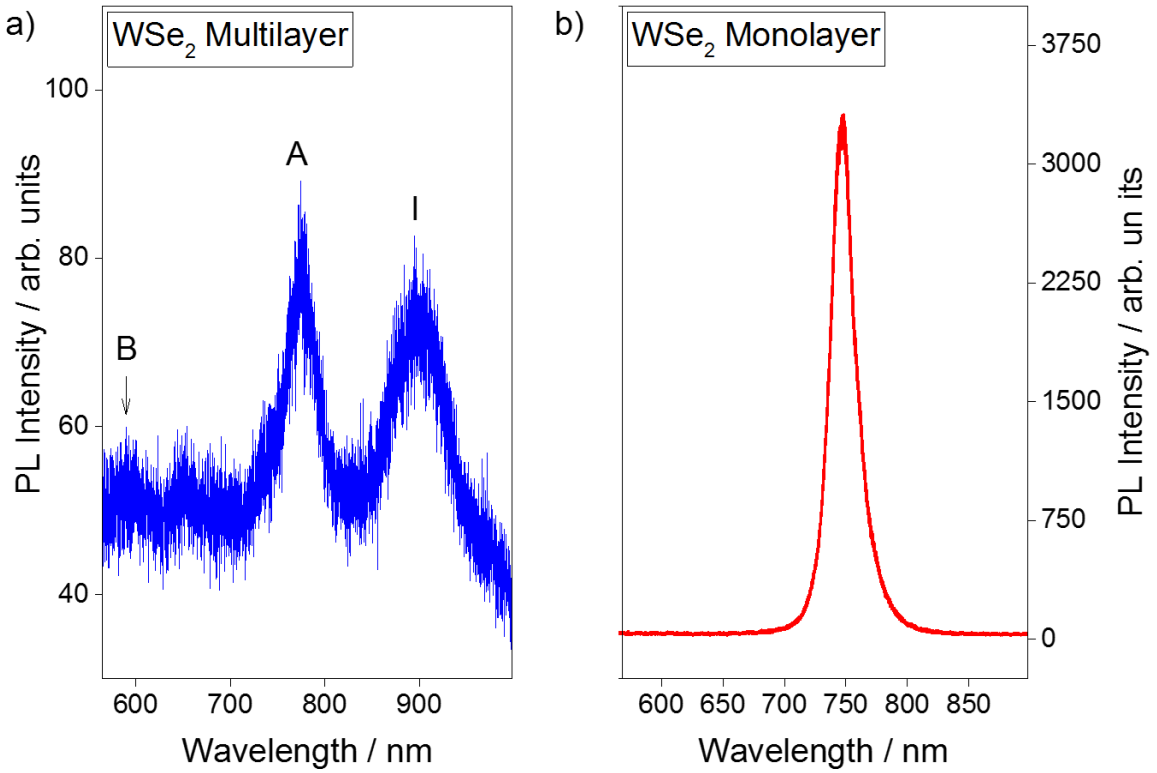

Figure 4.19. PL spectra of multilayer and monolayer WSe_2.

The **figure 4.20** presents the Photoluminescence (PL) spectra taken from different regions from the heterostructure. The PL spectra of WSe_2 side indicates that the 3 layers crsytals according to literature. $SnSe_2$ is known with its weak PL behavior, hence we track the PL behavior of WSe_2 and $SnSe_2/WSe_2$ heterojunction. The PL spectra, taken from WSe_2 and junction, reveals significant difference. We calculated the difference between B and A peaks as 0.42 eV and 0.51 eV for WSe_2 and junction, respectively.

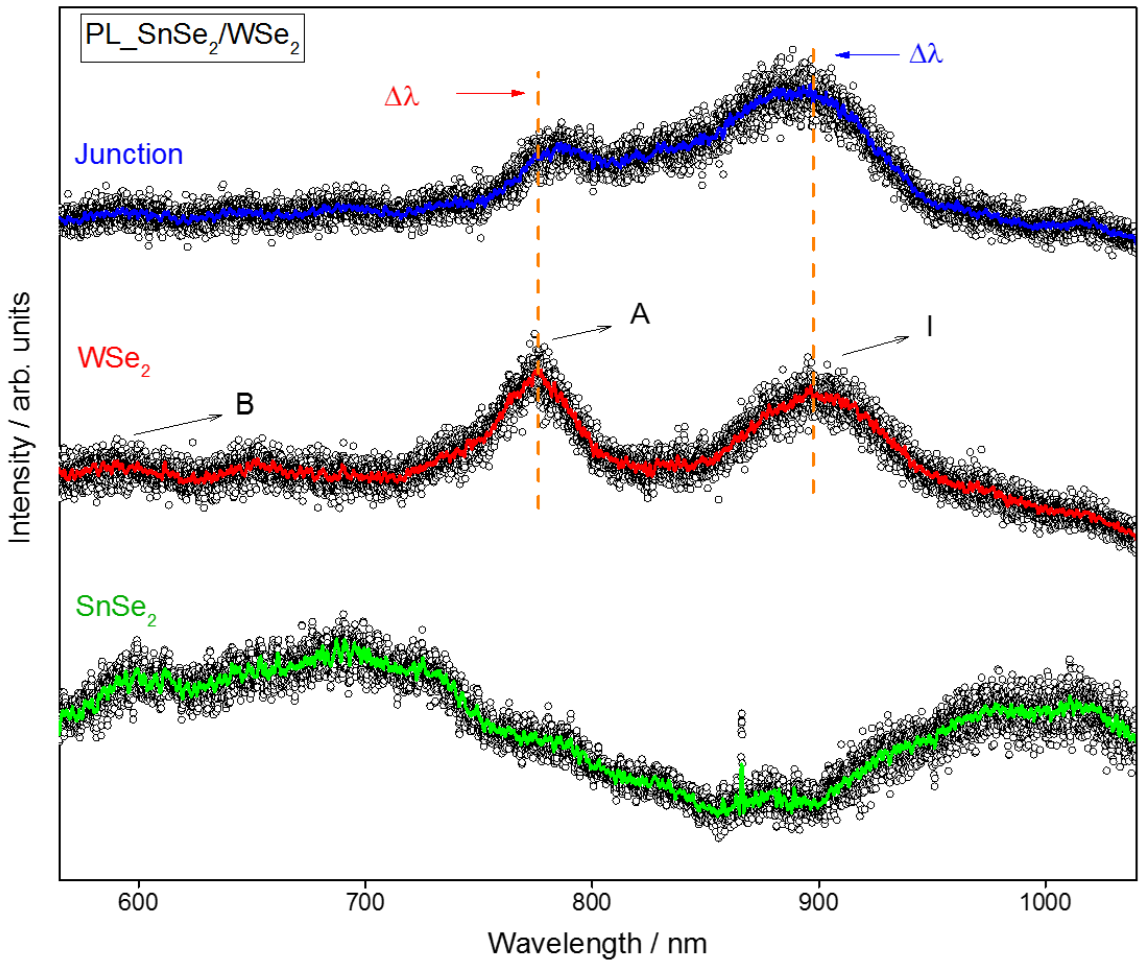

Figure 4.20. The PL spectra taken from WSe_2, $SnSe_2$, and the junction of the heterostructure.

4.3.6. $SnS_2/MoTe_2$

The **figure 4.21** presents the optical microscopy image of $SnS_2/MoTe_2$ heterostructure, which has the great potential of applications of electronics thanks to its broken band gap at junction [59]. The SnS_2 is located at the bottom, while $MoTe_2$ is transferred onto SnS_2. The optical contrast provides visible differentiation of the combination of different materials and thickness.

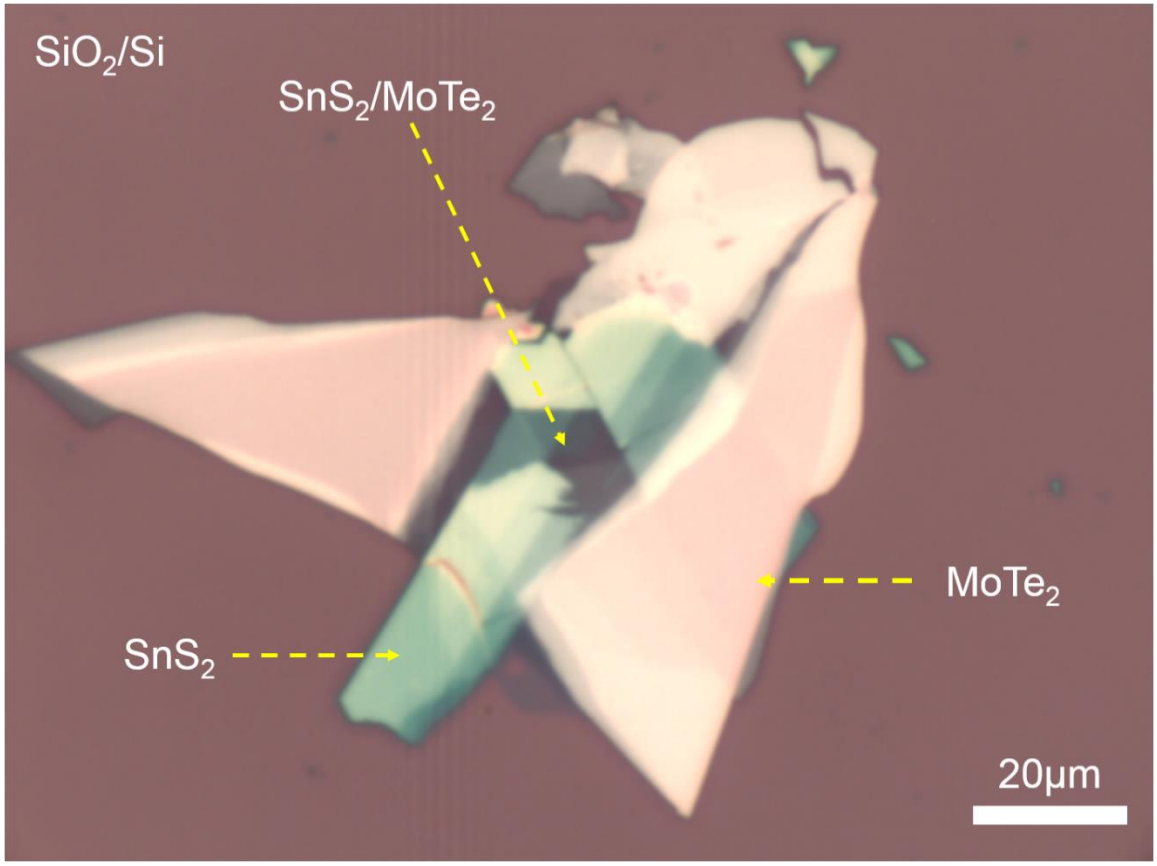

Figure 4.21. Optical microscopy image of $SnS_2/MoTe_2$ on the SiO_2/Si substrate.

Figure 4.22 presents the Raman spectra taken from three different components of the heterostructure as SnS_2, $MoTe_2$, and junction. From the observation of second order resonant Raman modes of $MoTe_2$ and disappearance of E_g mode of SnS_2, it is likely to state we have achieved few layers of heterostructure. The out of plane A_{1g} mode of SnS_2 has been experienced a red shift (1.3 cm^{-1}) at junction. This implies that softening of the out of plane bonds due to interaction of van der Waals force. The out of plane breathing mode

B^2_{2g} has experienced a blue shift (2.7 cm^{-1}), and this implies stiffening of the out of plane breathing mode.

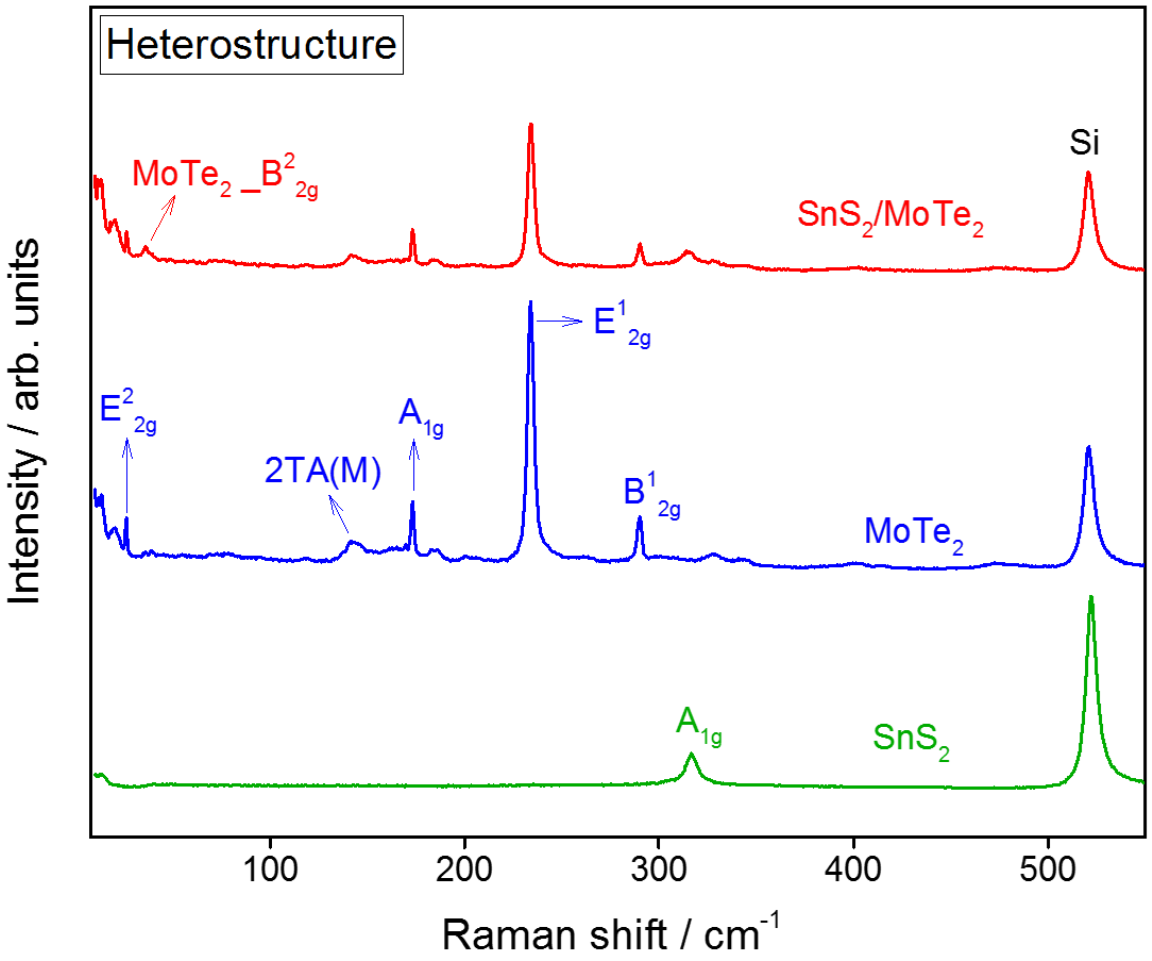

Figure 4.22. Raman spectra of $SnS_2/MoTe_2$ heterostructures.

Figure 4.23 and **Figure 4.24** present the polarized Raman mapping of the selected region in the center and corresponding analysis of the heterostructure. The bright green region in the mapping represents bare $MoTe_2$, the bright blue region represents bare SnS_2, and the darker blue region represents the junction.

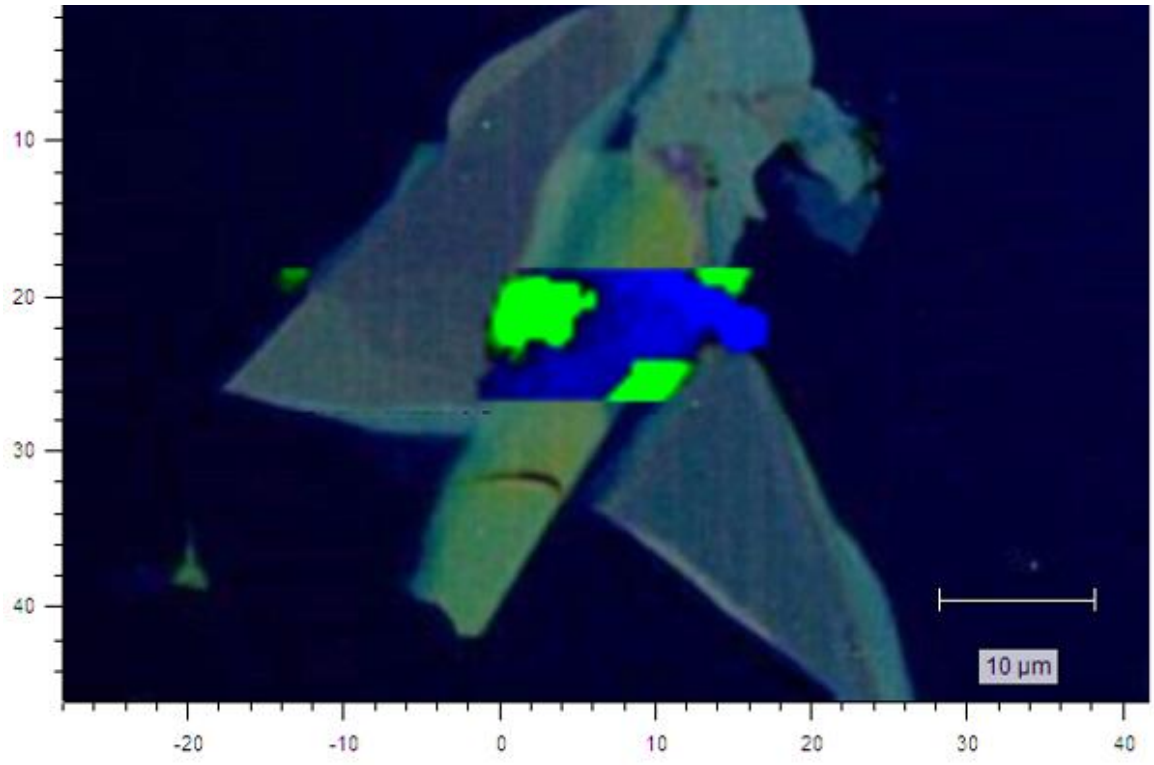

Figure 4.23. The polarized Raman mapping of SnS_2/$MoTe_2$ heterostructures.

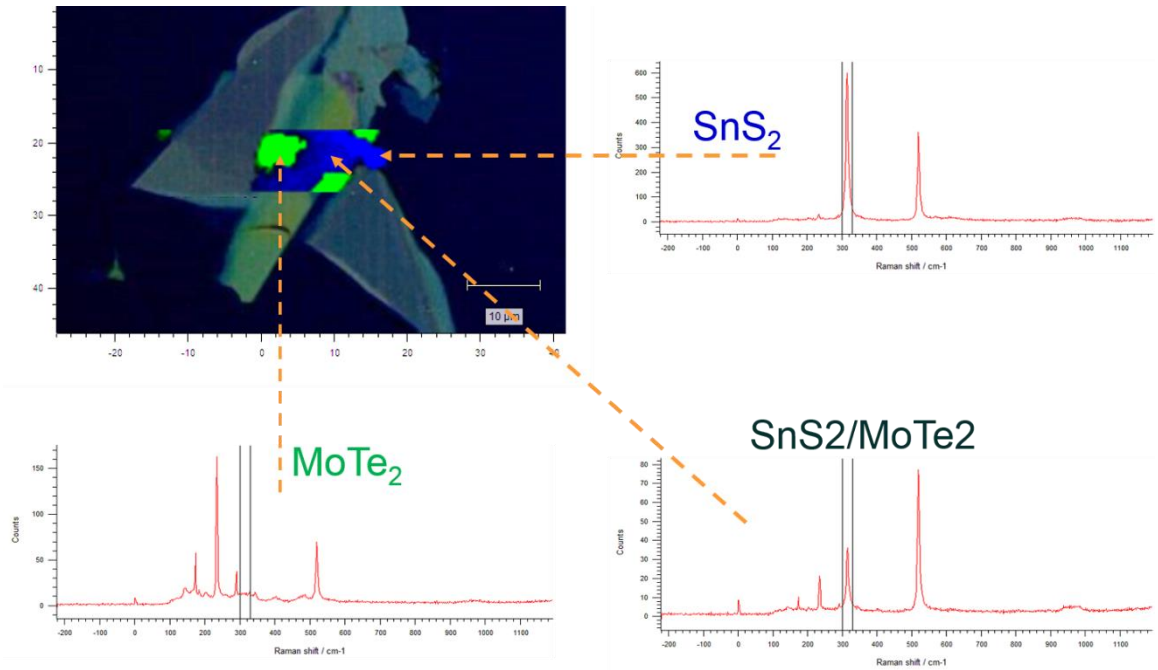

Figure 4.24. The analysis of polarized Raman mapping of SnS_2/$MoTe_2$ heterostructures.

4.4. Conclusions

The second order resonant Raman scattering investigation have been studied on metal and transition metal dichalcogenides and heterostructures. The second order resonant Raman process has been demonstrated that to be an effective characterization method on transition metal dichalcogenides. The second order resonant Raman scattering is an easy and powerful method to identify the structural characteristics, but also not limited to analyze the phonon behavior of these semiconductor materials. The thickness identification of few layer WSe_2 and $MoTe_2$ can be effectively conducted by resonant Raman process thanks to variety of phonon modes that are only appear in excitation by the proper wavelength of the interacting photon.

4.5. References for chapter 4

[1] X. Zhang, Q-H. Tan, J-B. Wu, W. Shi, and P-H. Tan: *Review on the Raman spectroscopy of different types of layered materials*. Nanoscale **8**, no. 12 (2016), 6435-6450.

[2] Y. Ma, Y. Dai, M. Guo, C. Niu, J. Lu, and B. Huang*: Electronic and magnetic properties of perfect, vacancy-doped, and nonmetal adsorbed MoSe 2, MoTe 2 and WS 2 monolayers*. Physical Chemistry Chemical Physics **13**, no. 34 (2011), 15546-15553.

[3] X. Zhang, X-F. Qiao, W. Shi, J-B. Wu, D-S. Jiang, and P-H. Tan: *Phonon and Raman scattering of two-dimensional transition metal dichalcogenides from monolayer, multilayer to bulk material*. Chemical Society Reviews **44**, no. 9 (2015), 2757-2785.

[4] A.C. Ferrari and D.M. Basko: *Raman spectroscopy as a versatile tool for studying the properties of graphene.* Nature nanotechnology **8**, no. 4 (2013), 235-246.

[5] R.L. McCreery: *Raman spectroscopy for chemical analysis*. Vol. **225**. John Wiley & Sons, (2005).

[6] L.P. Bouckaert, R. Smoluchowski, and E. Wigner: *Theory of Brillouin zones and symmetry properties of wave functions in crystals*. Physical Review **50**, no. 1 (1936), 58.

[7] J.P. Elliott, and P.G. Dawber: *Symmetry in Physics, Volume* **1** *and* **2**. Macmillan, (1979).

[8] D.L. Rousseau, R.P. Bauman, and S.P.S. Porto: *Normal mode determination in crystals*. Journal of Raman Spectroscopy **10**, no. 1 (1981), 253-290.

[9] S. Bhagavantam and T. Venkatarayudu: *Raman effect in relation to crystal structure*. Proceedings Mathematical Sciences **9**, no. 3 (1939), 224-258.

[10] A.A. Puretzky, L. Liang, X. Li, K. Xiao, K. Wang, M.M. Samani, L. Basile, J.C. Idribo, B.G. Sumpter, B. Meunier, and D.B Geohegan: *Low-frequency Raman fingerprints of two-dimensional metal dichalcogenide layer stacking configurations*. ACS nano **9**, no. 6 (2015), 6333-6342.

[11] R. Saito, A. Jorio, A.G.S. Filho, G. Dresselhaus, M.S. Dresselhaus, and M.A. Pimenta: *Probing phonon dispersion relations of graphite by double resonance Raman scattering*. Physical review letters **88**, no. 2 (2001), 027401.

[12] A.A. Mitioglu, P. Plochocka, G. Deligeorgis, S. Anghel, L. Kulyuk, and D.K. Maude: *Second-order resonant Raman scattering in single-layer tungsten disulfide WS 2*. Physical Review B **89**, no. 24 (2014), 245442.

[13] E. del Corro, H. Terrones, A. Elias, C. Fantini, S. Feng, M.A. Nguyen, T.E. Mallouk, M. Terrones, and M.A. Pimenta: *Excited excitonic states in 1L, 2L, 3L, and bulk WSe2 observed by resonant Raman spectroscopy*. ACS nano **8**, 9 (2014), pp.9629-9635.

[14] H. Sahin, S. Tongay, S. Horzum, W. Fan, J. Zhou, J. Li, J. Wu, and F. M. Peeters: *Anomalous Raman spectra and thickness-dependent electronic properties of WSe 2*. Physical Review B **87**, no. 16 (2013), 165409.

[15] S.B. Desai, G. Seol, J.S. Kang, H. Fang, C. Battaglia, R. Kapadia, J.W. Ager, J. Guo, and A. Javey: *Strain-induced indirect to direct bandgap transition in multilayer WSe2*. Nano letters **14**, no. 8 (2014), 4592-4597.

[16] W. Shi, M-L. Lin, Q-H. Tan, X-F. Qiao, J. Zhang, and P-H. Tan: *Raman and photoluminescence spectra of two-dimensional nanocrystallites of monolayer WS2 and WSe2*. 2D Materials **3**, no. 2 (2016), 025016.

[17] T. Minagawa: *Common polytypes of SnS2 and SnSe2*. Journal of the Physical Society of Japan **49**, no. 6 (1980), 2317-2318.

[18] B. Pałosz, S. Gierlotka, and F. Levy: *Polytypism of SnSe2 crystals grown by chemical* transport structures of six large-period polytypes of SnSe2. Acta Crystallographica Section C: Crystal Structure Communications **41**, no. 10 (1985), 1404-1406.

[19] B.D. Tracy, X. Li, X. Liu, J. Furdyna, M. Dobrowolska, and D.J. Smith: *Characterization of structural defects in SnSe 2 thin films grown by molecular beam epitaxy on GaAs (111) B substrates*. Journal of Crystal Growth **453** (2016), 58-64.

[20] P. Yu, X. Yu, W. Lu, H. Lin, L. Sun, K. Du, F. Liu, W. Fu, Q. Zeng, Z. Shen, C. Jin, Q.J. Wang, and Z. Liu: *Fast photoresponse from 1T tin diselenide atomic layers*. Advanced Functional Materials **26**, no. 1 (2016), 137-145.

[21] J.M. Gonzalez and I.I. Oleynik: *Layer-dependent properties of SnS 2 and SnSe 2 two-dimensional materials*. Physical Review B **94**, no. 12 (2016), 125443.

[22] W. Zhou, Z. Yu, H. Song, R. Fang, Z. Wu, L. Li, Z. Ni, W. Ren, L. Wang, and S. Ruan: *Lattice dynamics in monolayer and few-layer SnSe 2*. Physical Review B **96**, no. 3 (2017), 035401.

[23] A.J. Smith, P.E. Meek, and W.Y. Liang: *Raman scattering studies of SnS2 and SnSe2*. Journal of Physics C: Solid State Physics **10**, no. 8 (1977), 1321.

[24] T.Y. Jeong, B.M. Jin, S.H. Rhim, L. Debbichi, J. Park, Y.D. Jang, H.R. Lee, D-H. Chae, D. Lee, Y-H. Kim, S. Jung, and K.J. Yee: *Coherent lattice vibrations in mono-and few-layer WSe2*. ACS nano **10**, no. 5 (2016), 5560-5566.

[25] W. Zhao, Z. Ghorannevis, K.K. Amara, J.R. Pang, M. Toh, X. Zhang, C. Kloc, P.H. Tan, and G. Eda: *Lattice dynamics in mono-and few-layer sheets of WS 2 and WSe 2*. Nanoscale **5**, no. 20 (2013), 9677-9683.

[26] H. Li, G. Lu, Y. Wang, Z. Yin, C. Cong, Q. He, L. Wang, F. Ding, T. Yu, and H. Zhang: *Mechanical Exfoliation and Characterization of Single-and Few-Layer Nanosheets of WSe2, TaS2, and TaSe2*. Small **9**, no. 11 (2013), 1974-1981.

[27] Y. Zhao, X. Luo, H. Li, J. Zhang, P.T. Araujo, C.K. Gan, J. Wu, H. Zhang, S.Y. Quek, M.S. Dresselhaus, and Q. Xiong: *Interlayer breathing and shear modes in few-trilayer MoS2 and WSe2*. Nano letters **13**, no. 3 (2013), 1007-1015.

[28] H. Terrones, E.D. Corro, S. Feng, J.M. Poumirol, D. Rhodes, D. Smirnov, N.R. Pradhan, Z. Lin, M.A.T. Nguyen, A.L. Elias, T.E. Mallouk, L. Balicas, M.A. Pimenta, and M. Terrones: *New first order Raman-active modes in few layered transition metal dichalcogenides*. Scientific reports **4** (2014).

[29] E.D. Corro, A. Botello-Méndez, Y. Gillet, A.L. Elias, H. Terrones, S. Feng, C. Fantini, D. Rhodes, N. Pradhan, L. Balicas, X. Gonze, J.-C. Charlier, M. Terrones, and M.A. Pimenta: *Atypical Exciton–Phonon Interactions in WS2 and WSe2 Monolayers Revealed by Resonance Raman Spectroscopy*. Nano letters **16**, no. 4 (2016), 2363-2368.

[30] H. Zeng, G-B. Liu, J. Dai, Y. Yan, B. Zhu, R. He, L. Xie, S. Xu, X. Chen, W. Yao, and X. Cui: *Optical signature of symmetry variations and spin-valley coupling in atomically thin tungsten dichalcogenides*. Scientific reports **3** (2013).

[31] Y. Zhang, M.M. Ugeda, C. Jin, S-F. Shi, A.J. Bradley, A. Martín-Recio, H. Ryu, J. Kim, S. Tang, Y. Kim, B. Zhou, C. Hwang, Y. Chen, F. Wang, M.F. Crommie, Z. Hussain, Z-X. Shen, and S-K. Mo: *Electronic structure, surface doping, and optical response in epitaxial WSe2 thin films*. Nano letters **16**, no. 4 (2016), 2485-2491.

[32] W. Zhao, Z. Ghorannevis, L. Chu, M. Toh, C. Kloc, P-H. Tan, and G. Eda: *Evolution of electronic structure in atomically thin sheets of WS2 and WSe2*. ACS nano **7**, no. 1 (2012), 791-797.

[33] S. Nakashima, H. Katahama, and A. Mitsuishi: *The effect of polytypism on the vibrational properties of SnS2*. Physica B+ C **105**, no. 1-3 (1981), 343-346.

[34] A.N. Utyuzh, Y.A. Timofeev, and G. N. Stepanov: *Effect of pressure on raman spectra of SnS 2 single crystals*. Physics of the Solid State **52**, no. 2 (2010), 352-356.

[35] L. Zhou, K. Xu, A. Zubair, A.D. Liao, W. Fang, F. Ouyang, Y-H. Lee, K. Ueno, R. Saito, T. Palacios, J. Kong, and M.S. Dresselhaus: *Large-area synthesis of high-quality uniform few-layer MoTe2*. Journal of the American Chemical Society **137**, no. 37 (2015), 11892-11895.

[36] C.H. Naylor, W.M. Parkin, J. Ping, Z. Gao, Y.R. Zhou, Y. Kim, F. Streller , R.W. Carpick, A.M. Rappe, M. Drndic, J.M. Kikkawa, and A.T.C. Johnson: *Monolayer Single-Crystal 1T'-MoTe2 Grown by Chemical Vapor Deposition Exhibits Weak Antilocalization Effect*. Nano letters **16**, no. 7 (2016), 4297-4304.

[37] M. Kan, H.G. Nam, Y.H. Lee, and Q. Sun: *Phase stability and Raman vibration of the molybdenum ditelluride (MoTe 2) monolayer*. Physical Chemistry Chemical Physics **17**, no. 22 (2015), 14866-14871.

[38] M. Grzeszczyk, K. Gołasa, M. Zinkiewicz, K. Nogajewski, M. R. Molas, M. Potemski, A. Wysmołek, and A. Babiński: *Raman scattering of few-layers MoTe2*. 2D Materials **3**, no. 2 (2016), 025010.

[39] D.H. Keum, S. Cho, J.H. Kim, D-H. Choe, H-J. Sung, M. Kan, H. Kang, J-Y. Hwang, S-W. Kim, H. Yang, K.J. Chang, and Y.H. Lee: *Bandgap opening in few-layered monoclinic MoTe2*. Nature Physics **11**, no. 6 (2015), 482.

[40] T. Goldstein, S-Y. Chen, J. Tong, D. Xiao, A. Ramasubramaniam, and J. Yan: *Raman scattering and anomalous Stokes–anti-Stokes ratio in MoTe2 atomic layers*. Scientific reports **6** (2016), 28024.

[41] R. Beams, L.G. Cançado, S. Krylyuk, I. Kalish, B. Kalanyan, A.K. Singh, K. Choudhary, A. Bruma, P.M. Vora, F. Tavazza, et al. "Characterization of Few-Layer 1T′

MoTe2 by Polarization-Resolved Second Harmonic Generation and Raman Scattering." *ACS nano* 10, no. 10 (2016): 9626-9636.

[42] T. Goldstein, S-Y. Chen, J. Tong, D. Xiao, A. Ramasubramaniam, and J. Yan: *Raman scattering and anomalous Stokes–anti-Stokes ratio in MoTe2 atomic layers*. Scientific reports **6** (2016), 28024.

[43] M. Yamamoto, S.T. Wang, M. Ni, Y-F. Lin, S-L. Li, S. Aikawa, W-B. Jian, K. Ueno, K. Wakabayashi, and K. Tsukagoshi: *Strong enhancement of Raman scattering from a bulk-inactive vibrational mode in few-layer MoTe2*. ACS nano **8**, no. 4 (2014), 3895-3903.

[44] C. Ruppert, O.B. Aslan, and T.F. Heinz. *Optical properties and band gap of single- and few-layer MoTe2 crystals*. Nano letters **14**, no. 11 (2014), 6231-6236.

[45] K.E. Aretouli, D. Tsoutsou, P. Tsipas, J. Marquez-Velasco, S.A. Giamini, N. Kelaidis, V. Psycharis, and A. Dimoulas. *Epitaxial 2D SnSe2/2D WSe2 van der Waals Heterostructures*. ACS applied materials & interfaces **8**, no. 35 (2016), 23222-23229.

[46] M.O. Li, David Esseni, J.J. Nahas, D. Jena, and H.G. Xing. *Two-dimensional heterojunction interlayer tunneling field effect transistors (thin-tfets)*. IEEE Journal of the Electron Devices Society **3**, no. 3 (2015), 200-207.

[47] T. Roy, M. Tosun, X. Cao, H. Fang, D-H. Lien, P. Zhao, Y-Z. Chen, Y-L. Chueh, J. Guo, and A. Javey. *Dual-gated MoS2/WSe2 van der Waals tunnel diodes and transistors*. Acs Nano **9**, no. 2 (2015), 2071-2079.

[48] M. Zhao, M. Liu, Y. Dong, C. Zou, K. Yang, Y. Yang, L. Zhang, and S. Huang: *Epitaxial growth of two-dimensional SnSe 2/MoS 2 misfit heterostructures*. Journal of Materials Chemistry C **4**, no. 43 (2016), 10215-10222.

[49] X. Zhou, N. Zhou, C. Li, H. Song, Q. Zhang, X. Hu, L. Gan, H. Li, J. Lü, J. Luo, J. Xiong, and T. Zhai: *Vertical heterostructures based on SnSe2/MoS2 for high performance photodetectors.* 2D Materials **4**, no. 2 (2017), 025048.

[50] Y. He, Y. Yang, Z. Zhang, Y. Gong, W. Zhou, Z. Hu, G. Ye, X. Zhang, E. Bianco, S. Lei, Z. Jin, X. Zou, Y. Yang, Y. Zhang, E. Xie, J Lou, B. Yakobson, R. Vajtai, B. Li, and P. Ajayan: *Strain-Induced Electronic Structure Changes in Stacked van der Waals Heterostructures*. Nano letters **16**, no. 5 (2016), 3314-3320.

[51] K. Xu, Z. Wang, X. Du, M. Safdar, C. Jiang, and J. He: *Atomic-layer triangular WSe2 sheets: synthesis and layer-dependent photoluminescence property*. Nanotechnology **24**, no. 46 (2013), 465705.

[52] J.M. Riley, F. Mazzola, M. Dendzik, M. Michiardi, T. Takayama, L. Bawden, C. Granerod, M. Leandersson, T. Balasubramanian, M. Hoesch, T.K. Kim, H. Takagi, W. Meevasana, P. Hofmann, M.S. Bahramy, j.W. Wells, P.D.C. King: *Direct observation of spin-polarized bulk bands in an inversion-symmetric semiconductor.* Nat. Phys. **10,** no. 11 (2014), 835-839.

[53] P-C. Yeh, W. Jin, N. Zaki, D. Zhang, J.T. Liou, J.T. Sadowski, A.Al-Mahboob, J.I. Dadap, I.P. Herman, P. Sutter, R.M. Osgood, Jr.: *Layer-dependent electronic structure of an atomically heavy two-dimensional dichalcogenide*. Physical Review B **91**, no. 4 (2015), 041407.

[54] C.H. Lui, Z. Ye, C. Ji, K-C. Chiu, C-T. Chou, T.I. Andersen, C. Means-Shively, H.

Anderson, J.M. Wu, T. Kidd, Y-H. Lee, and R. He: *Observation of interlayer phonon modes in van der Waals heterostructures*. Physical Review B **91**, no. 16 (2015), 165403.

[55] P. Rivera, J.R. Schaibley, A.M. Jones, J.S. Ross, S. Wu, G. Aivazian, P. Klement, K. Seyler, G. Clark, N.J. Ghimire, J. Yan, D.G. Mandrus, W. Yao, and X. Xu: *Observation of long-lived interlayer excitons in monolayer MoSe2-WSe2 heterostructures*. Nature communications **6,** (2015), 6242.

[56] H. Zeng, G-B. Liu, J. Dai, Y. Yan, B. Zhu, R. He, L. Xie, S. Xu, X. Chen, W. Yao, and X. Cui: *Optical signature of symmetry variations and spin-valley coupling in atomically thin tungsten dichalcogenides*. Scientific reports **3** (2013).

[57] T. Yan, X. Qiao, X. Liu, P. Tan, and X. Zhang: *Photoluminescence properties and exciton dynamics in monolayer WSe2*. Applied Physics Letters **105**, no. 10 (2014), 101901.

[58] F. Wang, J. Wang, S. Guo, J. Zhang, Z. Hu, and J. Chu: *Tuning Coupling Behavior of Stacked Heterostructures Based on MoS2, WS2, and WSe2*. Scientific Reports **7** (2017), 44712.

[59] Á. Szabó, S.J. Koester, and M. Luisier. *Ab-initio simulation of van der waals MoTe 2–SnS 2 heterotunneling fets for low-power electronics*. IEEE Electron Device Letters **36**, no. 5 (2015), 514-516.

Chapter 5. Conclusions

The synthesis of recently discovered atomically thin layered materials are crucially important factor to the performance of its electronic device applications. There are numerous details about synthesis techniques of these materials. Therefore, growth details need to be optimized to proceed further in new generation electronics applications by utilizing layered materials for daily life use.

As of first and the most important member of the atomically thin layered materials, graphene synthesis has not been fully optimized yet. The results reveal significant difference on different laboratories, which implies the necessity for more effective optimization on graphene growth. We investigated the intermittent effect of oxygen exposure on CVD growth of graphene to contribute to the ongoing efforts to improve graphene production for electronics based applications. We found that oxygen has a critical role on graphene growth by passivation Cu surface active sites and its etching effect on graphene product. We evaluated the effect of oxygen that introduced to the reaction chamber during the growth process with the existence of hydrogen and methane. It has been observed that the flow oxygen of 5 sccm during the growth optimizes the growth conditions by yielding uniform, monolayer graphene.

Surface cleanness is an important parameter for sensitive device applications. We investigated graphene surface contamination through various characterization techniques. We found that the surface contamination of graphene is not detectable by micro-scale characterization tools, on the other hand nano-scale electron microscopy techniques reveal

contamination. The one of the outcome of surface contamination of graphene is that prevents interlayer coupling of graphene with h-BN in its heterostructures. The source of contamination is mostly oxygen, and silicon, attributed to the factors from the CVD furnace.

The second order resonant Raman spectroscopy was performed to found a base to identify the structural information and phonon behaviors of WSe_2, $MoTe_2$, and $SnSe_2/WSe_2$, $SnS_2/MoTe_2$ heterostructures. We observed that the induced strain affects the Raman E^1_{2g} mode of WSe_2 by leading a peak splitting that can result to assignment of Raman modes, which are not well established yet.

As a general frame of this dissertation, a wide optimization process have been made to improve synthesis and characterization of atomically thin materials for applications related to the new generation electronics.